INVESTIGATIONS OF THE BALLISTIC RESPONSE OF BRITTLE MATERIALS

Charles E. Anderson, Jr.
James D. Walker
Jim Lankford

TECHNICAL REPORT
SwRI Project 06-5117/002

Prepared for

U.S. Army Research Office
P.O. Box 12211
Research Triangle Park, NC 27709-2211

November 1995

19960209 025

SOUTHWEST RESEARCH INSTITUTE
SAN ANTONIO
DETROIT
HOUSTON
WASHINGTON, DC

DISTRIBUTION STATEMENT A
Approved for public release;
Distribution Unlimited

DISCLAIMER NOTICE

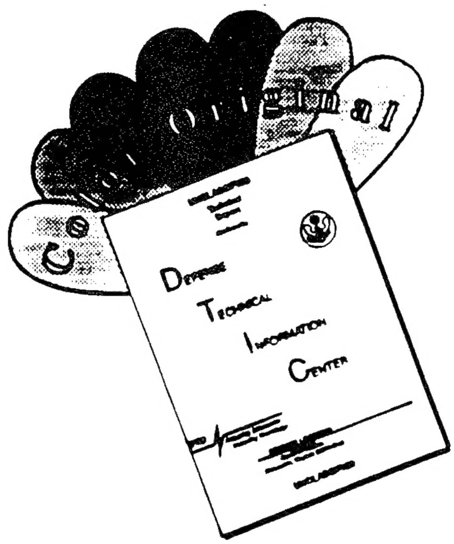

THIS DOCUMENT IS BEST QUALITY AVAILABLE. THE COPY FURNISHED TO DTIC CONTAINED A SIGNIFICANT NUMBER OF COLOR PAGES WHICH DO NOT REPRODUCE LEGIBLY ON BLACK AND WHITE MICROFICHE.

INVESTIGATIONS OF THE BALLISTIC RESPONSE OF BRITTLE MATERIALS

Charles E. Anderson, Jr.
James D. Walker
Jim Lankford

TECHNICAL REPORT
SwRI Project 06-5117/002

Southwest Research Institute
Materials and Structures Division
San Antonio, TX 78228-0510

Prepared for

U.S. Army Research Office
P.O. Box 12211
Research Triangle Park, NC 27709-2211

November 1995

Approved:

Geoffrey Dearnaley

Geoffrey Dearnaley, Vice President
Materials and Structures Division

THE VIEWS, OPINIONS, AND/OR FINDINGS CONTAINED IN THIS REPORT ARE THOSE OF THE AUTHOR(S) AND SHOULD NOT BE CONSTRUED AS AN OFFICIAL DEPARTMENT OF THE ARMY POSITION, POLICY, OR DECISION, UNLESS SO DESIGNATED BY OTHER DOCUMENTATION.

REPORT DOCUMENTATION PAGE

Form Approved
OMB No. 0704-0188

Public reporting burden for this collection of information is estimated to average 1 hour per response, including the time for reviewing instructions, searching existing data sources, gathering and maintaining the data needed, and completing and reviewing the collection of information. Send comments regarding this burden estimate or any other aspect of this collection of information, including suggestions for reducing this burden, to Washington Headquarters Services, Directorate for Information Operations and Reports, 1215 Jefferson Davis Highway, Suite 1204, Arlington, VA 22202-4302, and to the Office of Management and Budget, Paperwork Reduction Project (0704-0188), Washington, DC 20503.

1. AGENCY USE ONLY *(Leave blank)*	2. REPORT DATE	3. REPORT TYPE AND DATES COVERED
	November 1995	Final

4. TITLE AND SUBTITLE
Investigations of the Ballistic Response of Brittle Materials

5. FUNDING NUMBERS
DAAL03-92-K-0001

6. AUTHOR(S)
Charles E. Anderson, Jr.
James D. Walker
Jim Lankford

7. PERFORMING ORGANIZATION NAME(S) AND ADDRESS(ES)
Southwest Research Institute
Materials and Structures Division
6220 Culebra Road
P.O. Drawer 28510
San Antonio, TX 78228-0510

8. PERFORMING ORGANIZATION REPORT NUMBER
SwRI 5117/002

9. SPONSORING / MONITORING AGENCY NAME(S) AND ADDRESS(ES)
U.S. Army Research Office
P.O. Box 12211
Research Triangle Park, NC 27709-2211

10. SPONSORING / MONITORING AGENCY REPORT NUMBER
ARO 29788.13-MS

11. SUPPLEMENTARY NOTES
The views, opinions and/or findings contained in this report are those of the author(s) and should not be construed as an official Department of the Army position, policy, or decision, unless so designated by other documentation.

12a. DISTRIBUTION / AVAILABILITY STATEMENT
Approved for public release; distribution unlimited.

12b. DISTRIBUTION CODE

13. ABSTRACT *(Maximum 200 words)*
A multi-faceted study of the ballistic response of brittle materials has been performed to include experimental testing, numerical simulations, constitutive evaluation, and investigation of fundamental material response to high rate loading. Depth-of-penetration tests with and without cover plates investigated the performance of 99.5% pure aluminum oxide tiles to ballistic impact using *L/D* 10 tungsten heavy alloy projectiles at two impact velocities, nominally 1.5 and 1.8 km/s. Numerical simulations, using the EPIC95 finite element hydrocode, were compared to the results of the experiments. The Johnson-Holmquist II constitutive model was used for the computations. Ballistic tests, conducted by the Ernst-Mach-Institut in Germany, recorded *in-situ* positions of the nose and tail of the projectile at different times after impact, using flash radiography, in soda lime glass. The experimental arrangement was modified so that the projectile velocity was obtained after exiting a finite-thick glass target. The experimental data are analyzed, and numerical simulations of the experiments were conducted using the Eulerian wavecode CTH. Comparisons between the calculations and the experiments using different computational constitutive models provided insight into the constitutive behavior of the glass. Lastly, an experimental apparatus was designed to investigate the behavior of 99.5% pure alumina under large confinement within a controlled laboratory experiment. A split-Hopkinson pressure bar was used to load the confined specimen at a high rate. Metallurgical examination of the specimen after the test demonstrates large plastic flow within the specimen, with cracks originating at locations where dislocations pile up.

14. SUBJECT TERMS
ballistic limit, brittle materials, glass, ceramics, autofrettage, penetration mechanics, CTH, EPIC, tile efficiency, confinement, numerical simulations, constitutive modeling

15. NUMBER OF PAGES
112

16. PRICE CODE

17. SECURITY CLASSIFICIATION OF REPORT	18. SECURITY CLASSIFICATION OF THIS PAGE	19. SECURITY CLASSIFICATION OF ABSTRACT	20. LIMITATION OF ABSTRACT
UNCLASSIFIED	UNCLASSIFIED	UNCLASSIFIED	UL

NSN 7540-01-280-5500

Standard Form 298 (Rev. 2-89)
Prescribed by ANSI Std. 239-18 298-102
IAT Form 13a 3/93

TABLE OF CONTENTS

LIST OF FIGURES

LIST OF FIGURES (CONT'D)

LIST OF FIGURES (CONT'D)

LIST OF FIGURES (CONT'D)

LIST OF TABLES

NOTATION

A, B, C, m, n, SFMAX, D_1, D_2: material constants in the JH-2 constitutive model (see Fig. 18)

A^T thermal expansion term

c_l longitudinal sound speed

c_o bulk sound speed

c_s shear sound speed

c_v specific heat

Δe_c differential tile efficiency

E_m mass efficiency

D damage parameter ($0 \leq D \leq 1$)

D projectile diameter

G shear modulus

H indentation hardness

HEL Hugoniot elastic limit

J_2 second stress invariant

J_3 third stress invariant

k slope of shock-particle velocity curve

K bulk modulus

L, L_o initial projectile length

L_R instantaneous (residual) projectile length

L_R' residual projectile length after exiting modified target

L_R^* residual projectile length recovered in the impact tank

P pressure (mean stress)

ΔP incremental pressure increase from bulking

P_{HEL} pressure at the Hugoniot Elastic Limit

P_∞ depth of penetration in a semi-infinite steel target

P_r (residual) depth of penetration into steel substrate

P_T total penetration ($T_{cp} + T_c + P_r$)

P^* normalized pressure in JH-2 constitutive model ($P^* = P/P_{\mathrm{HEL}}$)

R_t target resistance

S_H	distance projectile tail has moved
S_K	penetration depth
S_K'	penetration depth (thickness) of modified target
t	time
T	maximum tensile hydrostatic pressure a material can withstand
T	temperature
T_c	ceramic thickness
T_c'	estimate of the depth of penetration into a semi-infinite ceramic tile
T_{cp}	cover plate thickness
T_m	melt temperature
T^*	normalized maximum tensile hydrostatic pressure in JH-2 constitutive model ($T^* = T/P_{HEL}$)
$\bar{T}$	homogenized temperature
u	penetration velocity
u_r	radial displacement
u_z	axial displacement
V	impact velocity
V_p	impact velocity
V_R'	residual velocity after exiting modified target
Y_D	dynamic yield strength
Y_S	static yield strength
Y_p	projectile flow stress
$\bar{Y}$	cap on flow stress
$\alpha(T)$	coefficient of thermal expansion
β	fraction of elastic energy converted to hydrostatic potential energy
β	coefficient for pressure-dependent flow stress
ε_p	equivalent plastic strain
$\Delta\varepsilon_p$	increment in equivalent plastic strain calculated during a cycle of integration
$\dot{\varepsilon}$	plastic strain rate normalized by a reference strain rate of 1.0 s^{-1}
ε_p^f	equivalent plastic strain to fracture in JH-2 constitutive model
ε_{rr}	radial strain
$\varepsilon_{\theta\theta}$	hoop strain

ε_{zz} axial strain

ε_{zr} shear strain

Γ Grüneisen coefficient

λ Lamé constant

μ reduced density ($\mu = \rho/\rho_o - 1$)

μ Lamé constant (shear modulus, $\mu \equiv G$)

ρ_p projectile density

ρ_{st} steel density

ρ_t target density

σ^* normalized equivalent stress ($\sigma^* = \sigma_{eq}/\sigma_{\mathrm{HEL}}$)

σ_c compressive strength

σ_{eq} equivalent flow stress

σ_{HEL} stress at Hugoniot Elastic Limit

σ_i^* normalized intact strength in JH-2 constitutive model (see Fig. 18)

σ_f^* normalized fractured strength in JH-2 constitutive model (see Fig. 18)

1.0 INTRODUCTION

A variety of topics were investigated during the performance of this contract, all with a focus to provide a more fundamental understanding of the interaction of projectiles with armor targets. Extensive use of numerical simulations assisted in an analysis of projectile-target interactions. The following list provides a reasonably complete summary of the work:

1. pretest predictions of near full-scale experiments into armor technology targets (a finite-thick RHA target, a ceramic laminate target, and a spaced-plate target);

2. investigation of the penetration mechanics of $L/D \leq 1$ projectiles;

3. investigation of the penetration performance of short $1 \leq L/D \leq 6$ projectiles;

4. investigation of the penetration mechanics of the *L/D* effect;

5. a study of the erosion mechanisms of tungsten alloy penetrators;

6. a critical evaluation of the ability of state-of-the-art hydrocodes to reproduce the experimentally-measured time history of long-rod projectiles penetrating high-hard steel targets near the ballistic limit velocity (for two target thicknesses, i.e., two impact velocities);

7. experimental investigation of the ballistic performance of confined 99.5% Al_2O_3 ceramic tiles (with and without cover plates);

8. computational investigations of the penetration of ceramics;

9. a critical evaluation of the ability of state-of-the-art hydrocodes to reproduce the experimentally-measured time history of long-rod projectiles penetrating glass targets at two impact velocities;

10. the development of a unique device to obtain dynamic material property behavior of confined ceramic (intact and *in-situ* communited).

The research and findings for most of the items above have been documented in conference or symposia proceedings, journal articles, or reports [1-18]. This report provides the documentation for item 7, one portion of the work in item 8, and items 9 and 10.

2.0 CERAMIC EXPERIMENTS

2.1 Background

The depth-of-penetration (DOP) test has been used to investigate the ballistic performance of ceramic tiles since approximately 1986 [19]. In this arrangement, the ceramic tile is placed on, or in a cavity of, a metallic (aluminum or steel) substrate; the evolution of the DOP test is discussed in Ref. [20]. It is well-known that the performance of ceramic tiles increases with confinement [21-22]. In this context, there are two issues relative to confinement: lateral (or radial) confinement, and confinement by a cover plate. Partom and Littlefield [23] have modified cavity expansion theory to examine lateral confinement. Lateral confinement can be achieved by having sufficiently large (wide) tiles, or by placing the ceramic tile within a metal cavity. Reference [20] describes an empirically-based formula for estimating the amount of radial confinement necessary to achieve "saturated" ballistic performance. Less well studied and documented is the efficacy of cover plates. In general, it has been noted that a cover plate improves the ballistic performance of the tile, but if lateral confinement is not adequate, performance is degraded by the cover plate [24].

Numerical simulations of the response of ceramic tiles to flyer plate impacts has met with some success as described in Refs. [25-28] and in this report. However, the ability to predict the performance of a ceramic target to ballistic impact is considerably more uncertain, e.g., Ref. [7, 26-27]. Therefore, the present investigation had a two-fold purpose. First, there is a desire to investigate the ballistic performance of ceramic tiles as a function of the degree of confinement offered by cover plates. Nominally, three different experimental conditions were investigated: no cover plate, confinement by a mild steel cover plate, and confinement by a high-hard steel cover plate. It was hypothesized that if cover plate confinement was important, the ballistic performance of the ceramic should increase as the strength of the cover plate increased.

Second, the experiments were designed to provide a suite of tests for numerical simulations. Generally, ballistic impact experiments have been required to determine some of the constants in ceramic constitutive models, in particular, the flow stress of the comminuted material. Therefore, to ensure that agreement is not a result of "tuning" of the constitutive constants to one impact velocity, the experiments were designed to obtain data at two impact velocities. Thus, the

experimental data would serve as benchmark data for numerical simulations since issues of confinement and impact velocity are addressed in the test matrix.

2.2 Experimental Procedure

Projectiles. The experiments were conducted using tungsten-alloy long-rod projectiles with length-to-diameter ratios, including the hemispherical nose, of 10. All projectiles were made by Teledyne Firth Sterling from their X27X alloy (91.23% W, 5.98% Ni, and 2.79% Co), which has a density of 17.54 g/cm^3. The projectile radius was 0.381 cm, and the length 7.62 cm. The projectiles were cold worked (swaged) 25%, and aged at 400°C for one hour, giving the alloy an ultimate tensile strength of 1.5 GPa at 9% elongation with little or no work hardening. Threads (3/8-16 UNC-3A) were placed exterior to the main portion of the cylindrical rod over the center 3.81 cm to provide a gripping surface for the sabot, Fig. 1a. The total mass of the projectile was approximately 66.7 g (60 g for the cylindrical portion of the rod, and 6.7 g for the threads). A four-piece puller aluminum sabot, Fig. 1b, was used to launch the projectiles from the SwRI 30-mm powder gun.

Targets. The aluminum oxide tiles were 2.586±0.003-cm thick and 10.16 cm in diameter. The ceramic tiles were 99.5% pure Al_2O_3 (CAP3 from Coors), with a density of 3.90 g/cm^3. A variety of target configurations, Fig. 2, were used to vary the degree of confinement:

- unconfined (bare) ceramic tile (UCC);
- radially-confined (by a steel surround) ceramic tile (RCC);
- ceramic confined by a steel surround and with a 0.635-cm thick mild steel cover plate (1 MSCP);
- ceramic confined by a steel surround and with a 0.635-cm thick high-hard steel cover plate (1 HHCP);
- ceramic confined by a steel surround and with two 0.635-cm thick mild steel cover plates (2 MSCP); and
- ceramic confined by a steel surround and with two 0.635-cm thick high-hard steel cover plates (2 HHCP).

The steel surround was a 15.2-cm diameter cylinder of 4340 steel heat treated to a Rockwell C hardness of R_C 31±2. The length of the surround was sufficient to totally contain penetration. A

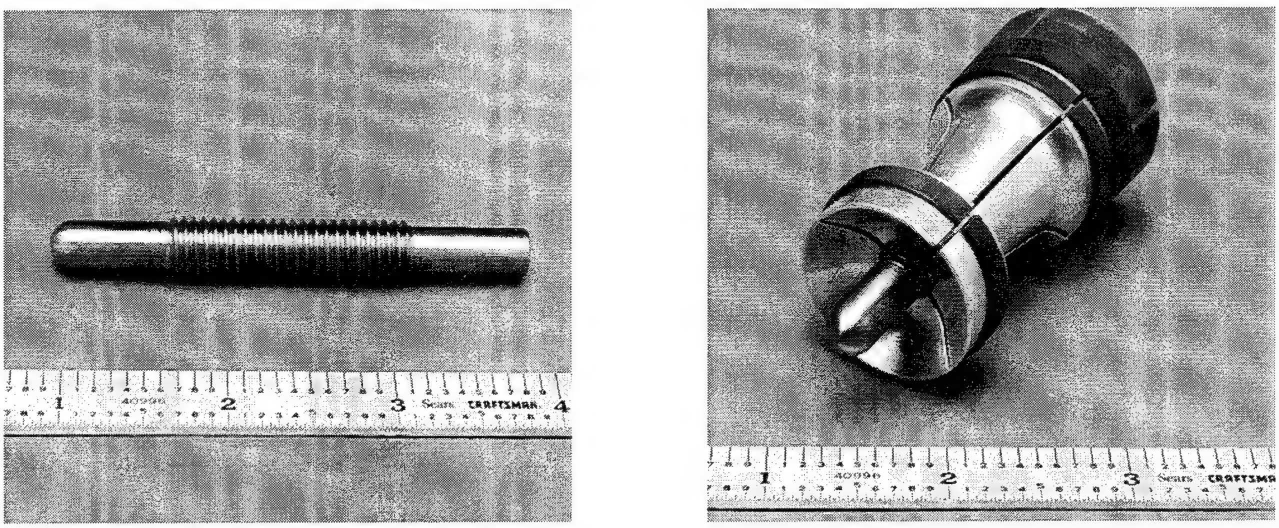

Figure 1. Projectile and Sabot

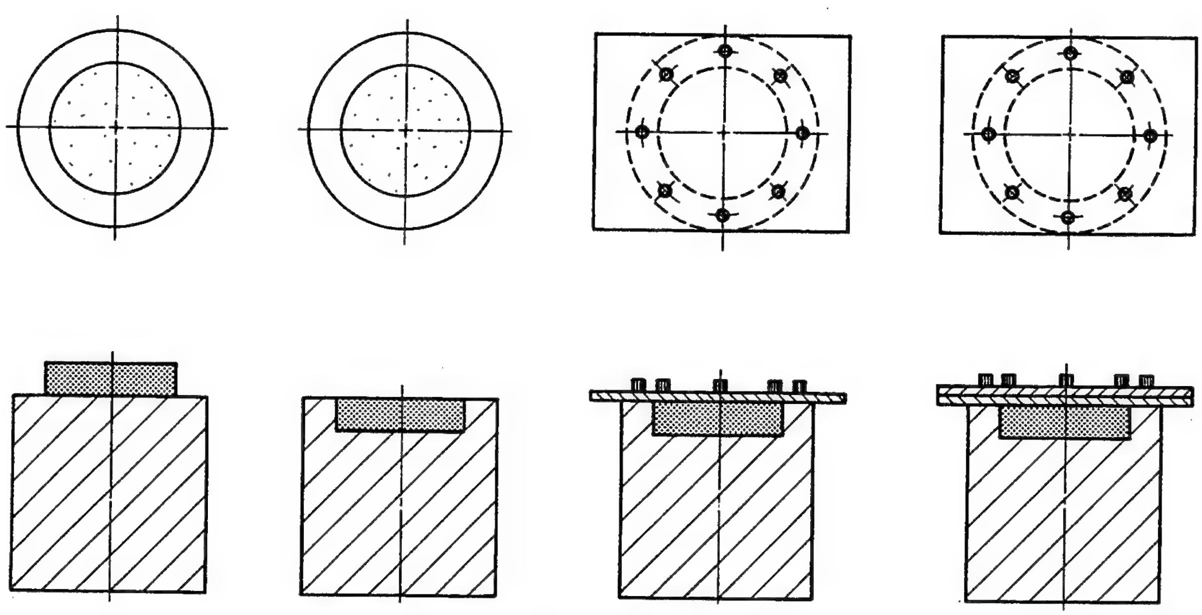

a) unconfined (bare) tile

b) radially-confined tile

c) single cover plate

d) double cover plate

Figure 2. Schematic of target configurations

2.54-cm deep recess was machined in the steel for the ceramic tiles. Prior to gluing, the target recess was cleaned with acetone to remove any remaining cutting oil. The ceramic was glued in place with epoxy (Easypoxy K20 by Conap). A thin coat of epoxy was evenly applied onto the bottom surface of the ceramic and a thin bead (approximately 5-mm diameter) placed at the base of the tile wall. The ceramic tile was then pressed into the recess. The tile was turned in the recess to spread the adhesive evenly on the walls. The excess epoxy was removed from the surface with acetone and the epoxy was allowed to cure for 24 hours at 70°F. The unconfined ceramic tile was glued directly to the steel surface.

Cover Plates. Socket head grade 8 (R_C 35) bolts, 3/8-in diameter, equally spaced around the circumference, were used to attach the cover plates to the steel surround. The recess for the ceramic was slightly less than the thickness for the ceramic, thereby ensuring that the cover plate was in direct contact with the ceramic tile. The bolts were torqued to a tightness of 81.3 N-m. The mild steel plates had a Rockwell B hardness of R_B 48.5, and the high-hard steel plates had a hardness of R_C 48.5, per MIL-A-461000.

2.3 Experimental Results

Baseline RHA Penetration Data. Prior to testing the ceramic targets, the baseline performance of the projectile into the steel target was quantified. The depths of penetration into the targets were measured and are plotted as normalized penetration *P/L* as a function of impact velocity in Fig. 3. A linear least squares fit through the data, represented by the solid line in Fig. 3, gives the following correlation:

$$\frac{P_\infty}{L} = 1.030V - 0.695. \tag{1}$$

Woolsey, *et al.* [29-30], have obtained data for *L/D* 10 projectiles made from the X27C and X21C alloy, using targets with an average hardness of R_C 27±2. The regression line through the Woolsey, *et al.,* data is denoted by the dashed line. The targets used for this study were R_C 31±2; adjusting Woolsey's data to the same steel hardness used in this study gives the dotted line in Fig. 3, which

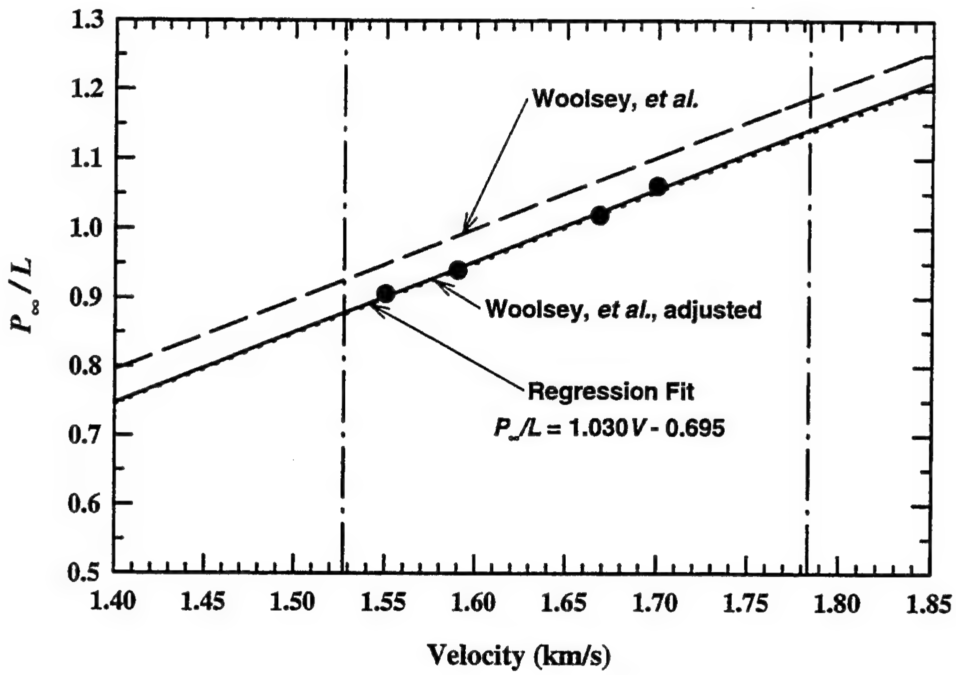

Figure 3. Baseline penetration

is in very good agreement with the current data. Therefore, Eqn. (1) will be used to provide the reference penetration performance as a function of impact velocity.

Ceramic Testing. Two impact velocities were used in the testing, nominally 1.53 km/s and 1.78 km/s, denoted by the vertical dot-dash lines in Fig. 3. The residual depth of penetration P_r into the backup steel cylinder was the experimental measure of penetration performance. The target code, the test number, tile thickness, cover plate thickness, impact velocity, residual penetration into the steel substrate, and total penetration (cover plate plus ceramic tile plus substrate) are listed in Table 1. The target code is as follows: the first two numbers give the approximate impact velocity, the third number is the number of cover plates. The two alphabetical characters provide further information about confinement: UC stands for the unconfined ceramic, RC stands for the (no cover plate) radially-confined ceramic, MS represents the use of a mild steel cover plate, and HH denotes the high-hard steel cover plate.

Photographs of the post-test targets are illustrative of the large forces exerted on the cover plates. First, Fig. 4 shows the ceramic remnants from an experiment. Much of the ceramic is highly comminuted, in the form of a fine, powder-like residue that is spread all over the test pad. The fragments seen in Fig. 4 are from the "edges" of the original ceramic tile.

Table 1. Experimental Conditions and Results for Ceramic Tests

Target Code	Test No.	T_c (cm)	T_{cp} (cm)	V (km/s)	P_r (cm)	P_T (cm)
150RC	6	2.586	0.000	1.55	4.32	6.90
150RC	7	2.583	0	1.52	4.32	6.90
170RC	14	2.591	0	1.78	6.06	8.65
170RC	15	2.586	0	1.79	6.20	8.78
151MS	8	2.586	0.635	1.56	3.4	6.62
151MS	9	2.581	0.635	1.53	3.37	6.58
171MS	20	2.588	0.635	1.70	4.38	7.60
171MS	21	2.581	0.635	1.78	4.78	7.99
151HH	10	2.583	0.635	1.52	3.25	6.47
151HH	11	2.586	0.635	1.51	3.05	6.27
151HH	32	2.583	0.635	1.55	2.86	6.08
151HH	33	2.581	0.635	1.51	2.84	6.06
171HH	22	2.581	0.635	1.78	3.51	6.72
171HH	23	2.586	0.635	1.80	4.62	7.84
150UC	18	2.586	0	1.50	4.65	7.23
150UC	19	2.583	0	1.48	4.36	6.94
170UC	16	2.588	0	1.78	6.18	8.77
170UC	17	2.588	0	1.79	6.30	8.89
152MS	29	2.588	1.27	1.47	2.72	6.58
172MS	24	2.588	1.27	1.78	4.45	8.3
172MS	25	2.588	1.27	1.79	4.52	8.38
152HH	30	2.586	1.27	1.52	2.67	6.52
152HH	31	2.591	1.27	1.48	1.97	5.83
172HH	26	2.586	1.27	1.80	4.50	8.35
172HH	27	2.586	1.27	1.75	4.14	8.00

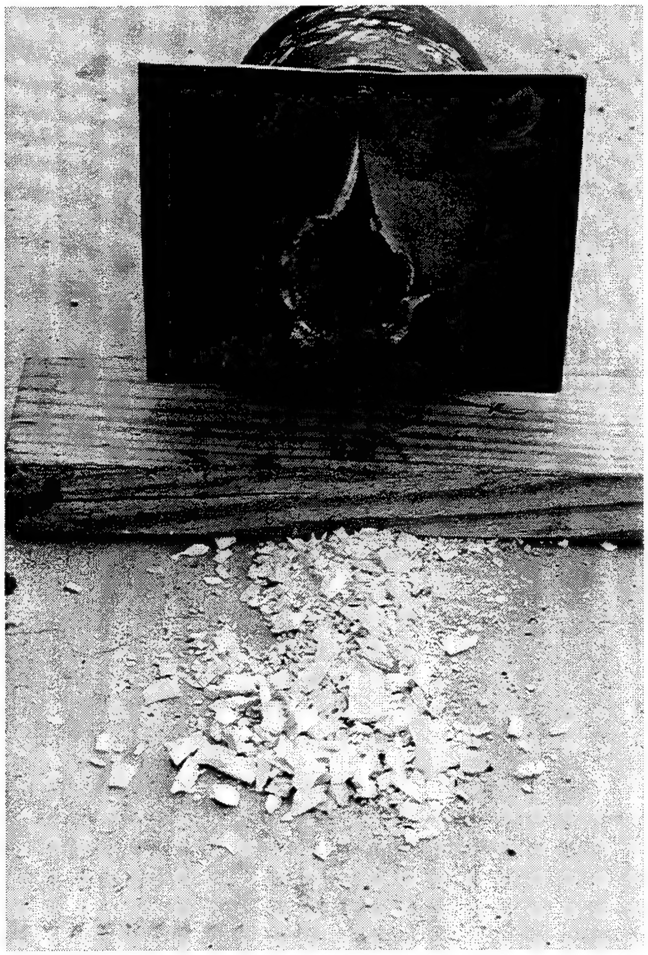

Figure 4. Photograph of the fragmented remnants of the ceramic tile

The sequence of photographs in Figs. 5-13 each show a side view of the target and cover plate, and a top view of the cover plate. Several observations are readily apparent. Originally, eight bolts were used to secure a single 0.635-cm thick cover plate ($T_{cp}/D = 0.833$). The mild steel cover plate underwent such severe deformation, presumably as a result of the bulking of the highly comminuted ceramic, that the plate was "torn" after a test; and at 1.78-km/s, the deformation was even more severe, Figs. 5 and 6. The high-hard cover plate resisted the deformation observed for the mild steel cover plate; instead, the bolts failed in tension and/or shear and the cover plate was not attached to the main target after the test, Fig. 7. The number of bolts was doubled to 16 to spread the load among more bolts. Although the bolts again failed, the plate was more severely deformed for the 16-bolt configuration, indicating that the plate must have remained in place longer before bolt

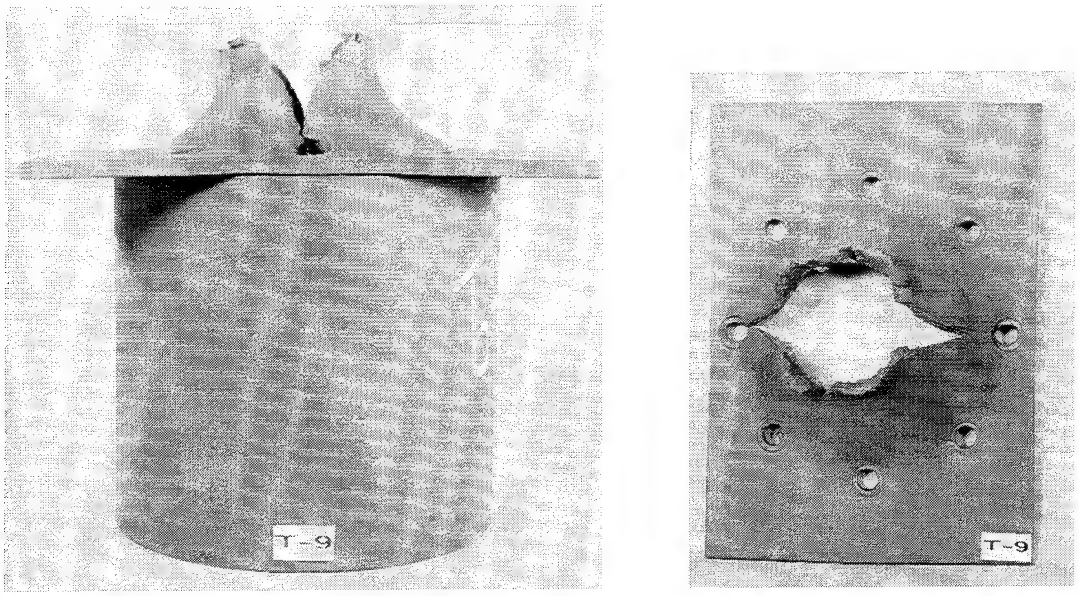

Figure 5. Test 9, one mild steel cover plate, $V = 1.53$ km/s

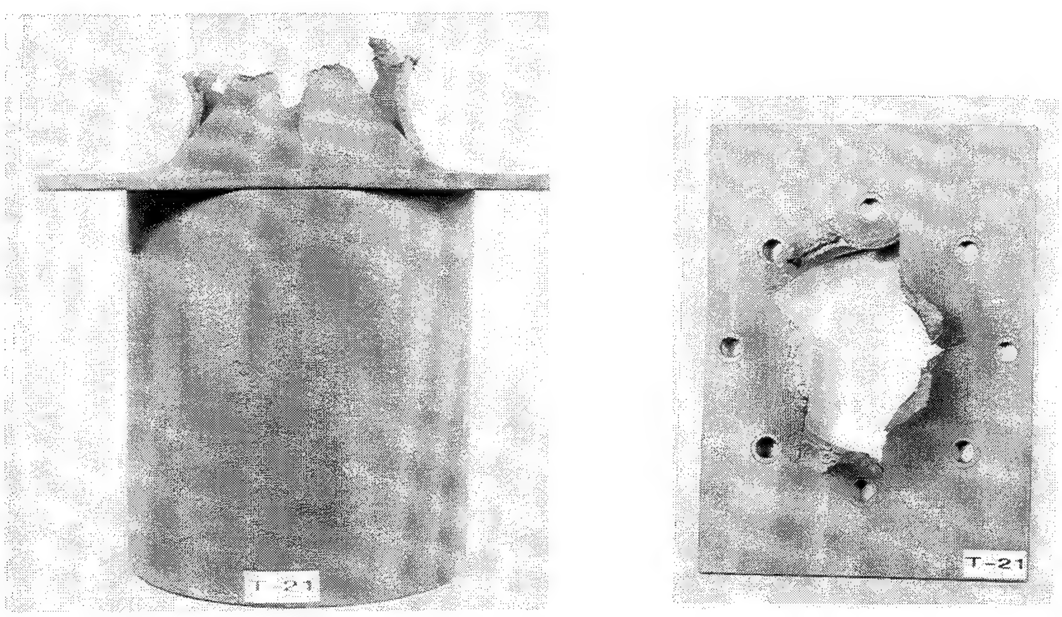

Figure 6. Test 21, one mild steel cover plate, $V = 1.78$ km/s

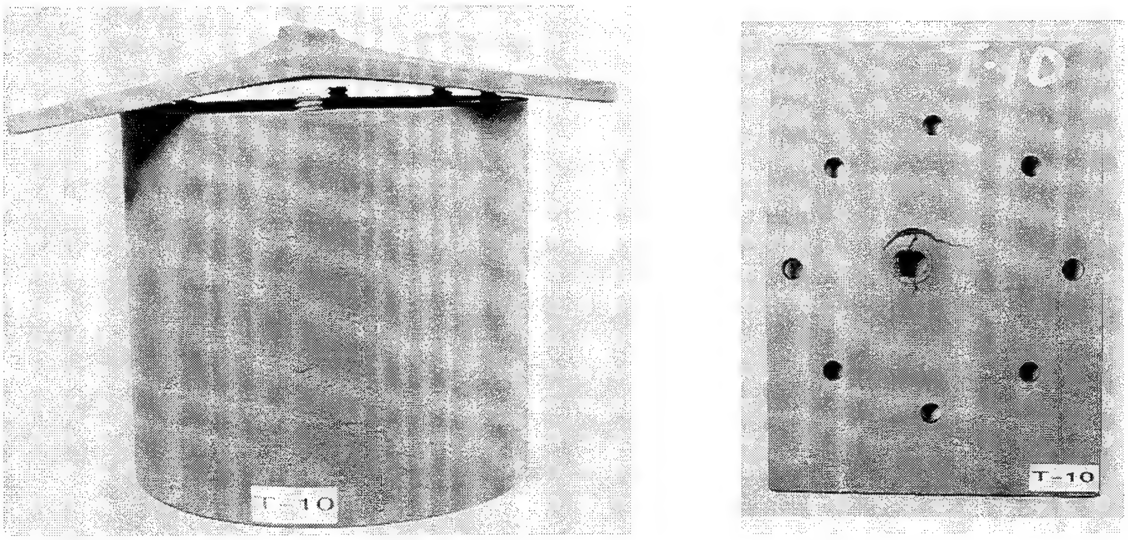

Figure 7. Test 10, one high-hard steel cover plate, V = 1.52 km/s

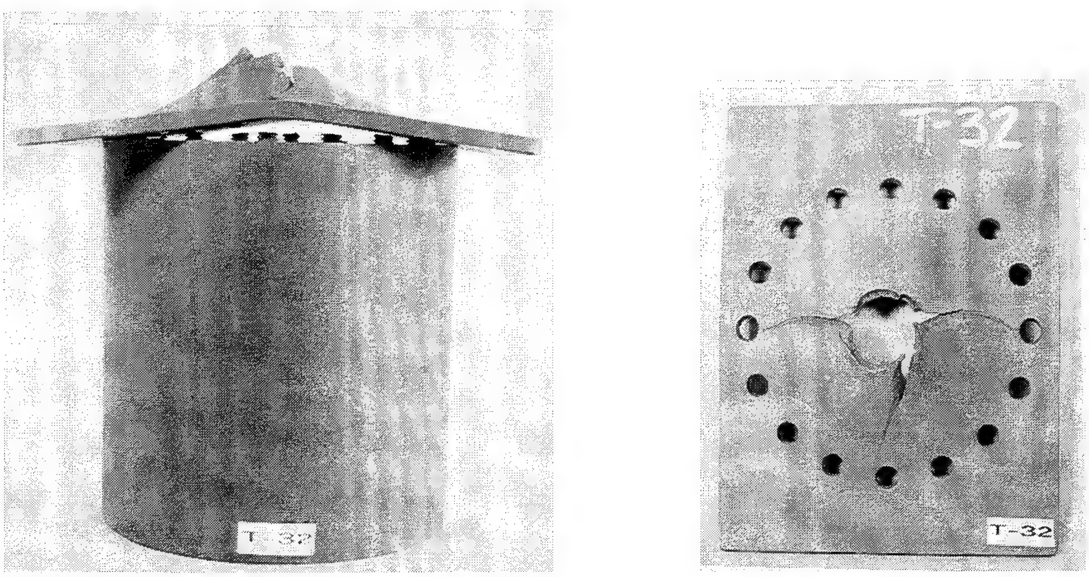

Figure 8. Test 32, one high-hard steel cover plate, V = 1.55 km/s

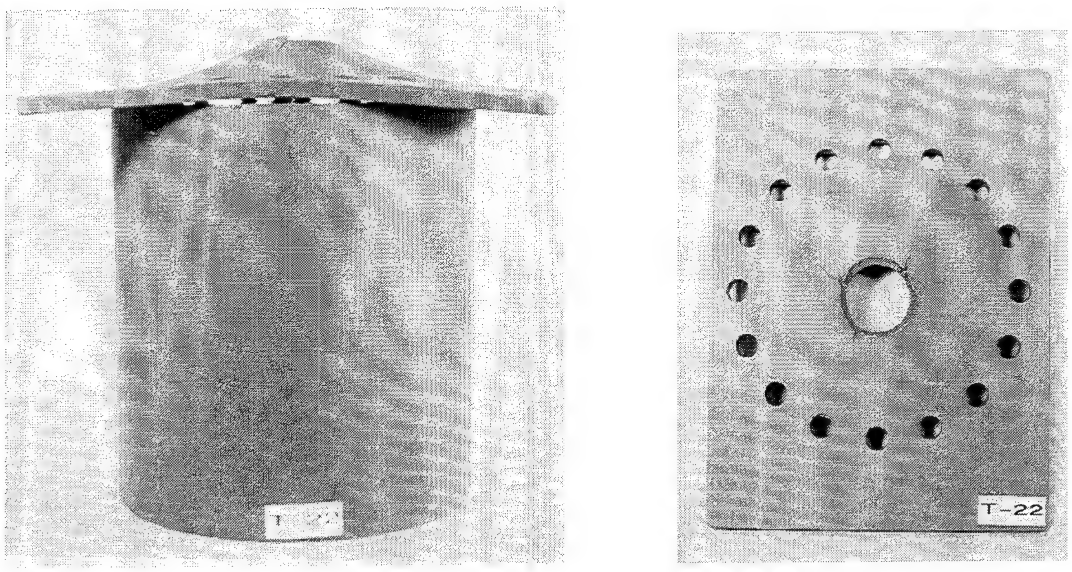

Figure 9. Test 22, one high-hard steel cover plate, V = 1.78 km/s

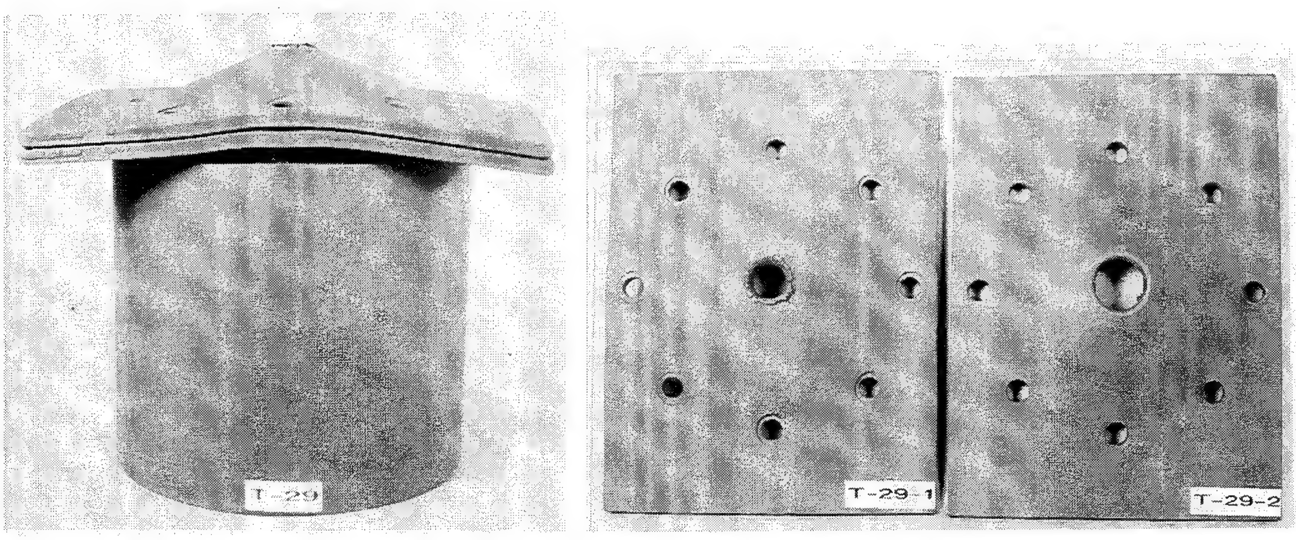

Figure 10. Test 29, two mild steel cover plates, V = 1.47 km/s

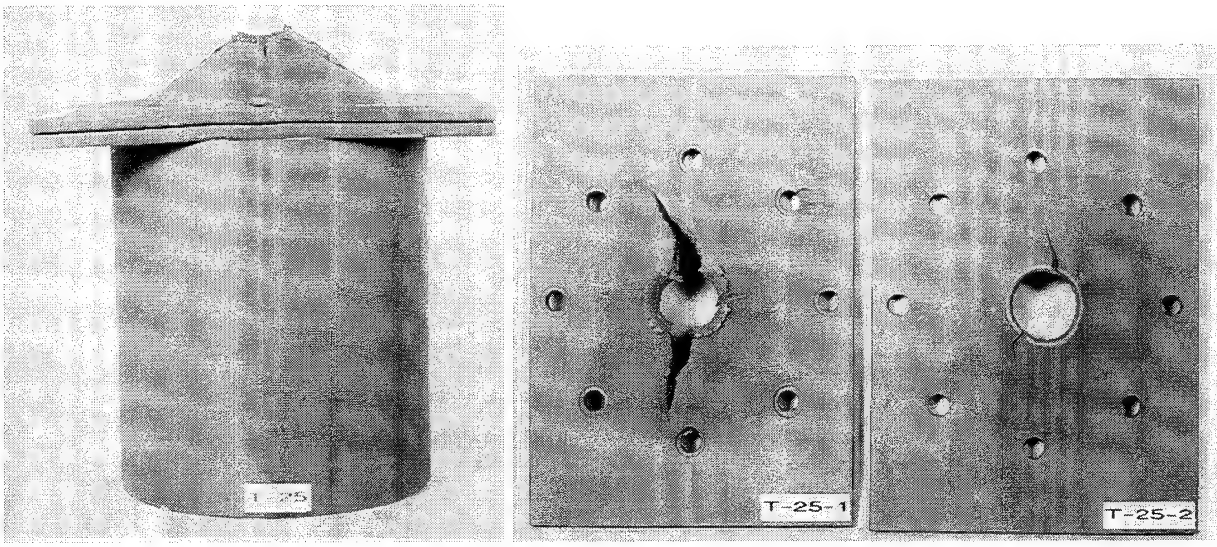

Figure 11. Test 25, two mild steel cover plates, $V = 1.79$ km/s

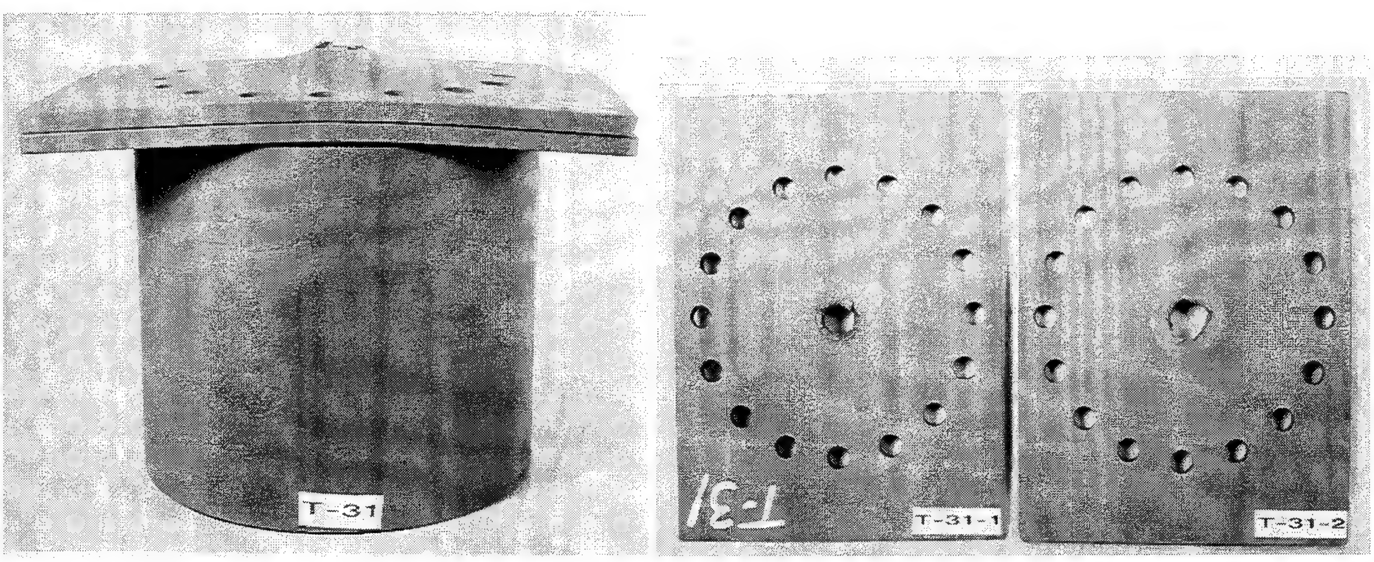

Figure 12. Test 31, two high-hard steel cover plates, $V = 1.48$ km/s

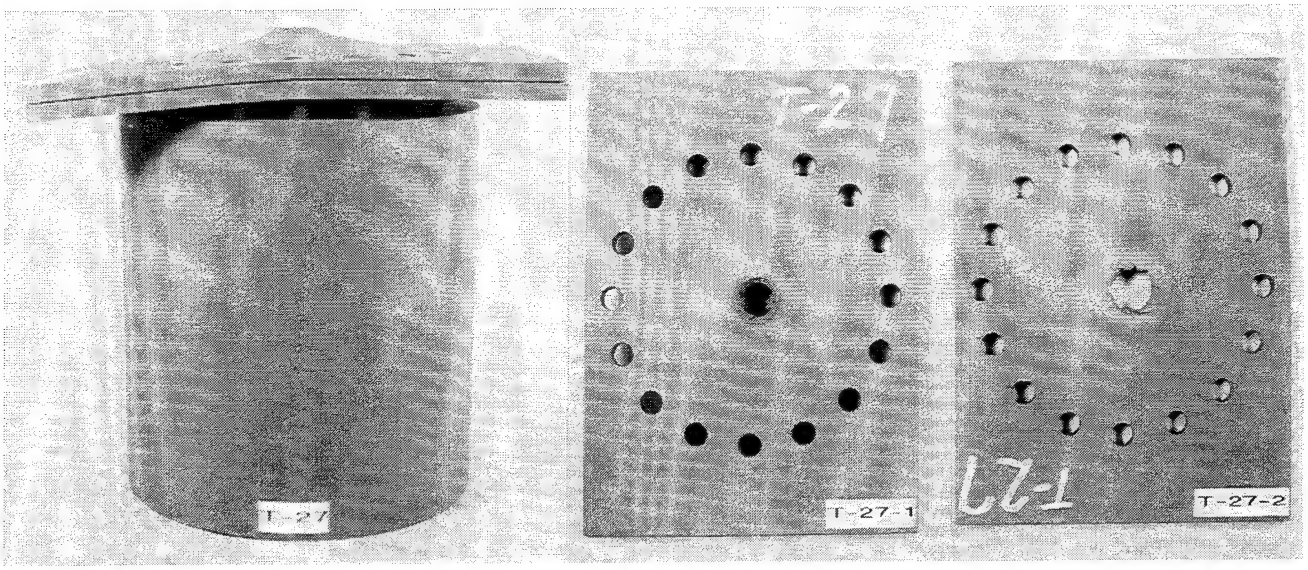

Figure 13. Test 27, two high-hard steel cover plates, V = 1.75 km/s

failure, Fig. 8. At the higher impact velocity, the bolts must have failed sooner since there is not as much deformation in the cover plate, Fig. 9.

Next, it was decided to use two 0.635-cm thick plates, for a total thickness of 1.27 cm (T_{cp}/D = 1.67), to increase the overall stiffness of the cover plates, Figs. 10-13. Although the plates bulged outward for the two mild steel cover plates at the 1.5-km/s impact velocity, the double-thick plates remained intact after the test, that is, there was no "tearing" of the plates, Fig. 10. At the higher impact velocity, deformation was sufficient to cause the plates to again tear, as shown in Fig. 11, but nowhere to the extent of the single-plate test, Fig. 6. The double-thick high-hard steel cover plate arrangement had sufficient stiffness that only a few of the bolts failed at the lower impact velocity, and the plates remained attached in one of the tests, Fig. 12. At the higher impact velocity, the bolts again failed, but there was considerably less overall deformation of the cover plates as compared to the single high-hard steel cover plate, Fig. 13 versus Fig. 9.

The total penetration normalized by the projectile length P_T/L is plotted versus impact velocity in Fig. 14. Solid lines connect similar target geometries. For comparison purposes, Eqn. (1) for semi-infinite steel is also plotted in the figure.

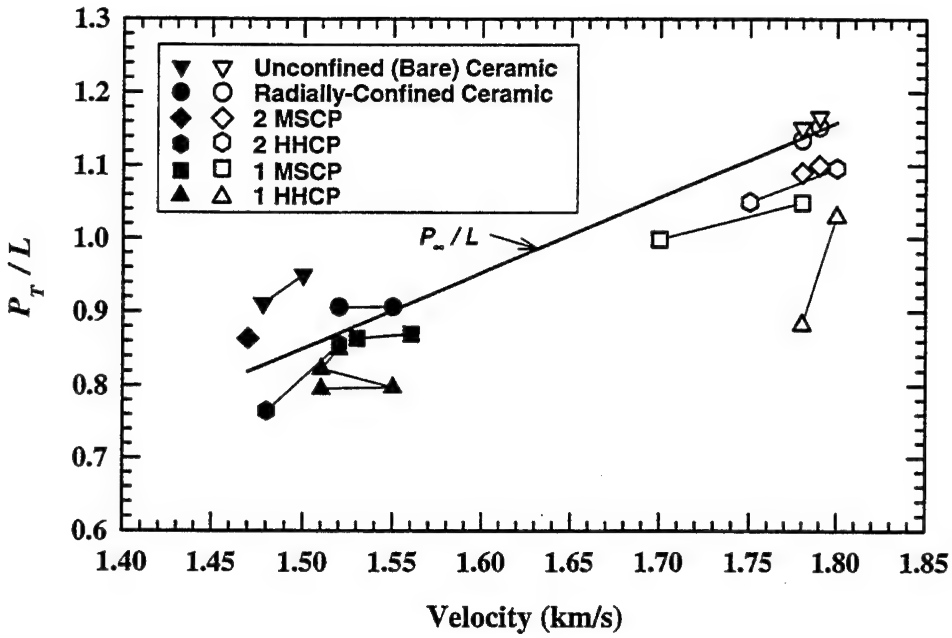

Figure 14. Total normalized penetration versus impact velocity

2.4 Analysis

It is informative to compute some measures of performance for the ceramic such as the mass efficiency , the differential tile efficiency, or the target resistance. The mass efficiency E_m compares the ballistic performance of the target to that of the baseline steel target, and is defined as:

$$E_m = \frac{P_\infty \rho_{st}}{T_{cp}\rho_{st} + T_c\rho_c + P_r\rho_{st}} . \tag{2}$$

The E_m's are tabulated in Table 2. Probably of more interest is the differential tile efficiency Δe_c since it specifically provides a quantitative measure of the performance of the ceramic tile as contrasted to the performance of the target-penetrator combination. Therefore, the differential efficiency more readily permits comparison of the data here with that of other researchers. It is defined as:

Table 2. Calculated Values of Ceramic Performance

Target Code	Test No.	E_m (cm)	Δe_c (cm)	$R_t(1)$ (km/s)	$R_t(2)$ (cm)
150RC	6	1.23	1.99	5.73	6.68
150RC	7	1.18	1.81	5.21	6.11
170RC	14	1.18	2.04	5.65	6.40
170RC	15	1.17	1.99	5.48	6.20
151MS	8	1.31	2.27	6.53	7.55
151MS	9	1.27	2.12	6.11	7.11
171MS	20	1.28	2.36	6.80	7.73
171MS	21	1.30	2.55	7.37	8.30
151HH	10	1.28	2.14	6.18	7.20
151HH	11	1.32	2.24	6.43	7.49
151HH	32	1.44	2.64	7.45	8.59
151HH	33	1.38	2.40	6.84	7.95
171HH	22	1.60	3.54	10.11	11.26
171HH	23	1.35	2.79	8.10	9.08
150UC	18	1.09	1.42	4.02	4.76
150UC	19	1.12	1.52	4.38	5.18
170UC	16	1.16	1.94	5.30	6.00
170UC	17	1.15	1.91	5.18	5.86
152MS	29	1.18	1.76	5.10	6.03
172MS	24	1.24	2.30	6.58	7.43
172MS	25	1.24	2.31	6.58	7.42
152HH	30	1.27	2.10	6.06	7.08
152HH	31	1.40	2.40	6.80	7.93
172HH	26	1.25	2.39	6.85	7.71
172HH	27	1.26	2.36	6.78	7.67

$$\Delta e_c = \frac{[P_\infty - (P_r + T_{cp})]\rho_{st}}{T_c \rho_c} . \tag{3}$$

The Δe_c's are plotted in Fig. 15, and listed in Table 2. The solid lines connect nominally identical tests.

Examining Fig. 15, there are several conclusions that can readily be made concerning the ballistic performance of ceramic tiles, albeit there are counterexamples to these observations:

- the ballistic performance of a ceramic tile increases with confinement (unconfined ceramic tile to radially-confined ceramic tile, to confinement with a cover plate);

- a steel cover plate improves the ballistic performance of a ceramic tile (for a radially-confined ceramic tile); and

- the ballistic performance of a ceramic tile is a function of the hardness and thickness of the cover plate (differences in penetration of the cover plates due to cover plate hardness are implicitly included in the calculation of Δe_c).

- there appears to be a strong increase in ceramic performance with impact velocity for V between 1.50 and 1.55 km/s but then performance increases considerably slower with velocity up to 1.80 km/s.

There are two, and perhaps three, points that are notable counterexamples to the last observation. The slight variation between Test Nos. 6 and 7 is almost certainly due to test-to-test variability and therefore should be considered as indicative of "data scatter," as opposed to a "violation" of the observed trends. However, Test Nos. 31 and 22 show significant increases in ceramic performance relative to other similar points in the test matrix, and are counter to the trends exhibited by the other data. In particular, Test No. 22 has a Δe_c of approximately 3.6, considerably larger than any of the other Δe_c's. More will be said about these latter observations in the paragraph below.

An alternative expression for tile performance is the Tate resistance R_t. There are two ways of calculating R_t from DOP data [31]. Both methods are based on the application of steady-state theory, and in particular, application of the Tate model [32]. However, the assumptions invoked, aside from the premise of steady state, are slightly different. The first method uses the residual

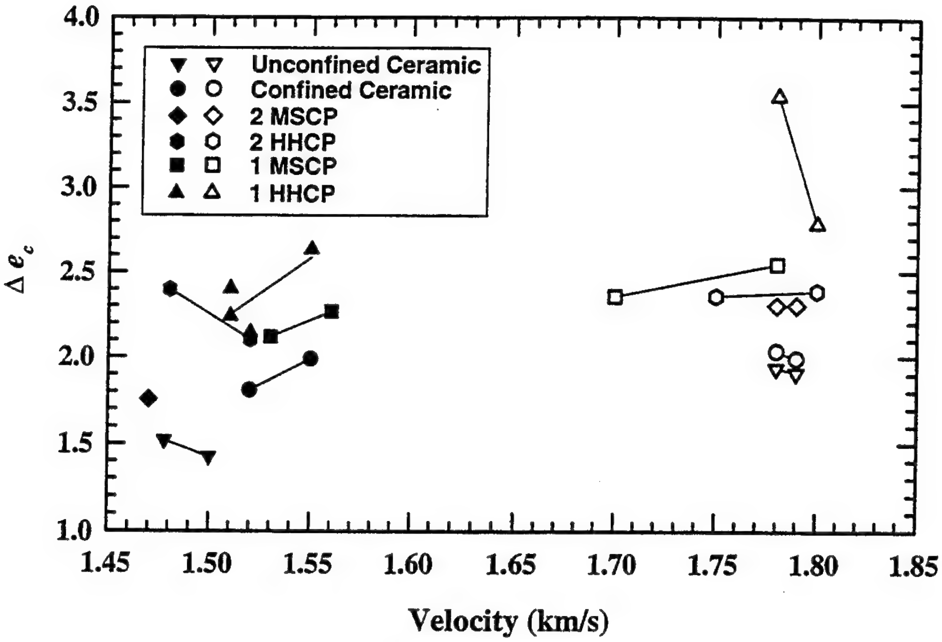

Figure 15. Differential tile performance

penetration and the tile thickness to estimate the tile thickness T_c' that would result in zero residual penetration:

$$T_c' = \frac{T_c P_\infty}{P_\infty - (P_r + T_{cp})} . \tag{4}$$

R_t in the Tate model is adjusted until the depth of penetration predicted by the model gives T_c'. The R_t's calculated with this method are given in Table 2 under the column $R_t(1)$. The second method for calculating the target resistance requires an estimate of the penetration velocity u in the ceramic tile. R_t is then calculated from the modified Bernoulli law:

$$R_t = Y_p + \frac{1}{2}\rho_p(V - u)^2 - \frac{1}{2}\rho_t u^2. \tag{5}$$

The penetration velocity is estimated by assuming penetration into the substrate is proportional to the residual rod length, which after some simplification, reduces to:

$$u = \frac{V}{1 + \dfrac{L[1 - (P_r + P_{cp})/P_\infty]}{T_c}} . \tag{6}$$

The R_t's calculated using this methodology are listed in Table 2 under the column R_t (2).

The calculated target resistances are plotted in Fig. 16, but the data are displayed somewhat differently than the data in Fig. 15. The differences in the calculation of R_t from Eqns. (4) and (5-6) are used, along with the spread in the experimental data, to estimate the uncertainties in R_t. (The sample standard deviation is used to give an estimate of the uncertainty.) The two "anomalous" data points, Test Nos. 31 and 22, are plotted separately, denoted by the open circles. The same conclusions can be drawn from Fig. 16 as Fig. 15.

Comparison with Data from Similar Investigations. Measures of performance such as E_m or P_T/L, are strongly dependent on the semi-infinite steel reference penetration. For example, changing the hardness of the steel substrate material can change E_m by as much as 30% [33]. An advantage of calculating Δe_c or R_t is that these measures of performance can be more readily compared with results from similar experiments by other investigators since the reference penetration is taken into account to estimate tile performance. In particular, by expanding the database, the data from this study can be compared to ceramic performance at other impact velocities and tile thicknesses. We will examine data from Woolsey, *et al.* [29-30,34], Wilkins, *et al.* [33], and Hohler, *et al.* [35], and compare Δe_c. The calculation of Δe_c requires the baseline penetration performance P_∞ of the projectile into the semi-infinite substrate material. The reference performance for the Woolsey, *et al.*, experiments is shown in Fig. 2, that of Wilkins, *et al.*, and Hohler, *et al.*, are reported in Refs. [33] and [35], respectively.

Woolsey, *et al.*, used square tiles, 15.24 cm on a side. The tiles were confined laterally in a 1.9-cm thick steel frame; tile thicknesses were varied between 1.0 and 4.0 cm. The substrate material was RHA, with a hardness of R_C 27±2. Woolsey provides only P_r adjusted to the nominal impact velocity of 1.49 km/s, so all data are shown at that impact velocity. Woolsey tested many different ceramic materials (using *L/D* 10 tungsten-alloy projectiles), but only the results for Coors

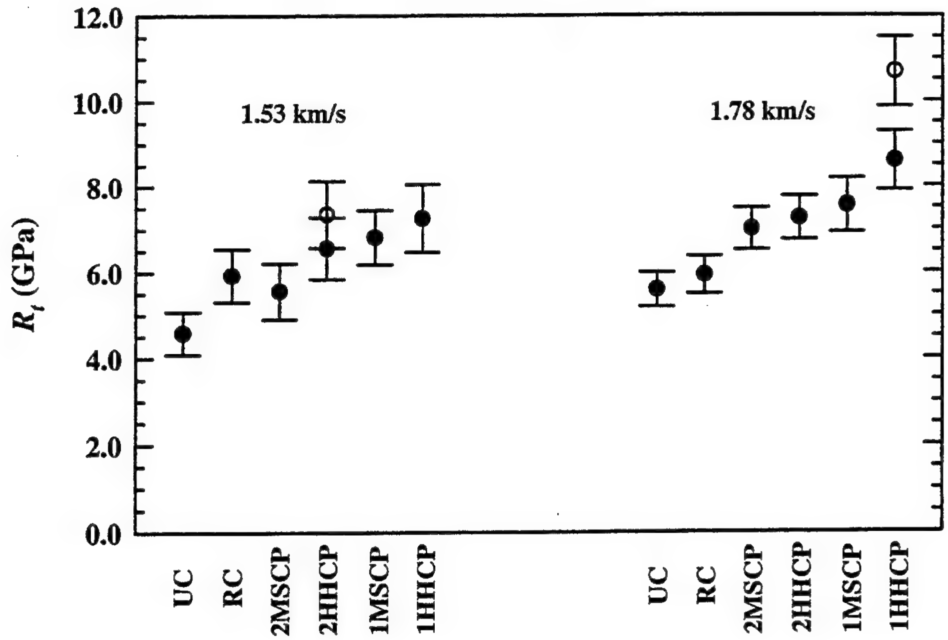

Figure 16. Tate Resistance

99.5% Al_2O_3, with a reported density of 3.89 g/cm^3, will be discussed here. The 1.0-cm thick tile results are not plotted since these clearly are not representative of (and are considerably below) the results for the thicker tiles. Examination of their data shows that ballistic performance, as measured by Δe_c, falls into two distinct categories. Most of the data yield a differential tile efficiency of approximately 2.0, independent of tile thickness (1.9 cm $\leq T_c \leq$ 4.0 cm). Occasionally, however, the ceramic performs better, with a Δe_c of approximately 2.7. Both of these values are plotted in Fig. 17, along with an estimate of the uncertainties calculated from the spread in the experimental data. Also plotted in Fig. 17 are the averaged values for the unconfined and radially-confined ceramic tiles from this study, Fig. 15. The lower value for Δe_c (~ 2.0) from Woolsey, *et al.*, agrees quite well with the present "confined" experiments. At approximately 1.5 km/s, the unconfined 10-cm diameter tile (open square symbol) does not provide sufficient inertial confinement, and ceramic performance, as measured by Δe_c, is 25% less than the radially confined tile (solid square) or the larger tiles used by Woolsey, *et al.* At 1.78 km/s, as already noted, the unconfined tile performance is only marginally less (4-5%) than that of the radially confined tile, and within the scatter of the data of Woolsey, *et al.*, for tiles with thicknesses of 1.9 to 4.0 cm.

The data from Woolsey, *et al.*, demonstrates that ceramic performance, under nominally identical test conditions, can vary by approximately 30% (Δe_c's of ~ 2.0 and ~ 2.7). Similar behavior is observed in the data in Fig. 15, specifically Test Nos. 22 and 23 (the open triangles at ~ 1.78 km/s), where performance differs by approximately 25%. Exactly why ceramic tile performance can vary so dramatically is unknown, although there has been considerable speculation.

In Refs. [33] and [35], square tiles (10.0, 15.0, or 18.0 cm on a side) were wedged into a 2.0-cm thick steel frame. The substrate material was a German armor steel with a hardness of R_C 40±1. A 1.0-cm thick mild steel cover plate ($T_{cp}/D \approx 1.46$) was placed in front to provide further confinement of the ceramic, but with a 3.0-cm diameter hole for projectile impact. A 0.15-cm thick piece of rubber was placed between the mild steel cover plate and the ceramic for damping.

In the Wilkins, *et al.,* work [33], total tile thickness was varied between 7.0 and 9.0 cm. The target was assembled by using a two-part adhesive to stack 3.0 and 4.0-cm thick tiles until the total thickness of 7.0, 8.0, or 9.0 cm was achieved. The 99.5% Al_2O_3 tiles were made by Dow Chemical, and had a density of 3.87 g/cm^3. The impact velocities were nominally 2.0 and 2.5 km/s. These results are plotted in Fig. 17. On average, there is a slight increase in tile efficiency between 1.95 and 2.45 km/s (8%). However, on average, ceramic performance for the DOW ceramic is approximately 12% less than the new data presented here or the data of Woolsey, *et al.* [34]. This decrease in performance is likely due to the substantially increased tile thickness as discussed in the paragraphs below.

Hohler, *et al.* [35], conducted experiments on Al_2O_3 tiles (trade name Al898), with a nominal density of 3.8 g/cm^3, manufactured by Hoechst CeramTec. Total ceramic thicknesses were varied between 1.98 cm and 10.0 cm by stacking nominally 2.0-cm thick or 1.0-cm thick tiles together. Tungsten-alloy long rods (*L/D* 10 and 12.5) were fired at approximately 1.25, 1.7, 2.5, and 3.0 km/s. The authors show that Δe_c decreases with increasing tile thickness. Yaziv and Partom [36] found similar behavior with AD-85 tiles, using an impact velocity of 1.38 km/s, but they also found that the effect was considerably less pronounced if the tile was radially confined. Likewise, Hauver, *et al.* [24], show a decrease in R_t for increasing tile thickness for a number of different ceramic materials.

For the purposes here, Δe_c was calculated from the data in Ref. [35] for the 2.0 and 3.0-cm thick tiles and averaged. The difference in the two results provide an estimate of an uncertainty.

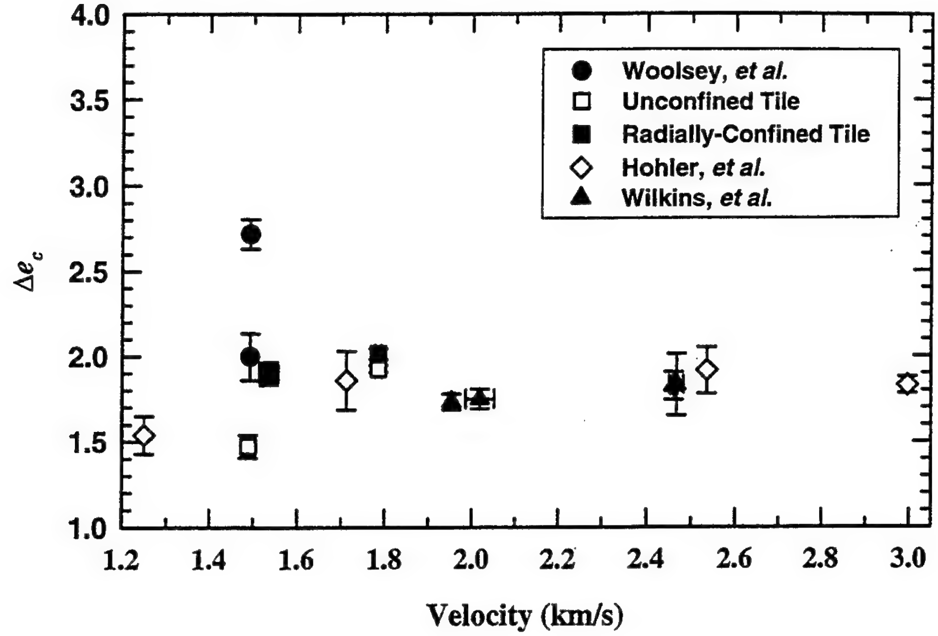

Figure 17. Comparison of results with the results of other investigators

The results are plotted in Fig. 17. Although Hohler, *et al.*, report a decrease in Δe_c with increasing tile thickness, the effect becomes less and less pronounced as the impact velocity increases. Their at 3.0 km/s is relatively independent of tile thickness; for example, for 8.0 cm of ceramic, Δe_c is only 6% less than the value shown in Fig. 17.

Several observations can be made, consistent with those already stated, concerning the Hohler, *et al.*, [35] data. There is an increase in ceramic performance with impact velocity between 1.25 km/s and 1.7 km/s. From 1.7 km/s to 2.5 km/s, there is a very slight improvement in performance on average, which then decreases slightly at 3.0 km/s. However, within the data scatter, ceramic performance is approximately constant with impact velocity for $V \geq 1.7$ km/s.

2.5 Summary

The ballistic performance of a ceramic tile improves with confinement. As shown in Figs. 15 and 17, performance is velocity dependent, but the more the confinement, the less the dependence on impact velocity. Within the data scatter, the data of Hohler, *et al.* [35], Wilkins, *et al.* [33], Woolsey, *et al.* [34], the radially-confined data at 1.53 km/s, and both the unconfined and radially-confined data at 1.78 km/s agree quite well. The ballistic performance of a ceramic tile is quite

sensitive to changes in confinement at low impact velocities ($V \leq 1.5$ km/s). The results of Refs. [35, 36] show that tile performance is a function of tile thickness at the lower impact velocities, although Yaziv and Partom [36] report that this dependence is less for a radially-confined ceramic. Additionally, for a given confinement, ceramic performance is relatively sensitive to impact velocity for $V \leq 1.5$ km/s. Ceramic performance appears to increase slowly until $V \sim 2.5$ km/s. At higher impact velocities, performance, within the data scatter, is constant.

From analysis of the results with cover plates, it has been demonstrated that ceramic performance is dependent on both the thickness and hardness of the cover plates used. The fact that tile performance decreased with an increase in cover plate thickness suggests that there is some optimum thickness for cover plate performance. Lastly, at the higher impact velocities ($V > 1.7$ km/s), provided there is adequate confinement, the ballistic performance appears to be only moderately sensitive to tile thickness for the conditions examined. The data of Woolsey, *et al.* [34], at $V = 1.49$ km/s, also showed little thickness dependency implying that their test protocol provides adequate confinement for the thickness for tiles tested.

3.0 CERAMIC COMPUTATIONS[1]

3.1 Introduction and a Constitutive Model for Brittle Materials

The observations discussed in Section 2.0 establish necessary conditions for the behavior of a robust computational model for ceramic materials. Generally, ballistic impact experiments have been required to determine some of the constants in ceramic constitutive models, in particular, the flow stress of the comminuted material. Therefore, to ensure that agreement is not a result of "tuning" of the constitutive constants to one impact velocity, the experiments described in Section 2.0 were designed to obtain data at two different impact velocities. Thus, issues of confinement and impact velocity are addressed in the same test matrix, and the experimental data serve as benchmark data for numerical simulations.

3.2 Johnson-Holmquist Model for Brittle Materials

Johnson and Holmquist developed a phenomenological model to define the elastic limit behavior of brittle materials such as ceramics and glass [37]. This model, referred to as JH-1, includes pressure-dependent strength, damage and fracture, strength after fracture, bulking, and strain-rate effects. A revised model, referred to as JH-2, was developed to address concerns in the original model [38]. A general overview of the model is shown in Fig. 18. The figure is divided into three sections: strength, damage, and pressure. The features of the model are as follows:

- The strength of the ceramic is a function of damage D, strain rate $\dot{\varepsilon}$, and confining pressure P.

- The strength and pressure are normalized by the strength and pressure, σ_{HEL} and P_{HEL}, respectively, at the Hugoniot Elastic Limit (HEL). The normalized maximum tensile hydrostatic pressure is $T^* = T/P_{HEL}$, where T is the maximum tensile hydrostatic pressure the material can withstand. The normalization procedure allows many of the constants to be dimensionless. This is helpful when comparing different materials, and when

[1]The authors would like to acknowledge and thank Gordon R. Johnson and Tim J. Holmquist for performing the computations described in this section.

estimating constants for materials that have an insufficient data base to determine constants.

- The material softens as damage accumulates ($D > 0$). This allows for gradual softening as a function of increasing equivalent plastic strain. (The JH-1 model does not soften until $D = 1.0$, whereupon the "softening" occurs instantaneously.)

- The strength of the intact ($D = 0$) and fractured ($D = 1.0$) material is essentially a Mohr-Coulomb model, that is, the strength is a function of confining pressure. However, there can be a "cap" on the strength of the fractured material, designated as SFMAX in the figure.

- Strength and damage are analytic functions of the pressure (and strain rate for the strength). This more readily allows for parametric variation of the constants in an easier and more systematic manner than for the JH-1 model, which uses multiple linear segments.

- The strength is generally a smoothly varying function of the intact strength, fracture strength, strain rate, and damage, which is better suited for numerical implementation.

- Damage accumulates with equivalent plastic strain. The material cannot undergo any plastic strain at $P^* = -T^*$, but as seen in Fig. 18, the equivalent plastic fracture strain ε_p^f increases with confining pressure.

- After damage begins to accumulate ($D > 0$), bulking (pressure increase and/or volumetric strain increase) can occur. The incremental pressure increase ΔP is determined from energy considerations. The internal energy associated with the decrease in elastic energy due to a decrease in shear and deviatoric stresses is converted to potential internal energy by increasing the pressure. A constant β ($0 \le \beta \le 1$) is used to vary the fraction of elastic energy lost that can be converted to potential hydrostatic energy. The expressions for the pressure and for the calculation of ΔP are shown at the bottom of Table 3.

The model constants are *A, B, C, n, m,* SFMAX, D_1 and D_2. In general, the constants are determined from quasi-static uniaxial stress compression tests, dynamic uniaxial stress compression tests (using a split-Hopkinson bar), quasi-static biaxial tests, and uniaxial strain flyer plate tests. The HEL values are determined from the flyer plate tests.

The constants for the 99.5 Al_2O_3 ceramic were obtained in a manner similar to that presented by Holmquist, *et. al.* [39], except that some constants were estimated due to lack of experimental data. Specifically, the plate impact experiments by Grady [40], and the penetration experiments

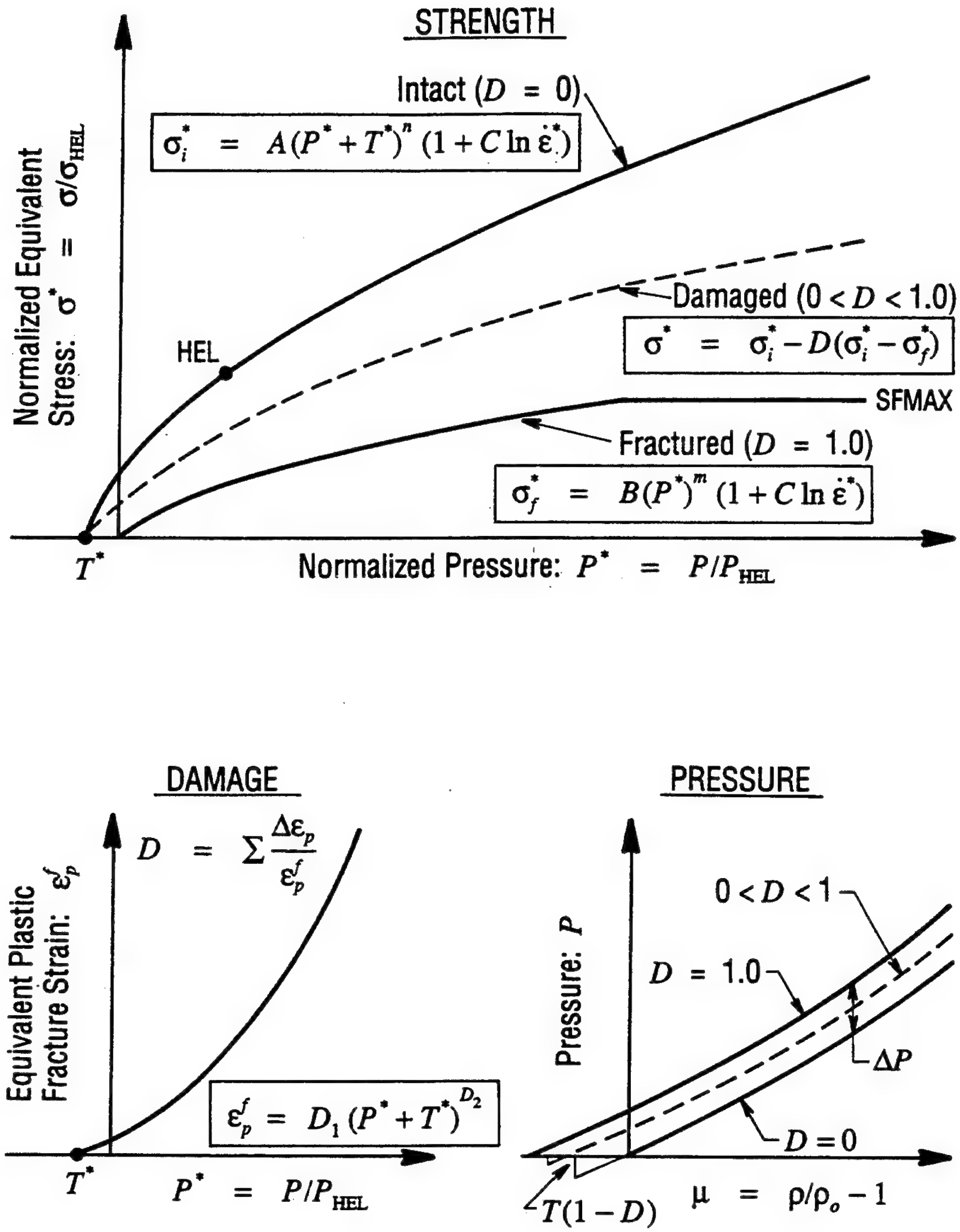

Figure 18. JH-2 model for brittle materials (from Ref. [38])

Table 3. JH-2 Constants for AD-99.5 Alumina

Density	ρ_o =	3890 kg/m^3
Shear Modulus	G =	152 GPa
Hugoniot Elastic Limit	HEL =	6.57 GPa
Intact Strength Constant	A =	0.88
Intact Strength Constant	n =	0.64
Strain Rate Constant	C =	0.007
Fracture Strength Constant	B =	0.28
Fracture Strength Constant	m =	0.60
Maximum Fracture Strength	SFMAX =	1.0
Tensile Strength	T =	0.262 GPa
Pressure Constant	k_1 =	231 GPa
Pressure Constant	k_2 =	-160 GPa
Pressure Constant	k_3 =	2774 GPa
Bulking Constant	β =	1.0
Damage Constant	D_1 =	0.01
Damage Constant	D_2 =	0.70

$$P = k_1\mu + k_2\mu^2 + k_3\mu^3 + \Delta P$$

$$\Delta P_{t+\Delta t} = -(k_1\,\mu_{t+\Delta t}) + \sqrt{(k_1\mu_{t+\Delta t} + \Delta P_t\,)^2 + 2\;\beta\, k_1\,\Delta U}$$

$$\Delta U = U_{D(t)} - U_{D(t+\Delta t)}$$

$$U = \sigma_{eq}^2 / 6G$$

by Hohler, Stilp, and Weber [35], were used to determine the constants shown in Table 3. Figure 19 shows the normalized strength versus normalized confining pressure for the AD-99.5 ceramic material. Figure 20 shows a comparison of experimental plate impact data [40] with computed results using the ceramic constants of Table 3. The computed results are in good agreement with the experimental data.

3.3 EPIC Calculations of Ballistic Experiments

A series of computations was performed to determine the ability to simulate accurately the confinement effects observed in the experiments described in the last section. The computations were performed with the SPH (Smooth Particle Hydrodynamics) option in the EPIC code [41]. The computations used the JH-2 model for the ceramic; and the Johnson-Cook strength [42] and fracture [43] models for the metals.

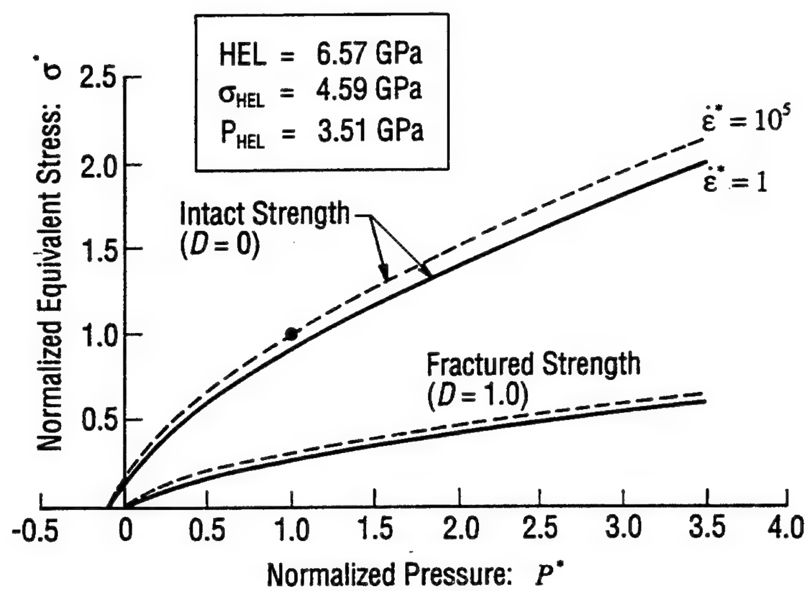

Figure 19. Normalized strength versus normalized confining pressure

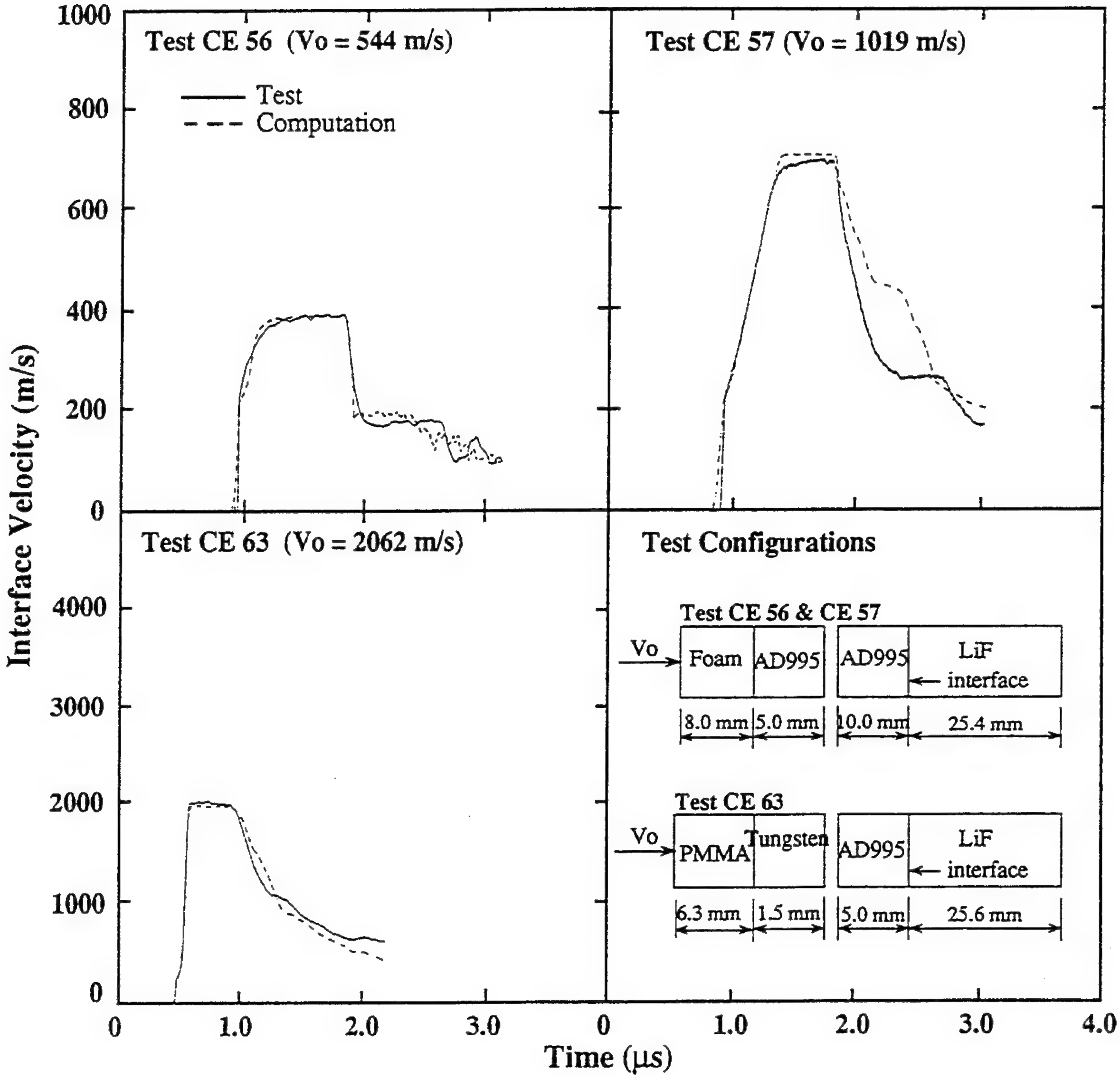

Figure 20. Experimental and computational results for plate impact tests on AD-99.5 alumina

Computations for some of the penetration experiments are shown in Figs. 21 and 22. Results are provided for the single cover plate configuration only. SPH nodes are used in the regions where there are large deformations. The mottled color represents SPH nodes, and the remaining regions are represented by standard quad elements. The standard elements are used to reduce

Table 4. Comparison of Results at $V = 1.52$ km/s

Target Configuration	Test P_T/L	Computed P_T/L
Steel Only	0.87	0.78
Unconfined Ceramic	0.93	0.85
Radially- Confined Ceramic	0.91	0.84
Mild Steel Cover	0.87	0.84
High Hard Cover	0.82	0.85

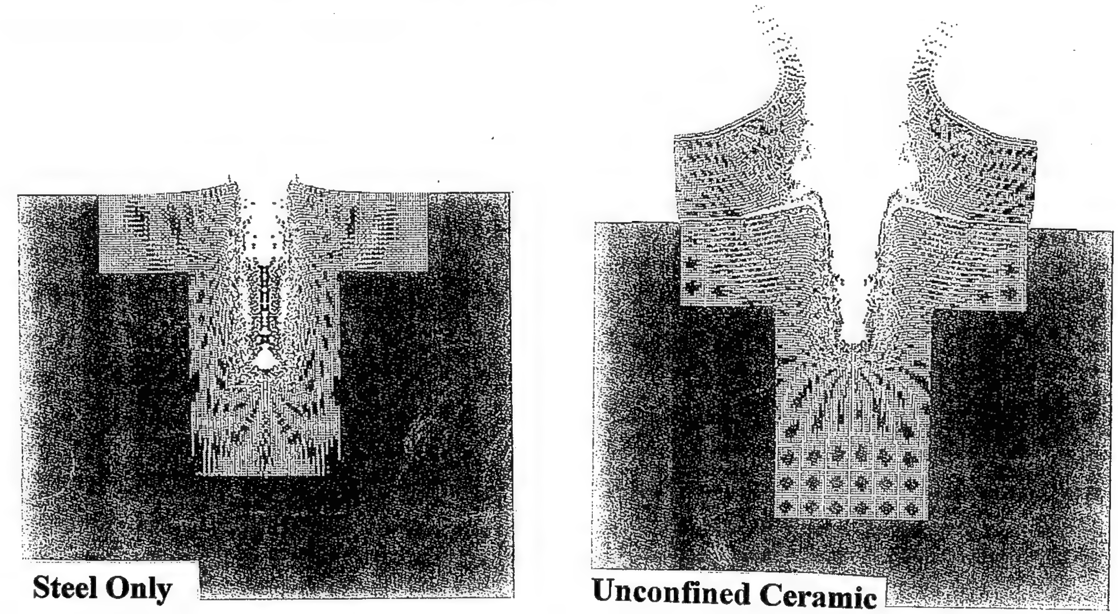

Figure 21. Computed penetration results at $t = 120$ µs for $V = 1.52$ km/s

Table 5. Comparison of Results at $V = 1.79$ km/s

Target Configuration	Test P_T/L	Computed P_T/L
Steel Only	1.15	1.01
Unconfined Ceramic	1.16	1.04
Radially-Confined Ceramic	1.14	1.01
Mild Steel Cover	1.02	1.01
High Hard Cover	0.96	1.00

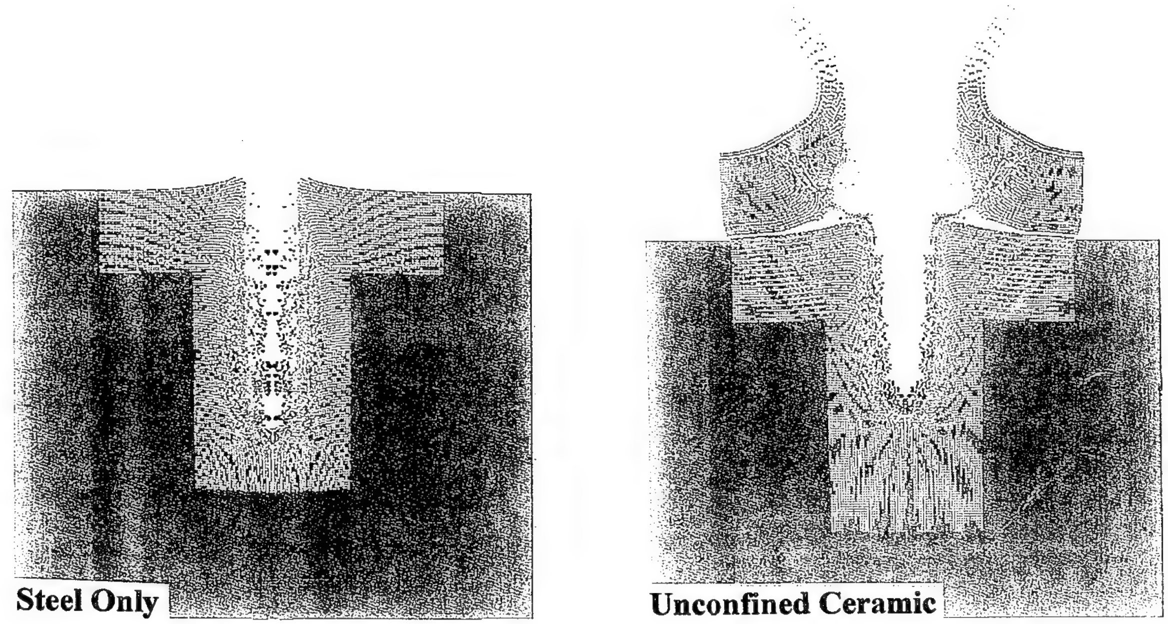

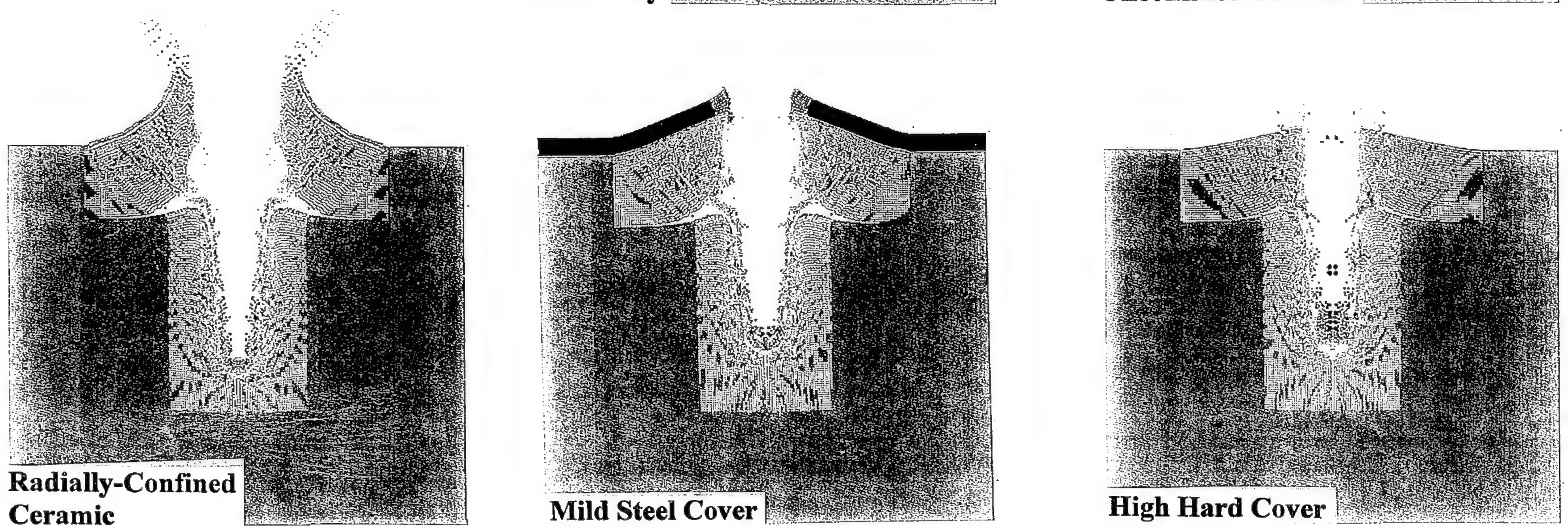

Figure 22. Computed penetration results at $t = 120$ μs for $V = 1.79$ km/s

the number of SPH nodes since the SPH algorithm requires more CPU time. The SPH nodes are attached (bonded) to the steel target, but they are allowed to slide along the lower surface of the cover plate. The diameter of all the SPH nodes is 0.152 mm, which gives five nodes across the radius of the tungsten rod. The Johnson-Cook strength constants for the 4340 steel target are given in Ref. [42], and those for the high-hard steel plate are given in Ref. [44].

Figure 21 depicts the results for a nominal impact velocity of 1.52 km/s. The normalized penetrations from the computations, P_T/L, are compared to the experimental results in Table 4. The computed penetration into the steel target (no ceramic present) is $P_T/L = 0.78$ and the experimental penetration is $P_T/L = 0.87$. The underprediction of the computed penetration is probably due to the coarse SPH grid and the SPH viscosity that can introduce additional resistance for this type of problem [45]. The computed penetration for the unconfined ceramic (Fig. 21b) is slightly more than for the radially-confined ceramic (Fig. 21c), and this is expected because the latter has more confinement. The increased confinement leads to increased pressures, which then leads to increased strength in the ceramic.

The mild steel cover plate bulges upward more than the high hard steel plate, Figs. 21d and 21e, which is consistent with the experiments, but the computed bulges are less than observed in the experiments. The cover plate computations were repeated with no bulking ($\beta = 0$), and the results were similar to those shown in Fig. 21. In general, the experimental data clearly show more target resistance for the cover plate configurations, but this is not predicted by the computations. The results for an impact velocity of 1.79 km/s are shown in Fig. 22. The computational results are compared to the experimental results in Table 5; the trend of these results is similar to the lower velocity results.

Why are the computations insensitive to changes in cover plate configuration? A comparison of a computation for a radially-confined ceramic with no cover plate to a run with a cover plate ($V = 1.79$ km/s) is shown in Fig. 23. At 4 μs, with no cover plate, the ceramic has failed all the way to the steel substrate, although penetration is only approximately one-half projectile diameter. With the cover plate, there is extensive damage to the ceramic at 4 μs, even though the projectile has only penetrated half the thickness of the cover plate. At 12 μs, the extent of fracture of the ceramic is similar for both configurations. Note that with the cover plate, the projectile is approximately at the same depth within the ceramic tile at 12 μs (Fig. 22d) as it is at 4 μs with no cover plate (Fig. 22a). Therefore, the computations show that the ceramic

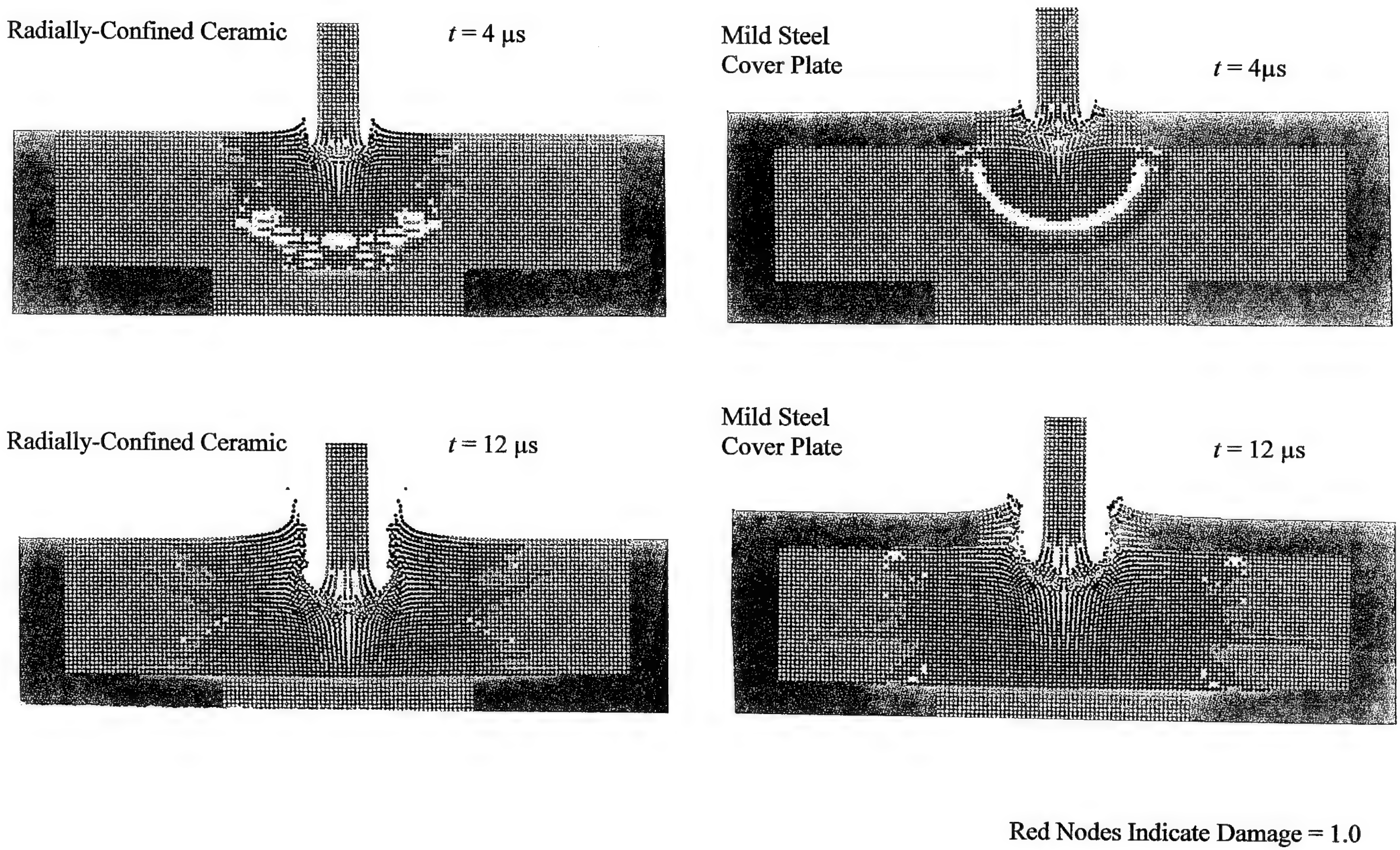

Figure 23. Comparison of ceramic fracture with and without cover plates (V = 1.79 km/s)

under the cover plate is fractured before the projectile penetrates the cover. The result is that the ceramic is fractured, and thereby weakened, before it is penetrated by the tungsten rod. Even though the cover plate partially confines the ceramic, the strengthening effect of the confinement does not offset the weakening effect of the early fracturing of the ceramic.

The reason for the discrepancy between the experimental and computational results is not clear. The source of the "error" could be the ceramic model, the constants for the model, the SPH algorithm or the modeling of the interfaces, or insufficient zonal resolution. The SPH technique is relatively new and is currently under development and evaluation. It is known that inaccuracies are introduced at material interfaces [46] and this could be an explanation. Additionally, in the experiments, the ceramic element was prestressed by the cover plate. There was no attempt to provide a prestress in the computations; however, from Fig. 18, it is seen that ε_p^f can be quite sensitive to confining pressure, e.g., a prestress.

3.4 Summary

Dehn [47] has had success, using the wavecode HULL, in modeling the experiments of Hauver, *et al.* [48, 49]. These experiments show the importance of attenuators, cover plates, interface materials, and confinement. However, Dehn has had to artificially increase the strength of the ceramic [50] in order for the computations to match the experiments.

The approach in this study has been to obtain constitutive constants from independent experiments and then compare the results to a set of ballistic experiments (with no changing of the constitutive constants). Overall, the computations correctly predict the total penetration to first order as a function of impact velocity. However, the computations do not capture the effects of differences in confinement which are clearly observed in the experiments. The results of the computations show promise, but work remains. The discrepancies between computational and experimental results could be related to numerical issues or constitutive issues. Since these two issues are coupled in the calculations, it is difficult, at this point, to identify the cause of the discrepancies.

4.0 EXPERIMENTS AND MODELING OF GLASS

4.1 Introduction

The final depth of penetration typically provides the only link between experiments and the results of numerical simulations, although occasionally crater diameters are also compared. Flash radiography can be used under certain conditions to determine the positions of the projectile/target interface and the projectile tail, and hence the instantaneous length of the projectile, at specific instances of time during the penetration process. Unfortunately, this information is considerably more time consuming and expensive to obtain, and the ability to "see" through the target constrains the dimensions of the targets that can be used in the experiments. Numerical simulations of long-rod penetration into steel and titanium targets were compared to a limited set of time-resolved X-ray data in Ref. [51]. Agreement between the numerical simulations and the experimental data was adequate, but certainly could be better. The discrepancies were attributed to the fact that the constitutive behavior of the materials used in the experiments had to be estimated. Since the focus of the work in Ref. [51] was on an examination of the time dependence of the target resistance R_t that is used in the Tate model [52], no attempt was made to determine more accurate constitutive parameters.

Twenty experiments, using L/D = 12.5 tungsten alloy projectiles at two impact velocities (1.25 and 1.70 km/s), were conducted on high-hard steel targets in Ref. [12]. Flash radiography was used to obtain the positions of the projectile nose and tail, and the projectile length, at various times. Constitutive constants had been determined for materials similar to those used in the experiments, so a critical comparison could be made between the numerical simulations and the experimental data. The computational predictions of the penetration-time behavior were in good agreement with the experiments. Although the computations were not able to reproduce exactly the experimentally-observed ballistic limit conditions, the computations did show a strong sensitivity to initial conditions near the ballistic limit, i.e., the computations displayed the expected qualitative behavior near the ballistic limit. The quantitative disagreement between the computations and the experiments was attributed to the inadequate treatment of material failure at breakout.

The present paper describes the results of a fairly large number of experiments into glass targets. The penetration of glass is contrasted to the penetration of steel targets. Different functional forms for the constitutive behavior of glass were used in numerical simulations of the experiments.

4.2 Experimental Procedures and Results

The experimental arrangement is depicted in Fig. 24. Blunt-nosed, tungsten-sintered alloy projectiles, 5.8 mm in diameter with a length-to-diameter (*L*/*D*) ratio of 12.5, were impacted against glass targets at a velocity of 1.25 and 1.70 km/s; the target obliquity was 0°.[2] The tungsten-sintered alloy had a density of 17.6 g/cm^3 (92.5% W, 4.85% Ni, 2.4% Fe, 0.25% Co) and a yield strength of 1.20 GPa (elongation at failure was 10%); the rods were manufactured by Metallwerk Plansee, Reutte, Austria.

The glass targets were constructed from 10 single sheets of 1.9-cm thickness each, held together by double-sided adhesive plastic foil (0.014-cm thick). An eleventh glass plate, thickness of 1.0 cm, brought the overall target thickness[3] to 20.0 cm. The glass targets were backed by a mild steel confinement block. The lateral dimensions of the plates were 15 cm by 15 cm. Two of the experiments were performed with 30-cm x 30-cm wide glass plates to investigate if there was any influence of the lateral dimensions. The experimental results were independent of this doubling of the lateral dimensions. The glass was a standard float (window) glass, with a density of 2.5 g/cm^3. The Vickers hardness was 430 ± 20. The compressive strength was determined to be 0.90 GPa, the bending strength was 30-90 MPa, and Young's modulus was 83 GPa.

Pictures of the penetration process were taken with a 600 kV flash X-ray, triggered at the moment of impact by a thin copper "shorting" screen. One shadowgraph per test was taken; the delay time from the trigger was changed for each test to record the projectile at different penetration positions. All tests and data analysis were conducted at the Ernst-Mach-Institut (EMI). The test numbers and impact conditions for the tests are given in Tables 6 and 7. In a few cases, the

[2] The projectiles had a conical-like drag cone (1.2 cm long, with a maximum diameter of 1.6 cm at 0.6 cm behind the base of the projectile), made from titanium, press-fitted onto the cylindrical rod. The drag cone added approximately 3-g mass (3%)to the ideal cylindrical rod.

[3] The measurement of total target thickness consists of the thicknesses of the glass and adhesive.

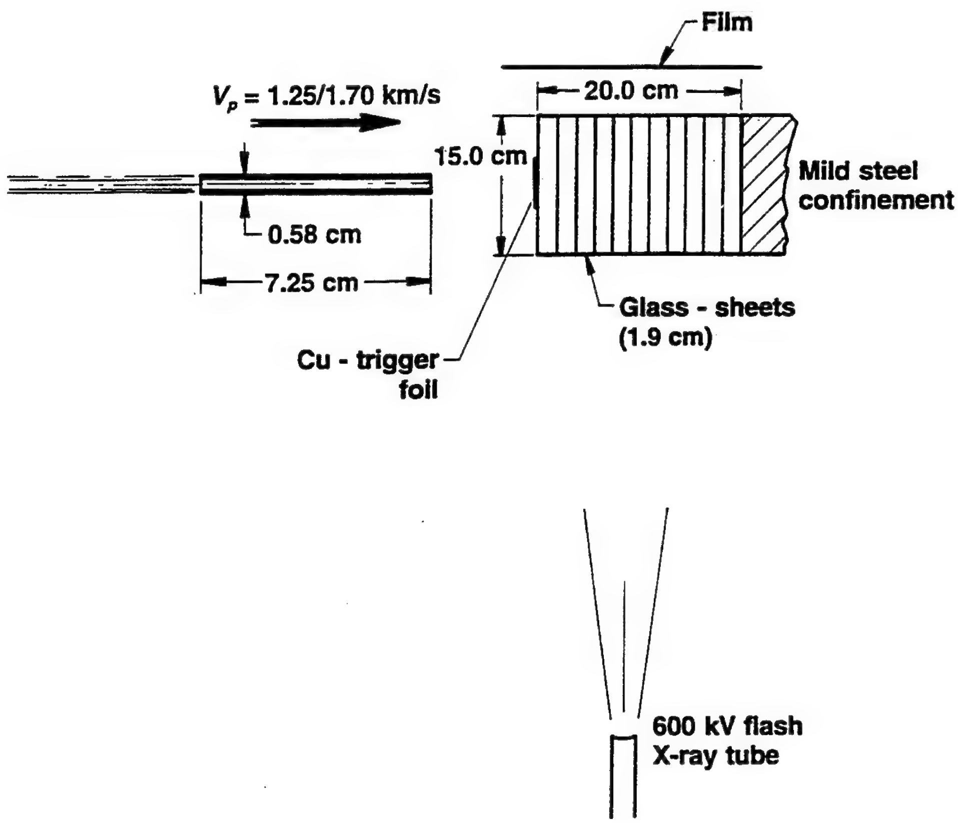

Figure 24. Schematic of experimental arrangements for glass targets

projectile was recovered in the impact tank so that its length could be measured; these values are given in the last column of Tables 6 and 7.

The positions of the projectile nose and tail, S_K and S_H respectively, defined in Fig. 25, were determined from the X-ray shadowgraph. Additionally, the length of the projectile, L_R, was independently measured. Because S_K, S_H, and L_R are independent measurements, the following expression provides a consistency check on the data:

$$L_o - L_R = S_H - S_K \tag{7}$$

The experimental spread in the impact velocities was ±20 m/s. The experimental data for S_K and S_H were corrected to exactly 1.25 and 1.70 km/s by a simple proportionality at the measured

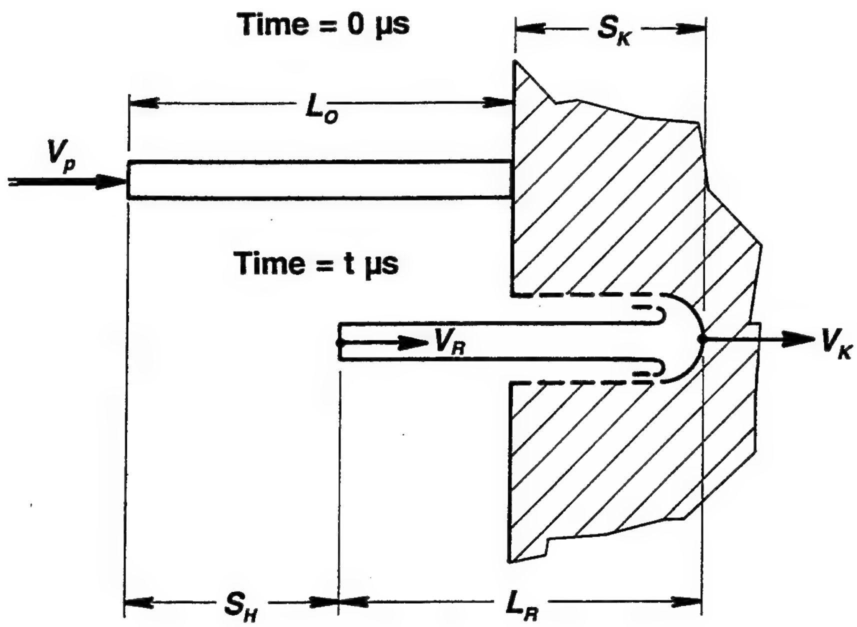

Figure 25. Nomenclature and measured quantities from flash X-rays

time; i.e., $(S_K)_{adj} = (V_p / V_{exp})\ (S_K)_{exp}$ and $(S_H)_{adj} = (V_P / V_{exp})\ (S_H)_{exp}$ where V_{exp} is the actual (experimental) impact velocity and V_p is 1.25 or 1.70 km/s. No adjustment to the time was performanced, i.e., $t = t_{exp}$. The "corrected" experimental data are given in Tables 8 and 9 for the two impact velocities, respectively[4].

A modified target was constructed for some of the tests to provide an estimate of the projectile velocity at different depths of penetration, denoted by the symbol S_K'. This experimental configuration is shown in Fig. 26. The glass portion of the target was made S_K' thick, and the projectile was allowed to exit the target through a 3.0-cm wide cavity drilled into the mild steel backup plate. A 4.5-cm wide, 1.5-cm thick, honeycomb sheet was placed at the rear of the glass

[4]The accuracy of the measurements is as follows. The times of the flash X-rays are correct to ± 0.2 μs (this includes the time interval counter and the short circuit trigger foil). The uncertainty in the impact velocity is ± 0.002 V_p, which is approximately ± 3 m/s for the impact velocities used in these tests. The positions of the nose and tail, measured from the flash X-ray pictures, are accurate to ± 0.1 mm; the uncertainty in the position of the target surface is also ± 0.1 mm. This leads to an uncertainty in S_K, S_H, and L_R of ± 0.2 mm.

Table 6. Impact Velocity, Pitch and Yaw, and Residual Projectile Length: $V_p \approx 1.25$ km/s

Experiment No.	V_p (km/s)	Pitch/Yaw (°/°)	L_R^* (cm)
5758	1.254	0.5/<1	
5753†	1.235	0/<1	
5757	1.264	0/<1	
4638	1.251	0/0.9	
5754	1.266	0.5/<1	
5756	1.270	0.3/<1	
5755	1.248	0.5/<1	
5744	1.266	0.5/<1	
4637	1.247	3.0/1.5	
4624	1.264	0/0.9	
4636	1.251	0.5/1.0	
4625	1.249	1.4/0.2	
4634	1.246	1.2/1.4	
4628	1.244	0.6/0.6	
4631	1.247	2.3/0.3	
4626	1.253	1.1/0.1	
4633	1.255	1.6/1.9	1.65
4627	1.267	2.3/2.4	2.00
4640	1.255	0.7/0.4	
4648	1.233	0.1/0.6	1.85
4649	1.231	0.1/0.4	
4643	1.272	0/1.4	

†Lateral dimensions of glass were 30.0 cm x 30.0 cm.

Table 7. Impact Velocity, Pitch and Yaw, and Residual Projectile Length: $V_p \approx$ 1.70 km/s

Experiment No.	V_p (km/s)	Pitch/Yaw (°/°)	L_R^* (cm)
5747	1.690	0.5/<1	
5746	1.690	0/<1	
5752†	1.695	0/<1	
4645	1.679	0.5/0.5	
5742	1.678	0.5/<1	
5759	1.711	0.3/<1	
5749	1.700	7.4/?	
5750	1.708	0.5/<1	
5748	1.683	4.3/<2	
5751	1.706	1/<1.5	
4644	1.719	1.1/2.8	
4646	1.686	1.9/0.4	
4647	1.710	0.4/0.9	
4689	1.695	0.2/1.2	1.10
4694	1.963	0.4/1.5	1.15
4693	1.680	0.6/1.9	
4695	1.702	0.8/1.6	1.15
4697	1.704	0.4/1.9	
4698	1.700	0.4/0.5	1.10
4699	1.698	0.6/2.0	

†Lateral dimensions of glass were 30.0 cm x 30.0 cm.

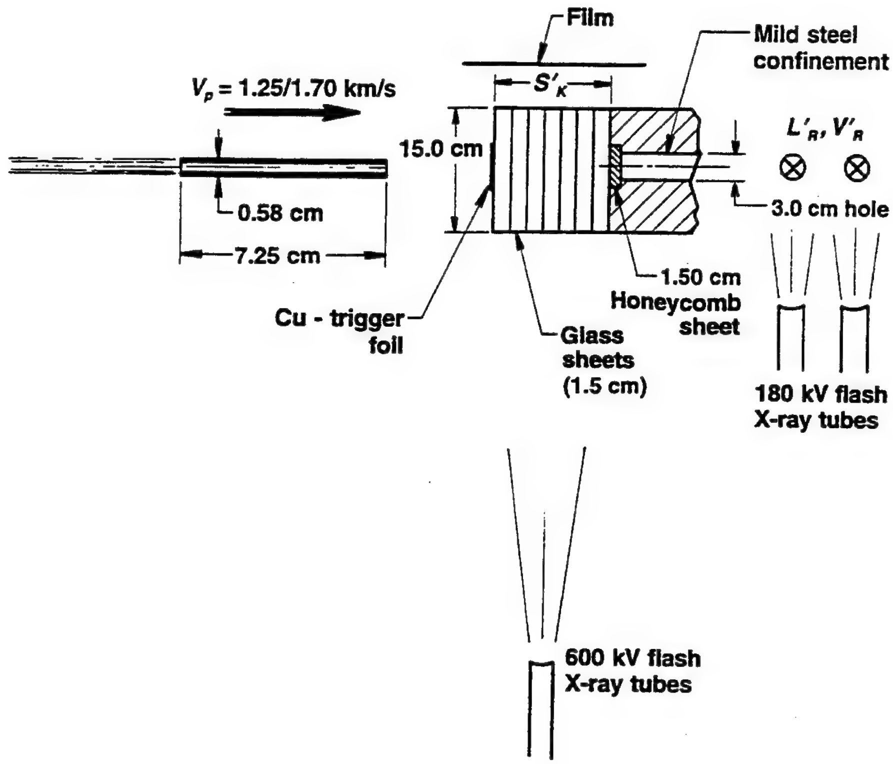

Figure 26. Schematic of modified experimental arrangement for glass targets

plates to provide confinement but minimize penetration/perforation resistance. The glass plates in these targets were 1.5-cm thick. Flash radiography was then used to obtain V_R' and L_R' behind the target. Since S_K' is a specified distance, it was not changed according to the "correction" algorithm described in the previous paragraph. Instead, t' was found from the penetration-time data (S_K versus time) for the designated penetration depth of S_K' (V_R' was adjusted, however, by an analogous formula to correct it to an impact velocity of 1.25 or 1.70 km/s). All data values are given in Tables 8 and 9.[5] In addition, the 600kV flash X-ray was used to provide *in situ* measurements of the penetration depth and projectile length at early times to supplement the data collected in the Fig. 24 arrangement.

[5] Column 1 in Tables 6-9 provide a four-digit experiment number. The experiments that have the prefix of "46" were performed using the test configuration of Fig. 24. The experiments that have the prefix "57" were performed using the test configuration of Fig. 26.

Table 8. Penetration into Glass: $V_p = 1.25$ km/s

Experiment No.	S_K (cm)	S_H (cm)	L_R (cm)	t (μs)	L_R' (cm)	V_R' (km/s)	S_K' (cm)	t' (μs)
5758	0.87	1.31	6.81	10.5	0.78/3.2†	1.005	6.04	83.9
5753	1.29	1.97	6.57	15.7	2.55	0.784	8.86	131.0
5757	1.44	2.19	6.50	17.5	1.14/1.92†	0.784	9.07	134.7
4638	1.66	2.49	6.42	20.2				
5754	1.70	2.57	6.38	20.6	1.71	0.667	10.35	158.5
5756	1.76	2.83	6.18	22.5	3.18	0.921	7.47	107.1
5755	2.02	3.20	6.07	25.6	1.04/1.91†	0.770	8.83	130.5
5744	2.46	3.74	5.97	30.5				
4637	3.07	4.77	5.55	39.9				
4624	3.69			49.4				
4636	5.06			69.9				
4625	5.76	9.34	3.67	80.1				
4634	6.13	9.90	3.48	84.7				
4628	7.09	11.50	2.84	99.9				
4631	7.83	12.48	2.60	111.1				
4626	8.30	13.12	2.43	120.7				
4633	9.27	14.63	1.89	139.9				
4627	9.73	15.12	1.86	150.5				
4640	10.58	16.01	1.82	159.6				
4648	11.55	17.05	1.99	189.4	tumbling			
4649	~12.9	~18.75	1.60	219.9	tumbling			
4643	~12.8	~19.45	1.85	300.4	tumbling			

†Residual rod was broken into two pieces, the lengths of each piece are given.

Table 9. Penetration into Glass: $V_p = 1.70$ km/s

Experiment No.	S_K (cm)	S_H (cm)	L_R (cm)	t (μs)	L_R' (cm)	V_R' (km/s)	S_K' (cm)	t' (μs)
5747	1.27			10.5	2.37	1.308	10.39	96.1
5746	1.79	2.64	6.40	15.5				
5752	1.78	2.64	6.39	15.5	1.30	0.939	13.40	131.6
4645	2.41	3.35	6.31	19.7				
5742	2.42	3.43	6.24	20.5				
5759	2.40	3.53	6.12	20.7	4.34	1.561	5.90	52.1
5749	2.96	4.34	5.87	25.5				
5750	3.09	4.36	5.98	25.8	3.64	1.493	7.66	68.6
5748	3.54	5.13	5.66	30.6	1.56	1.079	13.16	128.5
5751	3.58	5.12	5.71	30.6	1.65	1.020	13.90	138.6
4644	4.28	6.31	5.22	38.8				
4646	6.58	9.75	4.08	59.2				
4647	8.80	12.68	3.37	79.8				
4689	10.84	15.99	2.10	100.9				
4694	12.38	18.20	1.43	120.4				
4693	14.28	20.20	1.33	141.4				
4695	15.24	21.25	1.24	159.6				
4697	16.22	22.38	1.09	179.8	tumbling			
4698	16.78	22.98	1.05	199.7				
4699	17.22	23.49	0.98	249.5	tumbling			

Figure 27 is a collage of X-ray shadowgraphs that show the penetrating projectile at various times after impact for the 1.25-km/s striking velocity. Figure 28 is the comparable figure for the 1.70-km/s striking velocity. The photographs have been aligned in the figures so that the displacement of the projectile is readily evident. The projectile never penetrated into the confinement block for the full-thickness (20.0-cm thick) glass targets.

Within the resolution of the X-ray shadowgraphs, no cracks can be discerned proceeding from the front or edges of the penetration channels. At the completion of a test, however, the glass is highly fragmented. At early times, the penetration front is hydrodynamic-like; an enlarged view of Test 4624 (V_p = 1.25 km/s) is shown in Fig. 29. The dark solid line that is perpendicular to the projectile denotes the front surface of the glass target. Although the penetration appears hydrodynamic in Figs. 27 and 28, the erosion debris at late times appears much more chaotic and turbulent than it does for metal targets [12].

The position-time data are plotted in Fig. 30 for the two impact velocities. The size of the data points is approximately the uncertainty in the determination of the position. The solid lines in Fig. 30 are fourth-order polynomial least-squares regression fits to the data (the last pair of points for both sets of data were not included in the curve fits). The normalized lengths of the projectiles as a function of time are shown in Fig. 31. The solid symbols represent the *in situ* measurements, and the open symbols denote the experiments where L_R' was measured after exiting the target (Fig. 26). Also in the figure, to the right and beyond 325 μs and denoted by the open symbols with a dot at the center, are the normalized residual lengths L_R^*/D of projectiles recovered in the impact tank (from Tables 6 and 7). These data agree well with the measured L_R'.

Examining the data (Figs. 30 and 31), it is observed that after approximately 130 μs for V_p = 1.25 km/s, and after 160 μs for V_p = 1.70 km/s, there appears to be little or no further erosion of the projectile, and the projectile continues penetration in a rigid-body mode. The flash X-ray pictures of tests 4648, 4649, and 4643 (V_p = 1.25 km/s, Table 8 and Fig. 27) were taken at late times and show a tumbling, rigid-body penetration of the residual rod. Likewise, Tests 4697 and 4699 (V_p = 1.70 km/s, Table 9 and Fig. 28) indicate a tumbling-like behavior. For neither impact velocity, however, did any of the projectiles penetrate to the steel backup plate.

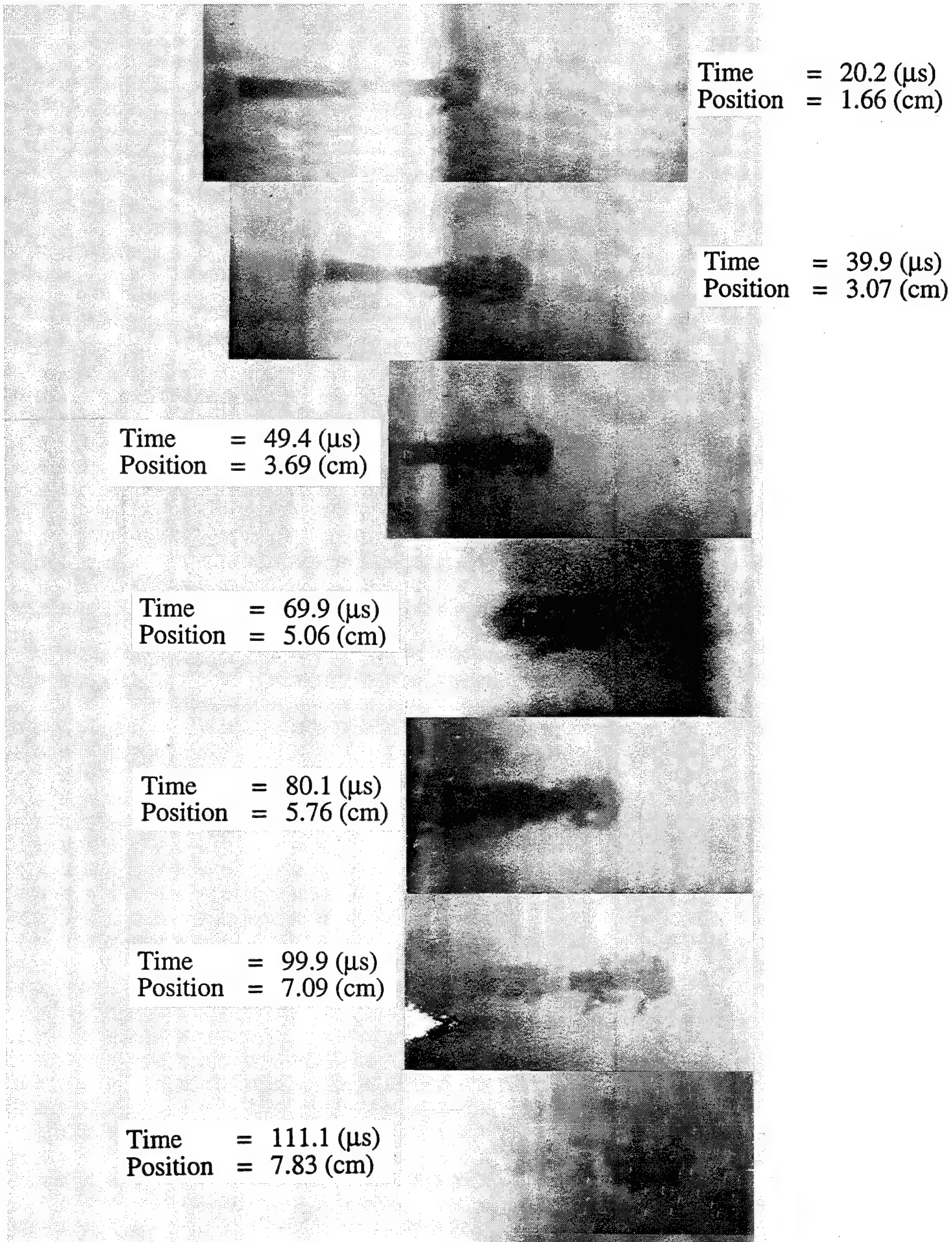

Figure 27. Flash X-rays of tungsten-alloy projectile penetrating glass targets (V_p = 1.25 km/s)

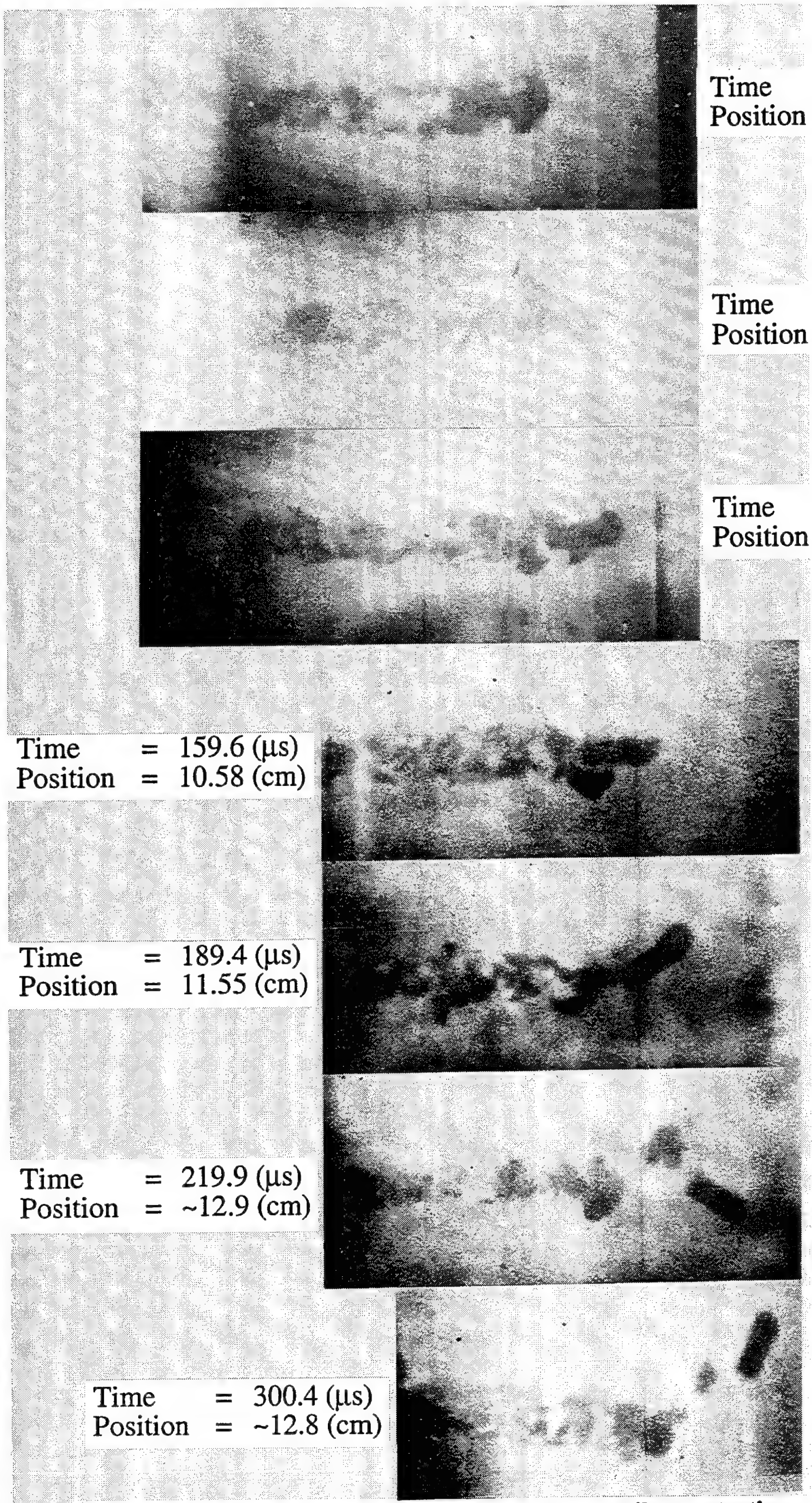

Figure 27. Flash X-rays of tungsten-alloy projectile penetrating glass targets (V_p = 1.25 km/s) (Cont'd)

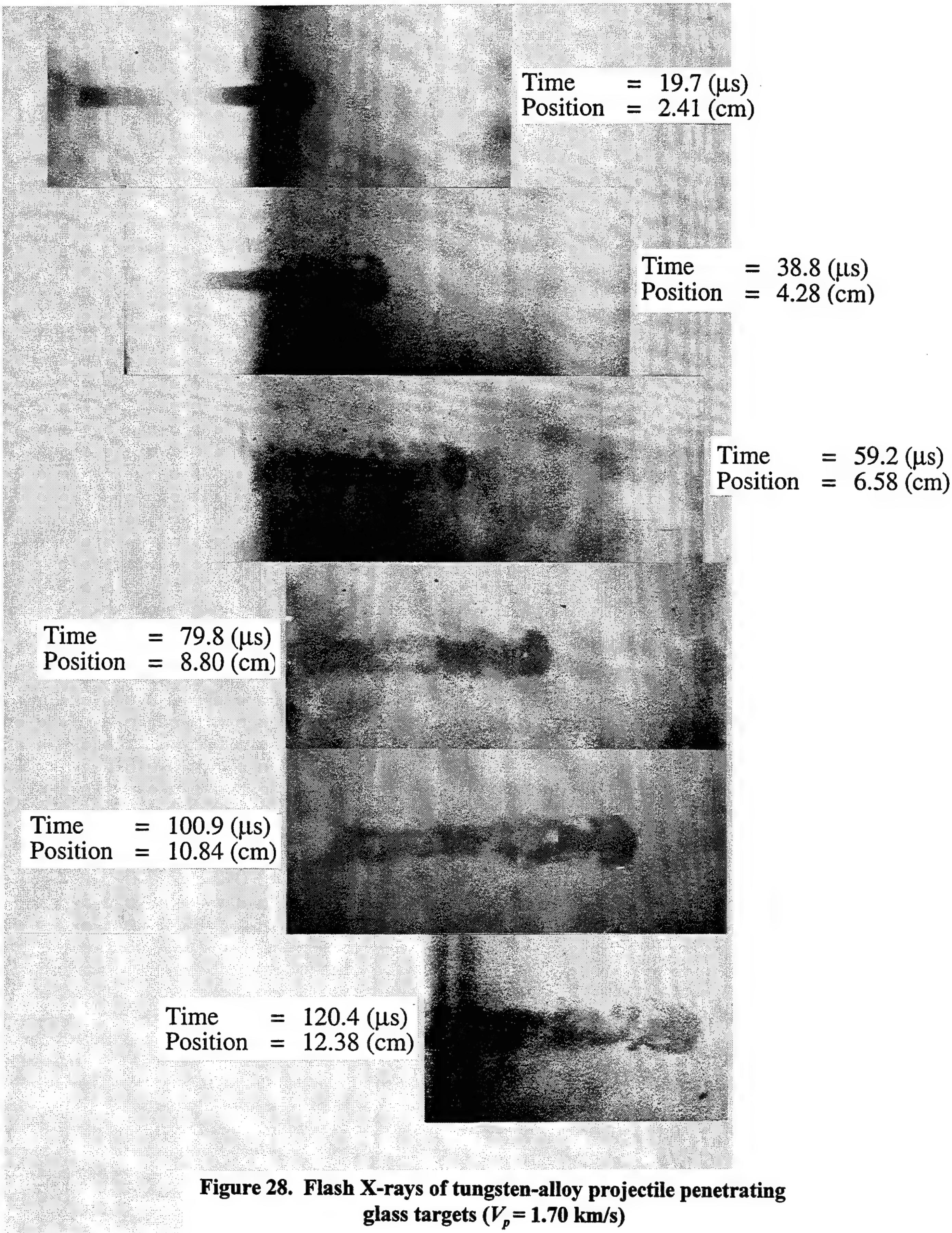

Figure 28. Flash X-rays of tungsten-alloy projectile penetrating glass targets (V_p = 1.70 km/s)

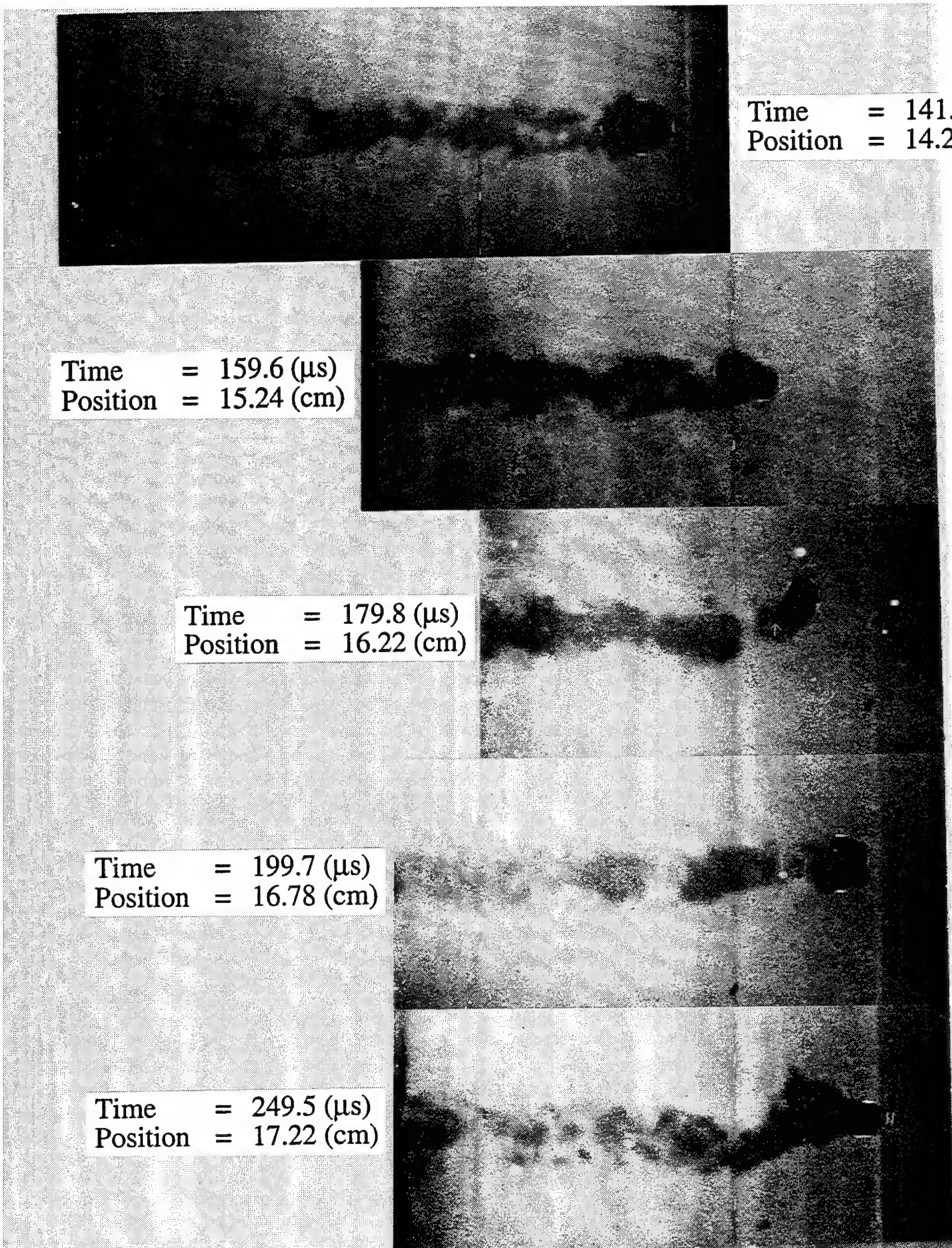

Figure 28. Flash X-rays of tungsten-alloy projectile penetrating glass targets (V_p = 1.70 km/s) (Cont'd)

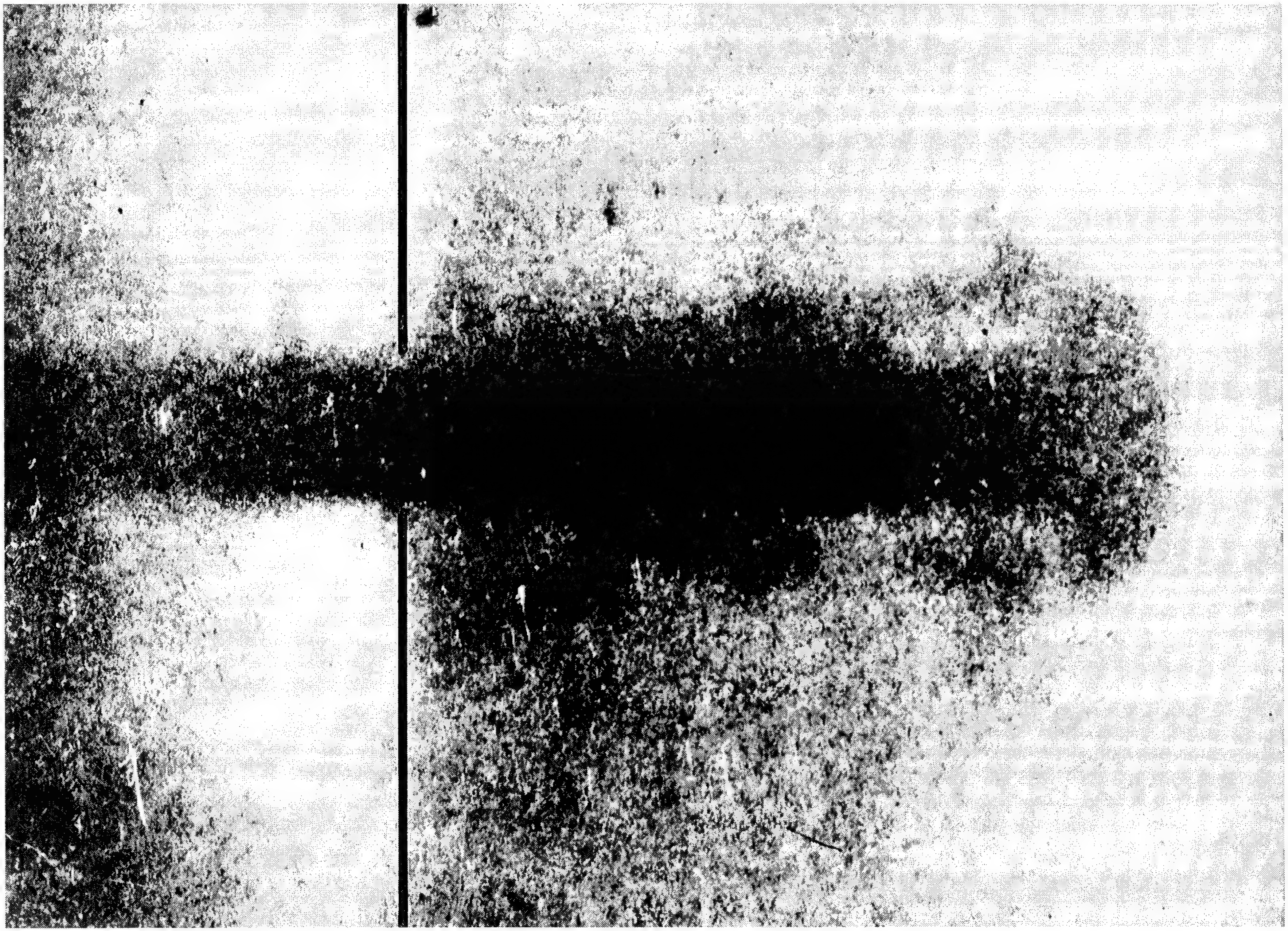

Figure 29. Enlarged photograph of Test 4624 (V_P = 1.25 km/s, t = 49.4 µs, S_K = 3.69 cm)

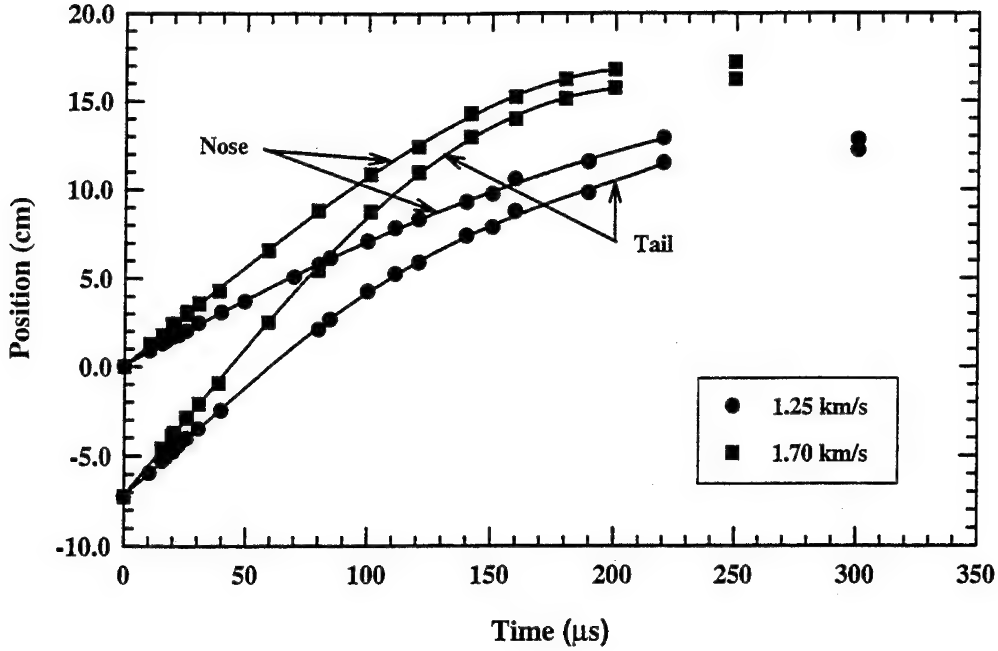

Figure 30. Nose and tail positions versus time

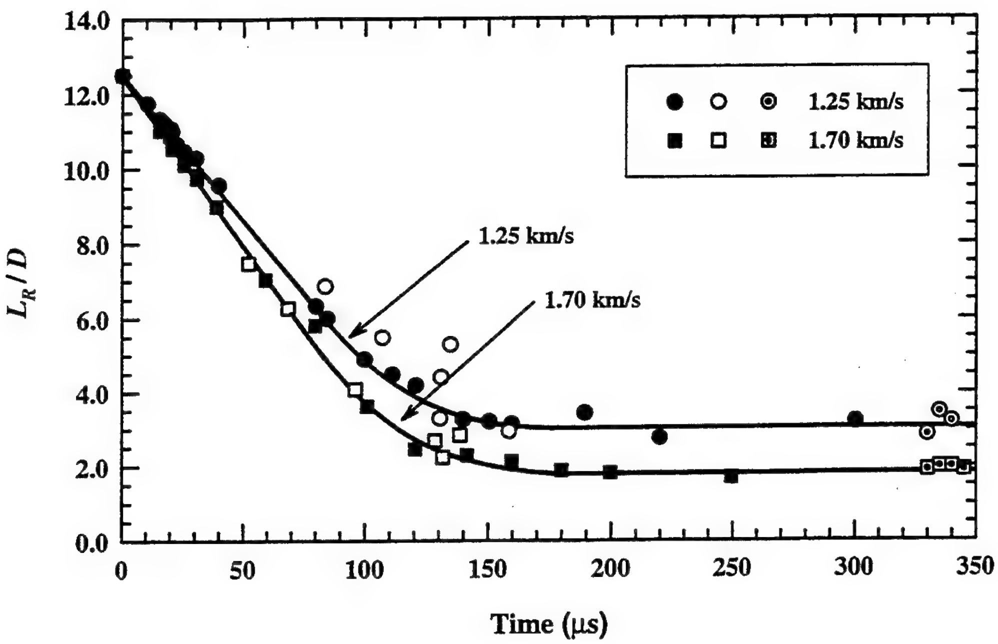

Figure 31. Normalized projectile length versus time: Filled symbols represent *in situ* measurements (Fig. 24); open symbols represent measurements made using the experimental arrangement in Fig. 26; symbols with centered dots represent rods recovered from impact tank

The polynomial curve fits in Fig. 30 were differentiated with respect to time to obtain an estimate of the penetration (nose) and tail velocities.[6] These are plotted in Figs. 32 and 33 for the lower and higher impact cases, respectively. The penetration and tail velocities approach each other in Figs. 32 and 33, signifying rigid-body penetration. However, the derivative of the polynomial fits are less accurate than the original curve fits, and at "late" times, the nose and tail velocities begin to diverge slightly in Fig. 32, and cross each other in Fig. 33; this behavior is simply the manifestation of the inaccuracy of the derivatives at the later times. The open symbols denote the velocities measured by the modified experiment shown in Fig. 26. Since most of the projectile is moving with the velocity of the tail [53], these experimental data lay close to the tail velocity. The velocities in Figs. 32 and 33 are replotted in Figs. 34 and 35 against the penetration depth. The penetration depth is calculated from the penetration-time polynomial expressions. The penetration depth for the experimental data, by definition, is S_K'. (There is no new information in Figs. 34-35; rather, they represent an alternate way of plotting the data.)

4.3 Numerical Simulations

The nonlinear, large deformation Eulerian wavecode CTH [54], using the 2-D cylindrically symmetric option, was used for the numerical simulations. CTH uses a van Leer algorithm for second-order accurate advection that has been generalized to account for a nonuniform and finite grid, and multiple materials; CTH has an advanced material interface algorithm for the treatment of mixed cells. Also, CTH has been modified to allow the flow stress to be a function of strain, strain rate, and temperature [55-56]. Square zoning, with 10 zones resolving the projectile radius, was used for the interaction region.

The Johnson-Cook model [42], with parameters for a tungsten alloy, was used for the projectile. The Johnson-Cook parameters for the tungsten alloy (7% Ni and 3% Fe) were obtained for a material with a density of 17.0 g/cm^3. Although the D17.6 alloy used in the experiments is different from that for which the constitutive constants were obtained, small changes in projectile

[6] An average of a third-order and fourth-order fit to the position-time data was used to obtain the tail velocity for $V_p = 1.25$ km/s.

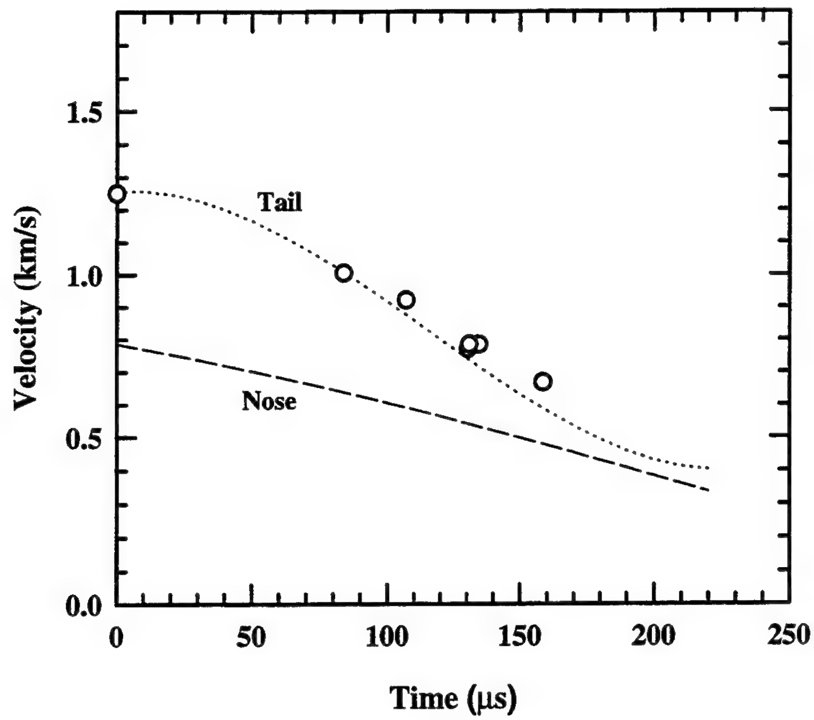

Figure 32. Penetration and tail velocities calculated from Fig. 30, $V_p = 1.25$ km/s; open symbols represent measurements made using the experimental arrangement in Fig. 26

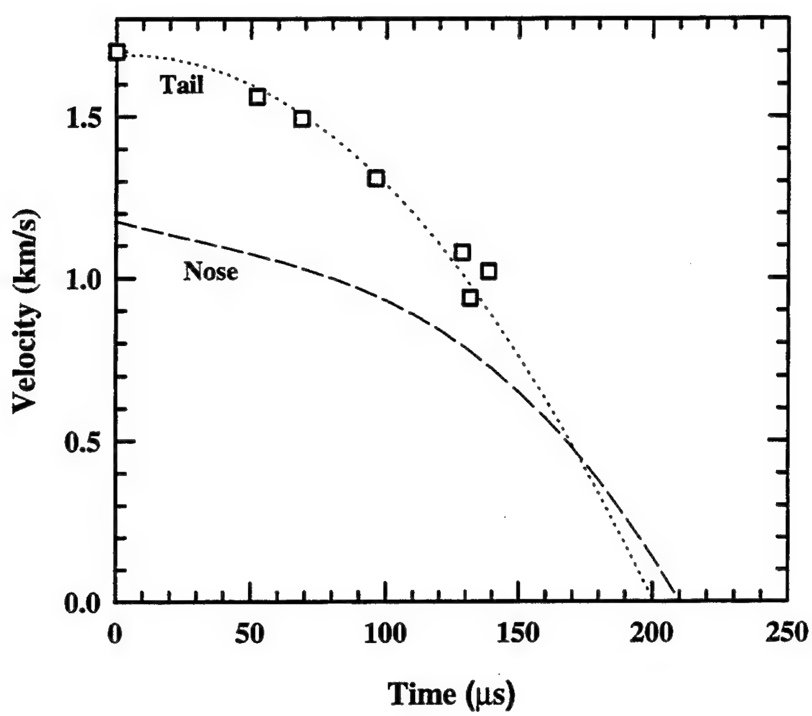

Figure 33. Penetration and tail velocities calculated from Fig. 30, $V_p = 1.70$ km/s; open symbols represent measurements made using the experimental arrangement in Fig. 26

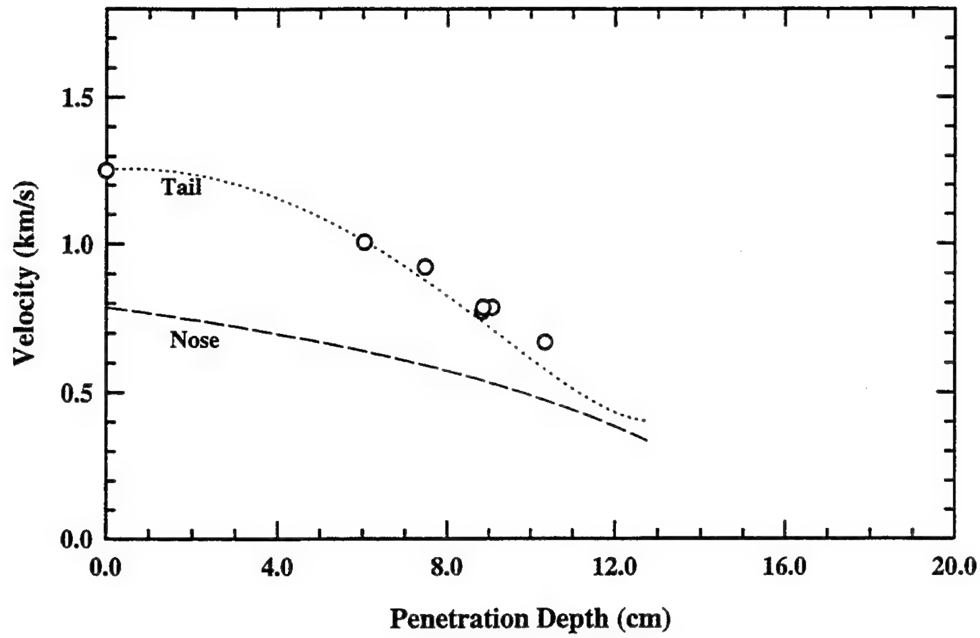

Figure 34. Penetration and tail velocities calculated from Fig. 30, $V_p = 1.25$ km/s; open symbols represent measurements made using the experimental arrangement in Fig. 26

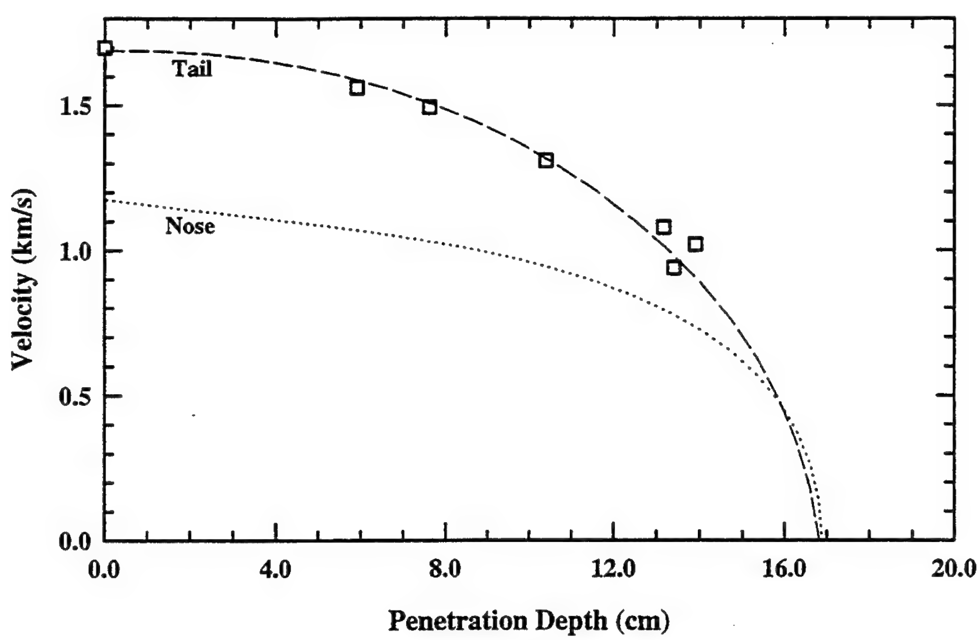

Figure 35. Penetration and tail velocities calculated from Fig. 30, $V_p = 1.70$ km/s; open symbols represent measurements made using the experimental arrangement in Fig. 26

properties have little effect on penetration [51]. Therefore, we used the Johnson-Cook parameters for the numerical simulations, but with a density of 17.6 g/cm[7].

The steel strength was modeled by multiplying the published yield and hardening coefficients for 4340 steel by 1.5 to represent the strength given by Hohler and Stilp (however, the steel does not play a significant role in these calculations since it is being used as a backing to the glass and the projectile does not penetrate into the steel). Constitutive constants for the tungsten and steel are given in Table 10. The Mie-Grüneisen equation of state was used to model the thermodynamic response of all three materials; the equation of state constants are given in Table 11.

Three different constitutive models for the glass were examined. First, calculations were performed with an elastic-perfectly plastic constitutive model for the glass. The flow stress was 1.0 GPa, based on calculations with a one-dimensional analytic model [57]. The depths of penetration versus time according to CTH (the solid line), the Walker-Anderson analytic model (dot-dash line), and the experimental data (open circles) are shown for the impact velocities 1.25 and 1.70 km/s in Figs. 36 and 37, respectively. It is seen that the elastic-perfectly plastic constitutive model works well for early-time penetration. However, the penetrator comes to rest too soon for both the analytical and numerical models. In the experiments, there is evidence of penetration into damaged material, and in particular, there is rigid-body penetration into failed glass. Using an elastic-plastic constitutive response for the target maintains target material integrity, and thus, this constitutive model results in rapid deceleration of the residual projectile at the late times.

At the opposite extreme of material modeling is to assume that the projectile penetrates failed material. Calculations were conducted using a modified Mohr-Coulomb[7] law for the flow stress of the glass:

$$Y = Y_o + \beta P \ . \tag{8}$$

This form treats the glass as completely failed material; it has been used in several constitutive models for failed Pyrex glass and ceramic [58-60, 37-38] (also see Section 3.2). Equation (8) is used

[7]Strictly speaking, Eqn. (8) is not the Mohr-Coulomb law, but is usually referred to as a Drucker-Prager yield surface due to the specific form of pressure dependence and relation to the J_2 and J_3 values. For the purposes here, we use the terminology Mohr-Coulomb to emphasize the pressure dependence.

Table 10. Constitutive Parameters

	Y_o (GPa)	B (GPa)	n (-)	C (-)	m (-)	T_m (K)	G (GPa)	ν (-)	Fract. Stress (GPa)
Tungsten Alloy	1.51	0.177	0.12	0.016	1.00	1748	120	0.30	2.0
Hard Steel	1.189	0.765	0.26	0.014	1.03	1818	77.6	0.29	2.0

$$\sigma_{eq} = (Y_o + B\varepsilon_p^n)(1 + C\ln\dot{\varepsilon}_p)(1 - \bar{T}^m) \qquad \bar{T} = \left(\frac{T - T_o}{T_m - T_o}\right) \qquad T_o = 300°K$$

Table 11. Equation of State Parameters

	ρ (g/cm^3)	c_o (km/s)	k (-)	Γ (-)	c_v (J/gK)
Tungsten Alloy	17.6	3.85	1.44	1.58	0.13
Hard Steel	7.85	4.5	1.49	2.17	0.44
Glass	2.5	4.7	0	1.00	0.43

here directly, without any failure model (for example, a failure model would transition from an intact material model to Eqn. (8) based on some damage condition). With $Y_o = 0$ and $\beta = 1$, reasonable agreement between CTH and the experimental data for an impact velocity of 1.70 km/s is obtained (Fig. 38). Although good agreement is obtained for the higher impact velocity, the model does not do well for the lower impact velocity of 1.25 km/s, where there is too much penetration (Fig. 39). Considerably better agreement is achieved with the 1.25-km/s tests with $Y_o = 0$, $\beta = 2$ as shown in Fig. 40. The values of β producing good results for the two impact velocities are substantially different, and argue that a simple pressure-dependent flow stress will not suffice, and suggest that a more complex constitutive model is required. We note that the apparent success of other researchers, e.g., [58, 37, 38], in using a value of $\beta \approx 1$ may be related to the

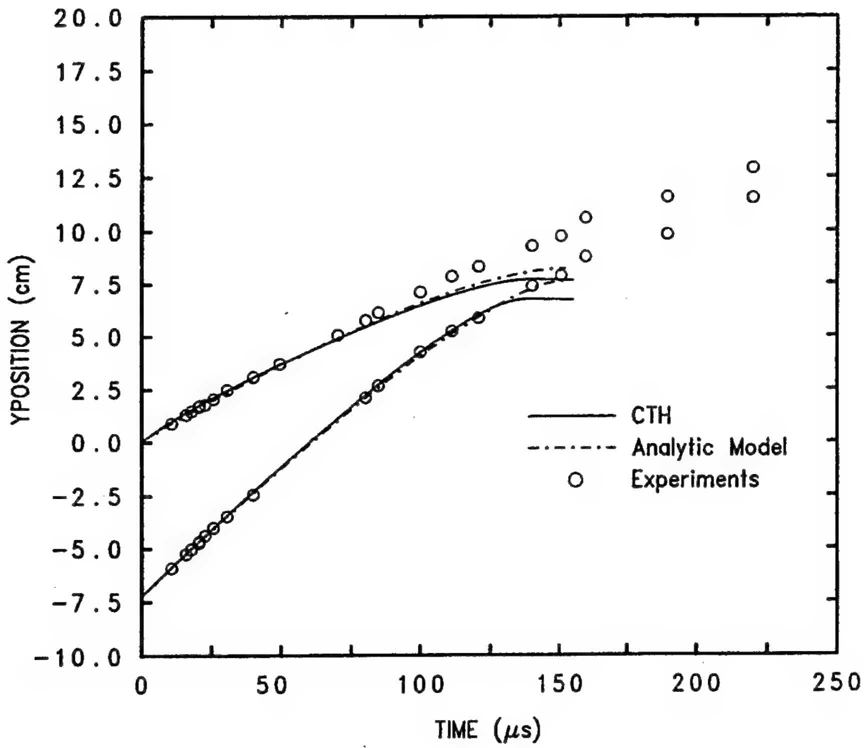

Figure 36. Elastic-perfectly plastic glass model (Y_o = 1.0 GPa): V_p = 1.25 km/s

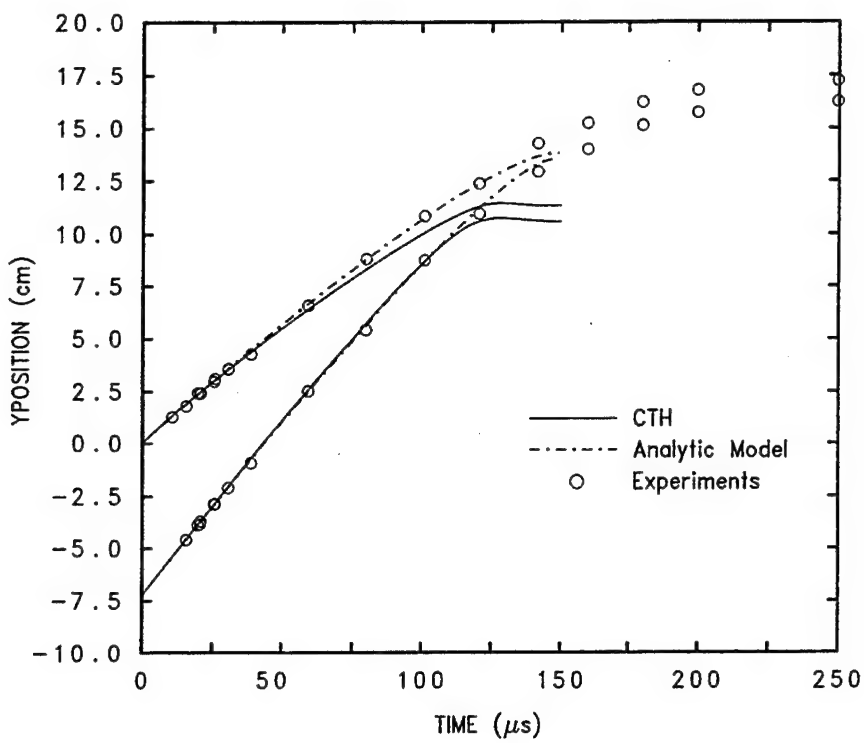

Figure 37. Elastic-perfectly plastic glass model (Y_o = 1.0 GPa): V_p = 1.75 km/s

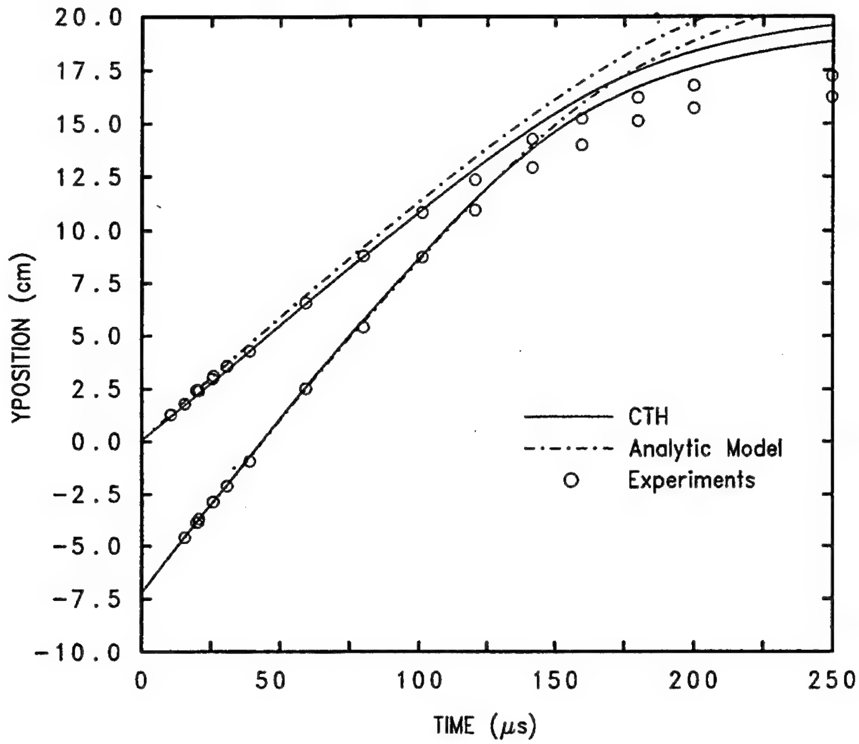

Figure 38. Mohr-Coulomb glass model (Y_o = 0, β = 1.0): V_p = 1.70 km/s

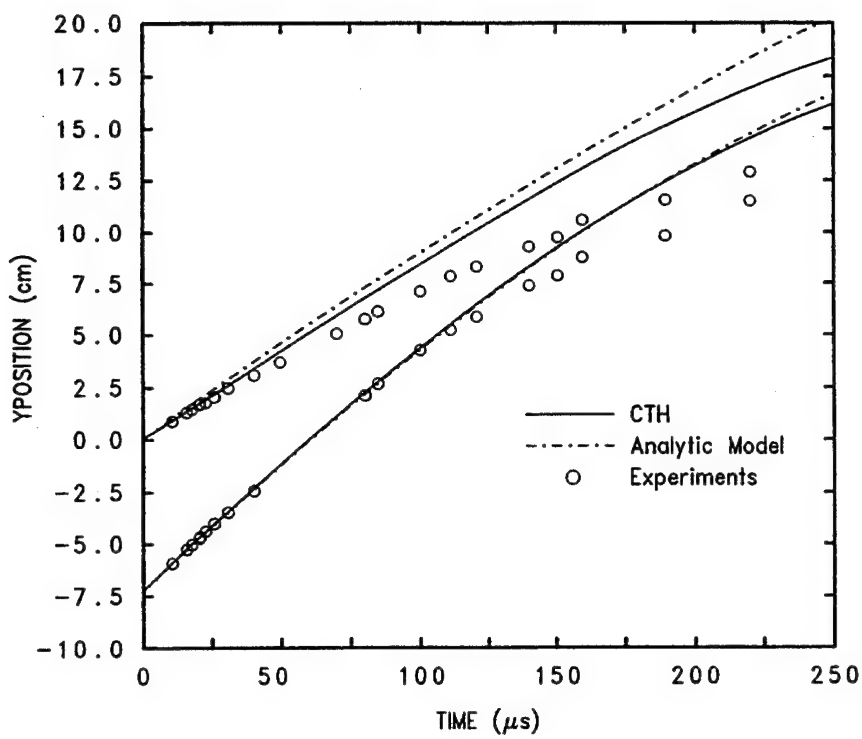

Figure 39. Mohr-Coulomb glass model (Y_o = 0, β = 1.0): V_p = 1.25 km/s

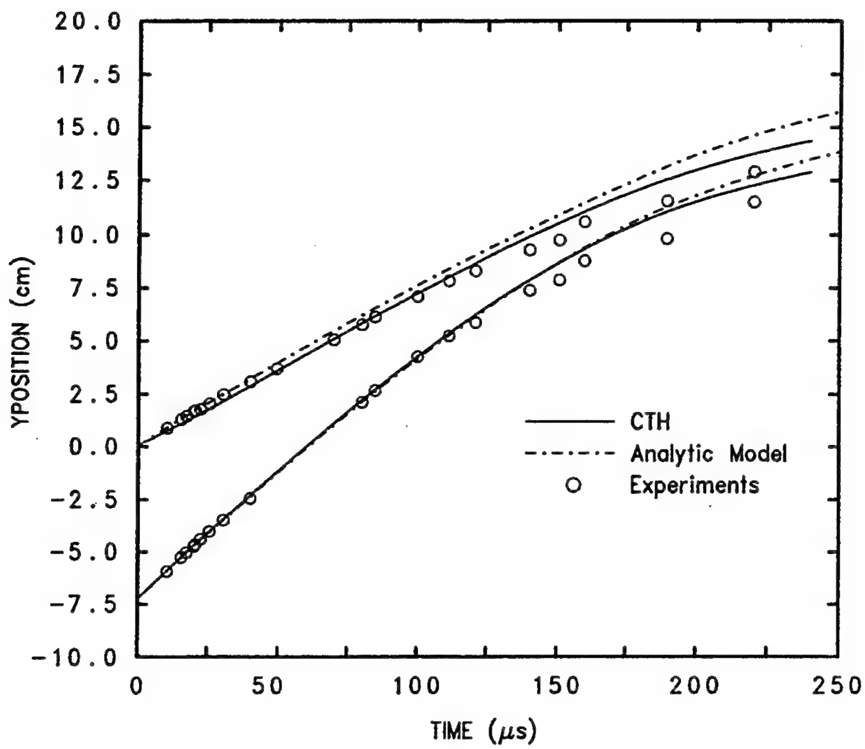

Figure 40. Mohr-Coulomb glass model (Y_o = 0, β = 2): V_p = 1.25 km/s

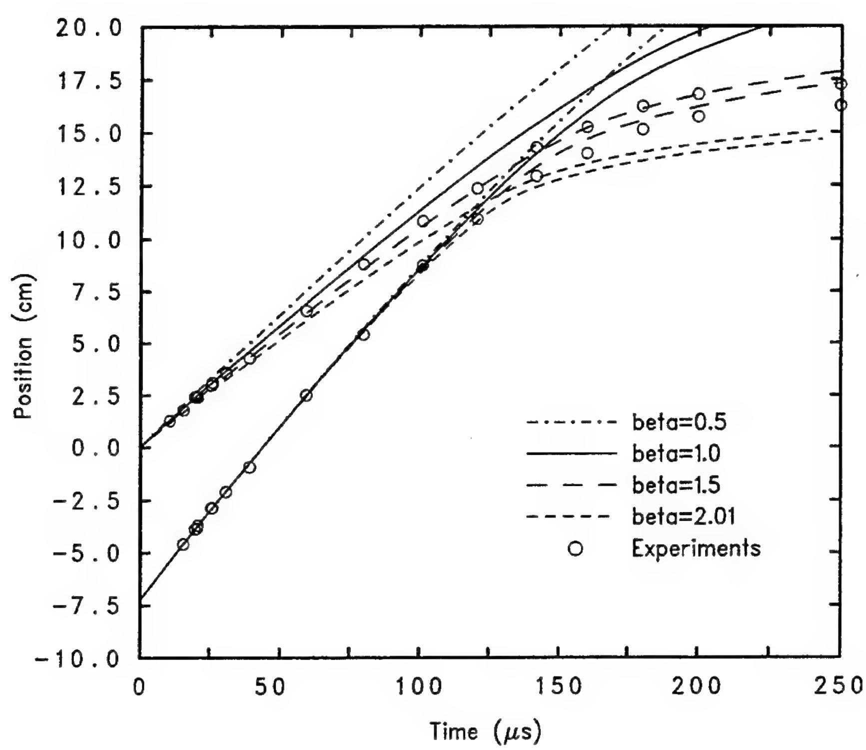

Figure 41. Parametric Study of β in the Mohr-Coulomb glass model: V_p = 1.70 km/s

observation that most experimental data used for comparison purposes has had impact velocities of approximately 1.5-1.6 km/s.

The Walker-Anderson model was modified to allow for the pressure-dependent strength given by Eqn. (8). The results from the modified model are shown as the dot-dash lines on Figs. 38-40, and are similar to those obtained with the CTH calculations ($\beta = 2.01$ was used in the model instead of $\beta = 2$, as the latter leads to a division by zero due to assumptions made in an integration in the model). In both the CTH calculations and the analytic model, the projectile does not come to rest, since the resistance to motion is a function of the velocity squared; the resistance goes to zero as the velocity goes to zero[8].

The effect of variations in β, using the analytical model, are shown in Fig. 41. As β is increased, penetration decreases, as expected. It is seen that $\beta = 2$ is unsuitable for the 1.70-km/s impact case, confirming that earlier observation that the simple pressure-dependent flow stress with constant constitutive parameters is not adequate for matching the experimental data.

As a note, the CTH calculations above were performed with the fracture stress at either 0.1 GPa (1/10th the glass flow stress for the elastic-perfectly plastic calculations) or 2.0 GPa (the standard CTH default). Changing the fracture stress of the glass had little influence on penetration.

A third constitutive model for glass was used. The general form is

$$Y = \min\ (\beta P,\ \bar{Y})\ . \tag{9}$$

Equation (9) is similar to Eqn. (8) except that a maximum value $\bar{Y}$, i.e., a cap, is placed on the flow stress. A number of numerical simulations were conducted to determine an appropriate cap for Eqn. (9). The results of calculations performed for this model with specific values $\beta = 2$, $\bar{Y} = 1.5$ GPa are shown in Figs. 42 and 43. The agreement is reasonable, although for the lower velocity case, the penetration is too great.

[8]The projectile does not come to rest using the "pure" Mohr-Coulomb model, where $Y_o = 0$ in Eqn. (8). Using a small nonzero value for Y_o would terminate penetration. But a small nonzero Y_o is not critical to an evaluation of the overall response using Eqn. (8).

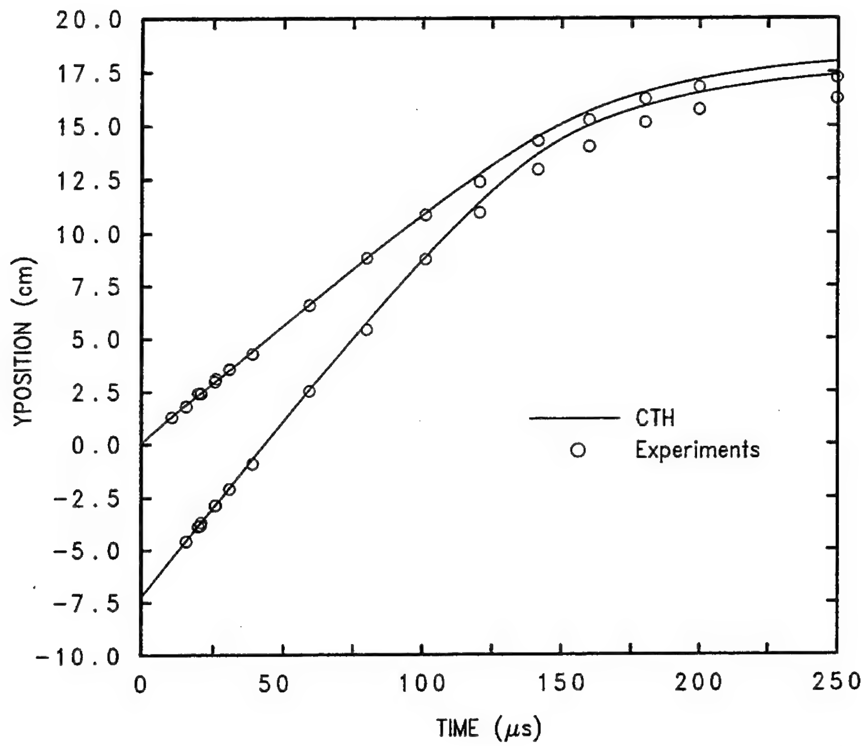

Figure 42. Mohr-Coulomb with cap (1.5 GPa) glass model: V_p = 1.70 km/s

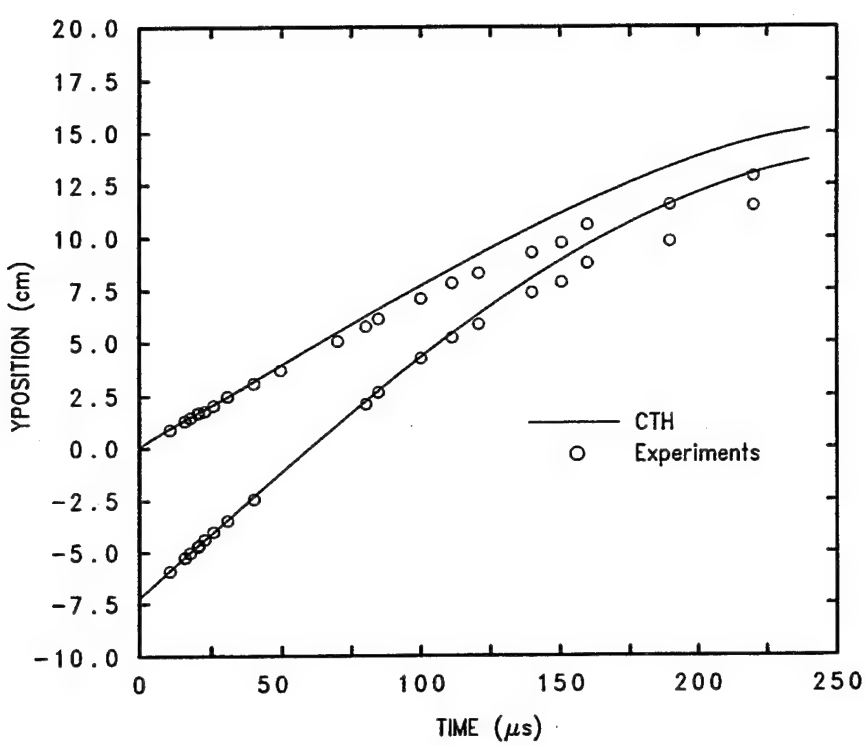

Figure 43. Mohr-Coulomb with cap (1.5 GPa) glass model: V_p = 1.25 km/s

4.4 Discussion

It is instructive to examine the pressure-time histories at the projectile-target interface, and the penetration and tail velocities histories (all along the projectile-target centerline) to gain insights into the constitutive response of the glass. The pressure-time histories for the three constitutive models—elastic-perfectly plastic (EPP); Mohr-Coulomb (MC), i.e., a pressure-dependent flow stress; and Mohr-Coulomb with a cap (MCC)—for the 1.70-km/s simulations are shown in Fig. 44. Except for the initial shock, the penetration pressures are noticeably different for the three glass constitutive models.

The EPP model produces the most steady pressure, which is not to be confused with steady penetration. The penetration and tail velocities for the same three simulations are plotted in Fig. 45. After an initial rapid deceleration of the penetrator nose, there is an approximately constant deceleration of the nose until the final transient deceleration using the EPP model. Although the EPP model results (using a flow stress of 1.0 GPa) matched the experimental position-time data extremely well during early penetration times, the simulation deviated from the experimental results at late times. The EPP constitutive model does not allow for weakening of the glass at late times. As discussed earlier, the experiments indicate that the projectile is penetrating in a rigid-body mode at late times; this suggests that the projectile is penetrating a damaged glass that is substantially weaker than the glass at earlier times.

The MC glass model starts with approximately the same (after-shock) penetration pressure, but then the pressure decreases approximately linearly with time. In contrast to the EPP model results, the early-time penetration velocity for the MC model is approximately 200 m/s less than that for the EPP model.[9] This striking difference is explained by examining the axial stress. The axial stress at the penetrator nose, assuming rigid plastic flow, is given by $-P - 2Y/3$ where P is the pressure and Y is the flow stress (in cylindrical coordinates, the radial and circumferential stresses are equal and given by $-P + Y/3$). The steady-state pressure for the EPP case is approximately 5 GPa, thus, the axial stress is approximately 5.7 GPa. On the other hand, the flow stress at the projectile nose, using $\beta=1$ in Eqn. (8), is initially 5 GPa; therefore, the axial stress is 8.3 GPa for the MC model. This higher axial stress results in a lower penetration velocity. Careful comparisons of

[9]If this velocity differential was maintained for 25 μs, then the difference in penetration depths would be 0.5 cm, approximately the diameter of the circles representing the experimental data in the figures.

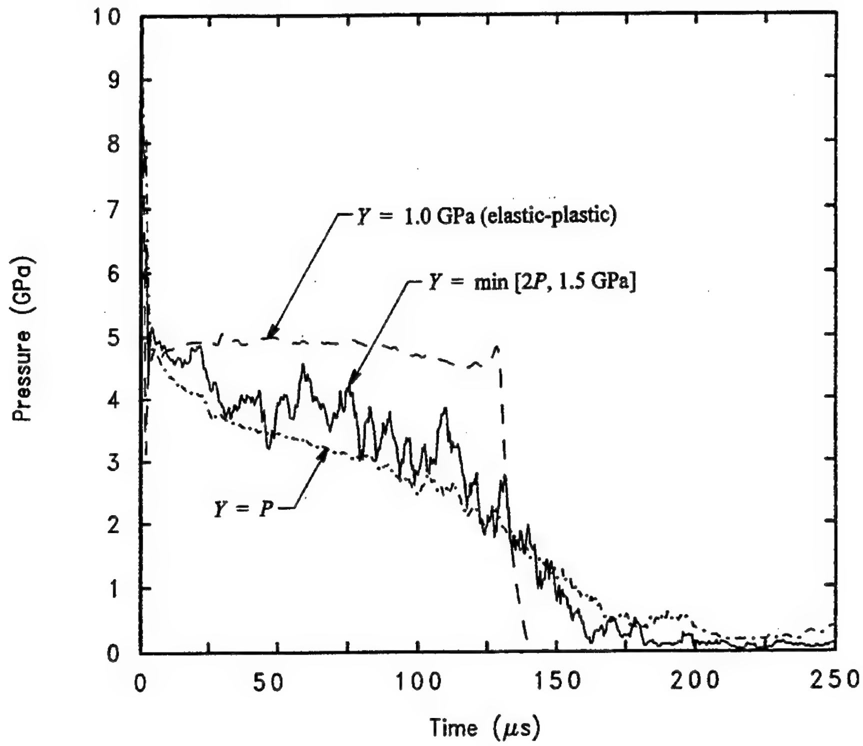

Figure 44. Centerline projectile-target interface pressure for three glass constitutive models (V_p = 1.70 km/s)

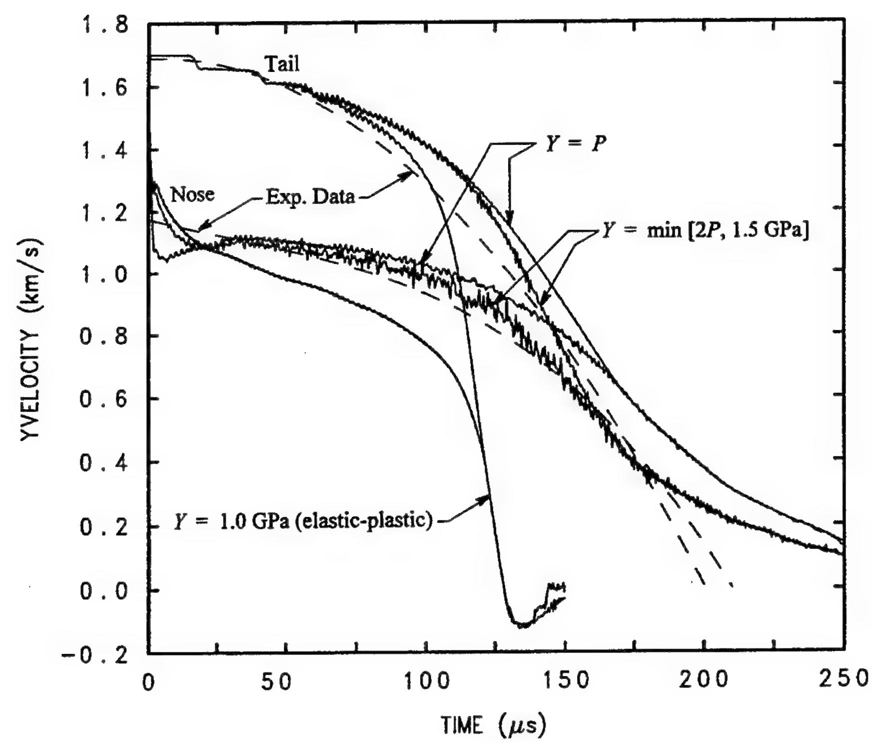

Figure 45. Centerline penetration and tail velocities for three glass constitutive models: V_p = 1.70 km/s

the early-time penetration-time histories of Figs. 37 and 38 show that the MC model initially gives less penetration than the EPP model. But as the penetration velocity decreases, Fig. 45, so does the pressure. The axial stress decreases even faster since it is a function of the pressure and a pressure-dependent flow stress. The net result, overall, is less resistance to penetration, and the projectile, over time, penetrates more deeply.

Target resistance to penetration is an integrated response of the target to deformation flow, and the flow stress of the target is extremely important in determining this flow. The pressure falls off rapidly from the projectile-target interface; consequently, there is less resistance to target flow away from the penetration channel in the MC model compared to the EPP model. As might be expected, the computations show that the penetration channel is substantially wider for the MC model than for the EPP model.

The results from the third constitutive model, MCC, contains features of the EPP and MC models. The very early-time pressures for the MCC model are similar to the results for the other two models[10]. But since the flow stress is capped at 1.5 GPa, the axial stress at early times is approximately 6 GPa. This is not substantially different than the 5.7 GPa for the EPP case. Therefore, the penetration velocity for the MCC model decays similarly to that of the EPP model at early times. However, since the pressure drops off quickly away from the projectile-target interface, the flow stress away from the interface is lower than the cap; therefore, the overall target resistance to flow is less for the MCC model than for the EPP model. Right near the projectile-target interface, the flow stress remains on or near the cap for quite some time. But as the penetration velocity decreases, there comes a point where βP is less than $\bar{Y}$, so the overall resistance to penetration decreases.

The experimental data, as represented by the time derivative of the polynomial fit to the position-time data (see Fig. 33), are shown as the dashed lines in Fig. 45. The experimental velocity-time results can be used to indicate an overall trend; however, very early time and late time results do not have the fidelity of the midtime results due to the sparseness of position-time data at the two time extremes. Comparing the results from the three glass constitutive models to the experimental data reinforces the discussion in the preceding paragraphs. Clearly, the EPP model provides an overestimate of the overall target resistance, resulting in the penetration velocity being

[10]The pressure-time record for the MCC model is extremely "noisy," so a nine-point running average was used to smooth the pressure-time curve. Although not as noisy, the same procedure was also applied to the MC pressure-time results.

too low. The other two models show much better agreement with the experimental penetration velocity. Also encouraging is that the MC model and MCC model permit the projectile to go into a rigid-body penetration mode at approximately 175 μs, in relatively good agreement with the experimental data. As to be expected from the position-time results, the MCC model provides the best agreement with the experimental data. However, the MCC model does not appear to offer quite enough resistance to penetration between approximately 70-125 μs. Also, starting at approximately 90-100 μs, the deceleration of the tail—as indicated by the experimental data—suggests that the projectile is transitioning to rigid-body penetration sooner than that seen in the computations. This observation is reinforced by the small change in total projectile length, Fig. 31, after approximately 120 μs. It is known that numerical simulations do not capture all the correct physics of rigid-body penetration [10], and the process surely is quite complicated with mushrooming and failure of the projectile nose becoming an increasingly stochastic process until further failure is finally inhibited by the strength of the projectile material.

The penetration and tail velocities for the 1.25-km/s impact cases are shown in Fig. 46; again, the experimental data (see Fig. 32) are displayed as the dashed lines. At the lower impact velocity, the differences between the MC and MCC models are almost negligible. The penetration pressures are lower and thus the stress-limiting cap has little influence on the overall results. At this lower impact velocity, the $Y = 2\beta$ does not offer sufficient resistance to penetration since the MC and MCC penetration velocities are larger than those inferred from the position-time experimental data.

4.5 Summary

Matching the final depth of penetration is important but is not the only factor of interest in modeling the penetration process. Modeling the constitutive behavior of metals is sufficiently mature such that calculated penetration-time behavior is in good agreement with time-resolved experimental data [12]. On the other hand, the constitutive treatment of brittle materials, typified here by a soda lime glass, requires more development. Two series of ballistics experiments were conducted to measure penetration depth and projectile tail position in glass targets at different times after impact. One set of experiments was conducted at a nominal impact velocity of 1.25 km/s, while the other was conducted at 1.70 km/s. Numerical simulations of the experiments were

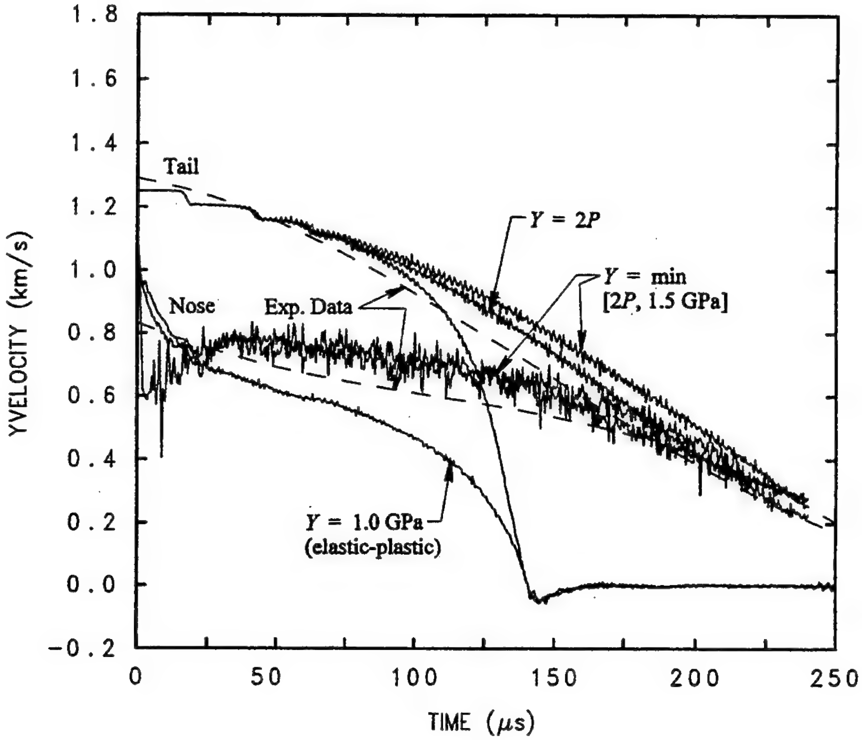

Figure 46. Centerline penetration and tail velocities for three glass constitutive models: V_p = 1.25 km/s

conducted using different constitutive models for the flow response of the glass: elastic-perfectly plastic, a pressure-dependent flow stress, and a pressure-dependent flow stress with a cap.

Earlier analyses [5] indicate that the computational results are dependent on the treatment of mixed cells, i.e., how to "homogenize" the flow stress when there is more than one material within a computational cell. This is particularly true when the process evolves from eroding to rigid-body penetration. Caution must be exercised when constitutive constants are varied to match the experimental data since results can depend on the treatment of mixed cells. In this earlier study [5], 5 zones were used across the radius of the projectile; in the present study, 10 zones were used so as to minimize the influence of mixed cells.

Ultimately, the goal is to model armor ceramics. Glass is used here as a canonical example of a "weak" armor ceramic. The low strength of the glass makes it easier to focus on issues related to strength effects, i.e., the constitutive model. Also, time-resolved data exist, thereby putting constraints on acceptable time histories of penetration. Analysis of the experimental results shows that the effective flow stress of the glass is considerably degraded during penetration. Strength degradation has also been observed for armor ceramics [9, 24], but the glass accentuates this strength

degradation since the penetration process transitions from one of erosion to rigid-body dynamics. It is hoped that proper modeling of penetration into glass will result in an applicable constitutive model for armor ceramics; clearly, the constitutive behavior, model constants, and numerical issues (mixed cells) require further study.

5.0 MEASUREMENT OF CERAMIC DYNAMIC STRENGTH

5.1 Introduction

A number of investigators have demonstrated that confinement can have a major effect on the strength of brittle materials; this has been shown for both rocks and ceramics, e.g., Refs. [61, 62]. In particular, compressive failure strength generally increases significantly with confining pressure, a dependence that can be interpreted to establish empirically the relevant failure criterion (Mohr-Coulomb, etc.) for a given material. It is known that the effect of pressure is manifested physically in the closure of axial microcracks, the coalescence of which ultimately causes compressively loaded specimens to fail. Failed material in powder form also is strengthened by confinement although the strength of this state at a given confining pressure is much reduced versus unfailed ceramic bodies. In this (powder) case, increasing pressure also raises the slope of the stress strain curve; while for solid material, the elastic modulus is essentially pressure-insensitive.

Research on brittle materials in which both confining pressure and strain rate were varied in combination was limited to rocks [61, 63, 64]; however, the superposition of these two environments occurs in the ballistic penetration of ceramics; therefore, a study was initiated to examine these effects in ceramics [65]. The experiments described in Ref. [65] were performed using a split-Hopkinson pressure bar (SHPB) apparatus [66]. For tests with radial confining pressure P_A, a special pressure vessel was utilized. In these experiments, the hydrostatic pressure was first raised to the desired level by pumping fluid into the pressure vessel while a servo-controller matched the axial stress to the pressure. Then the axial load was increased under displacement control at fixed pressure. The value of the strain rate $\dot{\varepsilon}$ was determined by measuring the stress rate $\dot{\sigma}$ and calculating $\dot{\varepsilon}$ using the appropriate value for Young's modulus for each material, i.e., $\dot{\varepsilon} = \dot{\sigma}/E$ [67]. Solid ceramic specimens were loaded by means of tapered alumina platens. Specimens were sealed within thin, heat-shrinkable Teflon tubing, overlapping the small ends of the platens in order to prevent the silicon-based pressure fluid from infiltrating surface pores and causing premature failure. Similarly, powdered compression specimens were produced by tamping the ball milled fines into heat-shrinkable tubing that had been shrunk to fit snugly over alumina platens. These specimens, like the solid ceramics, were 6.4 mm in diameter by 12-13 mm long. Anderson, *et al.* [67], used

numerical simulations to explore, evaluate, and substantiate the assumptions and interpretation of the experimental data.

In the earlier work [65], considerably different behavior was observed for SiC and Pyroceram under confinement. For SiC, Fig. 47, the σ_z versus time curve for $P_A = 0$ is roughly symmetric, suggesting that the specimen failed in a normal brittle fashion. However, with increasing pressure, the curve becomes quite asymmetric, as is especially noticeable for $P_A = 200$ MPa. The specimen did not fracture at 320 MPa confining pressure. On the other hand, the post-failure behavior of Pyroceram, Fig. 48, is more complex than that of SiC. It resembles very much, in fact, the phenomenon observed by Heard and Cline [68] for BeO and AlN subject to compression under confining pressure at strain rates on the order of 5×10^{-5} s^{-1}. In their work, it was hypothesized that the softening-to-hardening trend with rising pressure was caused by a brittle-to-ductile transformation, i.e., pressure above a critical level suppressed fracture and permitted plastic flow via dislocation motion. It is interesting to note that Heard and Cline saw no such pressure-induced plastic flow for Al_2O_3 subject to confinement at pressures as high as 1.25 GPa; i.e., it failed in an apparently brittle fashion at this and lower pressures.

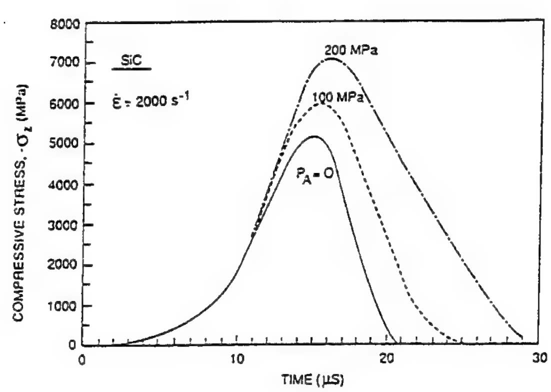

Figure 47. Compressive strength versus time for SiC at various confining pressures

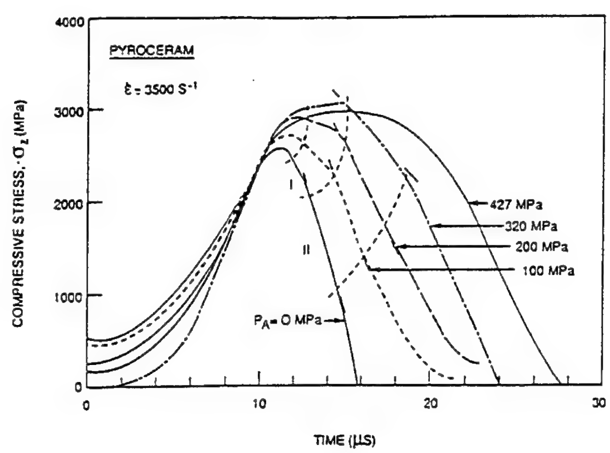

Figure 48. Compressive strength versus time for Pyroceram at various confining pressures

However, there are several limitations to the experimental methodology of the work in Ref. [65]. First, the maximum confining pressure was, in practice, limited to approximately 320 MPa (427 MPa was achieved for only a couple of tests, e.g., Fig. 48). At higher pressures, the seals did not contain the hydraulic fluid. Additionally, there were safety concerns relative to the

high static prestress and the linearity of the SHPB system (small deviations from linearity increased the likelihood of buckling of either the transmitter or receiver bar). To overcome these limitations, a different procedure to provide the confining pressure was needed. Chen and Ravichandran [69] have recently shown that lateral confinement can be applied by shrink fitting a metal sleeve onto the lateral surface of a cylindrical ceramic specimen. Using this approach, they report lateral confinement pressures as high as 200 MPa were developed for aluminum nitride, which was then subjected to moderate dynamic strain rates (500 s^{-1}) using a split-Hopkinson pressure bar. Under these conditions, samples were observed to fail by microfracture coalescence over a loading period of more than 300 μs.

The present effort describes a modification of this approach to achieve higher confining pressures, higher strain rates, and shorter loading periods (about 10 μs). Also, the approach of Chen and Ravichandran leads to an indeterminate stress state within the specimen; the present approach puts the specimen under a state of hydrostatic pressure. It will be shown that the sample does not fail under the latter conditions, and that extensive plastic flow is introduced.

5.2 Theory: The Autofrettaged Device

To achieve higher pressures, a steel confinement ring is shrink fitted around the ceramic specimen. To maintain an elastic response in the confinement ring, the ring is actually composed of two concentric rings, with the outer ring shrink-fitted to the inner. This autofrettaged assembly is then shrink-fitted to the ceramic specimen, producing a compressive stress state in the specimen. During the shrink fitting, the ceramic is compressively loaded in order to achieve a hydrostatic state of stress.

To calculate the amount of axial loading required and determine the subsequent pressure on the ceramic specimen, the elastic equations with an assumed uniform strain in the axial direction were solved. In cylindrical coordinates, assuming no θ dependence, the strains are

$$\epsilon_{rr} = \frac{\partial u_r}{\partial r} \, , \; \epsilon_{\theta\theta} = \frac{u_r}{r} \, , \; \epsilon_{zz} = \frac{\partial u_z}{\partial z} \, , \; \epsilon_{zr} = \frac{1}{2}\left(\frac{\partial u_z}{\partial r} + \frac{\partial u_r}{\partial z}\right) \qquad (10)$$

where u_i represents the various displacements. Assuming that the axial displacement depends only upon z and the radial displacement depends only upon r yields $\epsilon_{zr} = 0$. Given the strains, the stress state is obtained from Hooke's law:

$$\begin{aligned}
\sigma_{rr} &= (\lambda + 2\mu)\frac{\partial u_r}{\partial r} + \lambda\frac{u_r}{r} + \lambda\epsilon_{zz} - 3KA^T \\
\sigma_{\theta\theta} &= \lambda\frac{\partial u_r}{\partial r} + (\lambda + 2\mu)\frac{u_r}{r} + \lambda\epsilon_{zz} - 3KA^T, \quad A^T = \int_{T_{room}}^{T} \alpha(T)\, dT \qquad (11) \\
\sigma_{zz} &= \lambda\frac{\partial u_r}{\partial r} + \lambda\frac{u_r}{r} + (\lambda + 2\mu)\epsilon_{zz} - 3KA^T
\end{aligned}$$

where λ and μ are Lamé constants, and A^T is the thermal expansion term. For the ceramic, the coefficient of thermal expansion α is temperature dependent.

The equilibrium equation in cylindrical coordinates is

$$\frac{\partial \sigma_{rr}}{\partial r} + \frac{1}{r}\left(\sigma_{rr} - \sigma_{\theta\theta}\right) = 0 , \qquad (12)$$

and when combined with Eqn. (11) it becomes

$$\frac{d}{dr}\left(\frac{1}{r}\frac{d}{dr}(r u_r)\right) = 0 . \qquad (13)$$

The general solution, due to Lamé, is:

$$u_r = Ar + \frac{B}{r} . \qquad (14)$$

The resulting strains are

$$\epsilon_{rr} = A - \frac{B}{r^2}, \quad \epsilon_{\theta\theta} = A + \frac{B}{r^2} . \qquad (15)$$

The stresses can now be written in terms of the known strains. The pressure is

$$P = -\frac{1}{3}\sigma_{ii} = -\frac{1}{3}\left[(3\lambda + 2\mu)\left(\frac{\partial u_r}{\partial r} + \frac{u_r}{r} + \epsilon_{zz}\right) - 9KA^T\right] \tag{16}$$
$$= -K\left[2A + \epsilon_{zz} - 3A^T\right].$$

In order to estimate the confining pressure applied to the specimen from elastic considerations, the confinement sleeve cannot be allowed to yield, and to ensure that this is the case, the equivalent stress is compared with the yield stress of the steel confinement material. Therefore, to maintain an elastic condition, the pressure on the specimen is limited by the yield stress of the autofrettaged confining material. The equivalent stress is

$$\sigma_{eq} = \sqrt{3J_2} = \left\{\frac{1}{2}\left[(\sigma_{rr} - \sigma_{zz})^2 + (\sigma_{zz} - \sigma_{\theta\theta})^2 + (\sigma_{\theta\theta} - \sigma_{rr})^2\right]\right\}^{1/2} \tag{17}$$
$$= 2\mu\sqrt{(A - \epsilon_{zz})^2 + 3B^2/r^4}\ .$$

The equivalent stress is examined to see if the yield of the steel containment material is exceeded.

In the actual apparatus, VASCOMAX steel, with a yield strength of approximately 2.4 GPa, was used in fabricating the sleeve. For the specific geometry described later, the design is such that the maximum confining stress is actually limited by the temperature to which the autofrettaged ring can be raised, since for a wide range of temperatures the response is elastic.

The geometry is comprised of three regions, the inner ceramic specimen of radius a and the two concentric steel rings for containment of outer radii b and c. These regions will be indicated by the subscripts I, II, and III, respectively. In the inner region $B = 0$, since the solution must be well behaved at $r = 0$. A desired property in the inner region is that the stress state has no shear components, i.e., the load be purely hydrostatic, ($\sigma_{rr} = \sigma_{\theta\theta} = \sigma_{zz}$). This requires

$$A_I = \epsilon_{zz}\ . \tag{18}$$

We assume that regions *II* and *III* are made of the same material so that, for example, $\lambda_{II} = \lambda_{III}$. The boundary conditions between the regions are defined below.

BC1: Matching normal stresses (σ_{rr}) at $r = a$

$$3K_I(A_I - A_I^T) = 2(\lambda_{II} + \mu_{II})A_{II} - 2\mu_{II}\frac{B_{II}}{a^2} + \lambda_{II}(A_I + (\epsilon_{zz})_0) - 3K_{II}A_{II}^T \quad (19)$$

BC2: Matching displacements at $r = a$

$$A_I a = A_{II} a + \frac{B_{II}}{a} \quad (20)$$

BC3: Matching normal stresses at $r = b$

$$2(A_{II} + \mu_{II})A_{II} - 2\mu_{II}\frac{B_{II}}{b^2} - 3K_{II}A_{II}^T = 2(\lambda_{II} + \mu_{II})A_{III} - 2\mu_{II}\frac{B_{III}}{b^2} - 3K_{II}A_{III}^T \quad (21)$$

BC4: Matching displacements at $r = b$

$$A_{II}b + \frac{B_{II}}{b} = A_{III}b + \frac{B_{III}}{b} \quad (22)$$

BC5: Zero normal stress at outer surface

$$2(\lambda_{II} + \mu_{II})A_{III} - 2\mu_{II}\frac{B_{III}}{c^2} + \lambda_{II}(A_I + (\epsilon_{zz})_o) - 3K_{II}A_{III}^T = 0 \quad (23)$$

These five boundary conditions provide a linear system of five equations in the five unknowns A_I, A_{II}, B_{II}, A_{III}, and B_{III}.

The above system is first solved with no specimen to determine the inner radius of the autofrettaged device upon heating to a given temperature. This provides a radius for the test specimen. To load the specimen, the autofrettaged steel confinement ring is heated and the room

temperature specimen is placed in the inner cavity. The specimen is axially loaded in compression while cooling occurs.

In the analytical solution, it is assumed there is no axial slip between the ceramic specimen and the inner steel confinement ring once the room temperature specimen is inserted into the heated autofrettaged device. Thus, the axial displacement and strain (ϵ_{zz}) are the same for all regions. When the computation without the specimen is performed, an axial strain for just the autofrettaged ring is determined. This axial strain $(\epsilon_{zz})_0$ is used as an initial offset in the solution for the complete assembly. Use of this strain provides for the condition of no pressure on the specimen when it is initially inserted into the heated autofrettaged ring. After insertion, and as the temperature decreases, the axial strain is adjusted (through axial loading of the specimen) to maintain a hydrostatic state of stress within the sample.[11] This then leads to a final pressure within the specimen at room temperature. It also allows evaluation of the equivalent stress at the inner surfaces of the steel rings, where it is greatest. For the specific geometry discussed below, Fig. 49 shows the values of the pressure in the room temperature specimen and the maximum equivalent plastic stresses in each of the steel rings versus the temperature of the steel. It is seen that the stress state in the rings is well below yield.

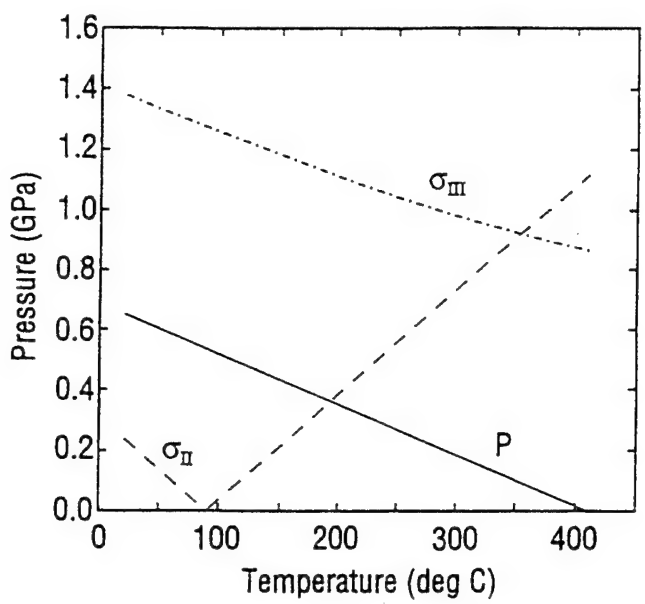

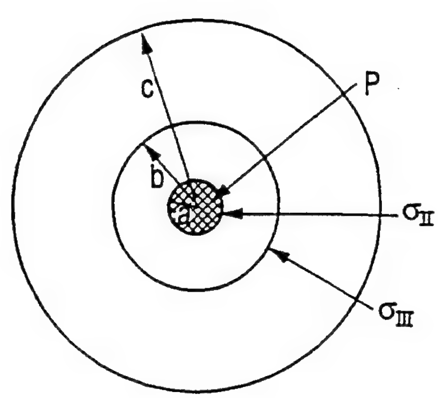

Figure 49. Pressure and equivalent plastic strain as a function of temperature

[11] Note that what is done to produce Fig. 49 is different from what is actually done in the test. For the former, gradual loading is applied during cooling, while in the latter, the full load is applied initially and held while the specimen cools.

5.3 Experimental Assembly

The inner and outer rings of the sleeve are shown in Figs. 50a and 50b, respectively, and the assembled device is shown in Fig. 50c. The autofrettaged ring was constructed with the inner steel ring having an inner diameter of 0.6213 cm and an outer diameter of 1.2621 cm, and the outer steel ring having an inner diameter of 1.2565 cm and an outer diameter of 3.1687 cm. With this geometry, the outer steel ring's inner diameter at 413°C equals the inner ring's outer diameter at 21°C (room temperature). (The actual temperature used in assembly was of course higher to allow clearance.) This corresponds to a temperature offset of 392°C used in the analytic solution. The radius ratios of roughly $b = 2a$ and $c = 5a$ were arrived at by examining the analytic solution; c is large enough that the outer ring nearly appears to have infinite extent (which leads to higher pressures). After cooling, the autofrettaged ring had an inner diameter of 0.6200 cm and an outer diameter of 3.1707 cm. These values agreed very well with the theoretical predictions of an inner diameter of 0.6187 cm and an outer diameter of 3.1702 cm. The inner diameter was subsequently machined to 0.6304 cm. Proper alignment is critical during the assembly due to the tight tolerances;

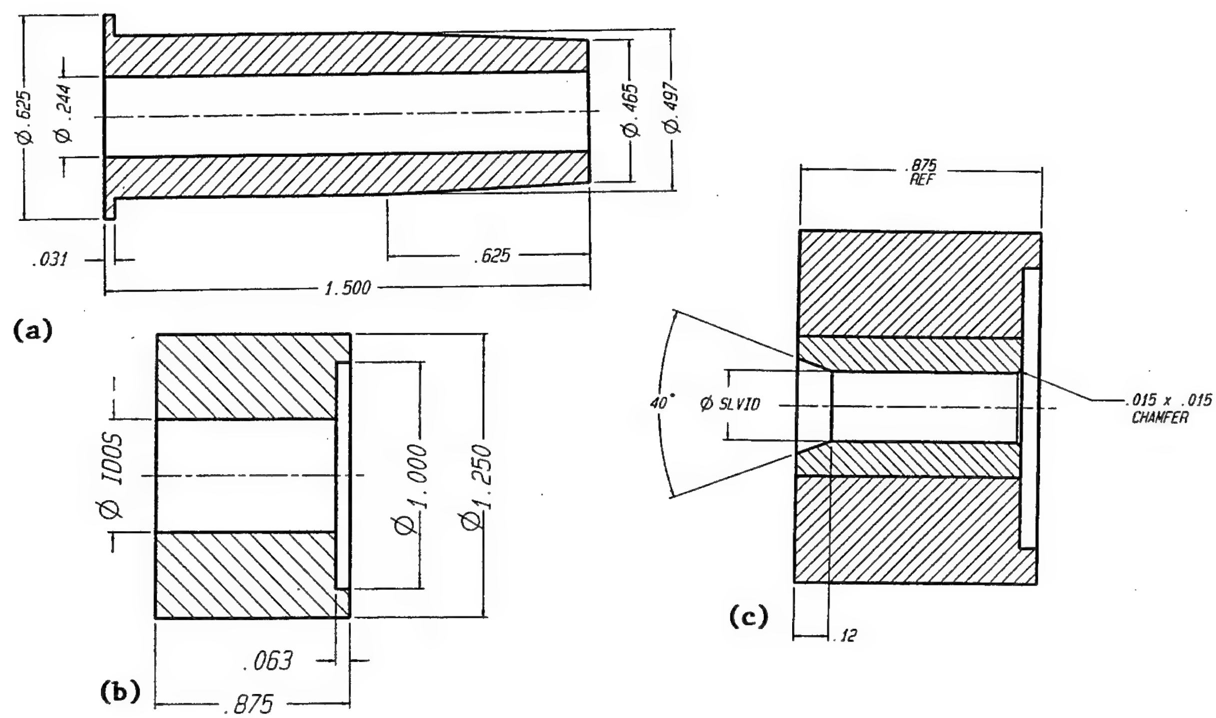

Figure 50. (a) Inner confinement ring of autofrettaged device, (b) Outer confinement ring of autofrettaged device, and (c) Assembled autofrettaged device

if the two rings touch before the insertion is complete, heat transfers from one ring to the other, causing the inner ring to expand, and the outer ring to contract, and the assembly process halts as the device seizes. The initial and the final dimensions of the sleeve assembly are also given in the figure (in English units).

Dimensions of the test specimen are tailored to provide the appropriate fit with the sleeve. Assuming a "perfect fit" for the specimen at a sleeve temperature of 410°C, the specimen diameter is 0.6332 cm. The hydrostatic confining pressure after completion of the test fixture assembly is 650 MPa. Small changes in the magnitude of interference have a pronounced effect on the amplitude of the generated confining pressure. A 0.000254-cm change will increase or decrease the confining pressure by roughly 60 MPa. Using higher temperatures for the "perfect fit" (and increasing the specimen diameter accordingly) produces higher pressures: for example, 538°C gives 930 MPa.

To perform the confining pressurization procedure and the subsequent high strain rate loading of the specimen, an experimental apparatus, as shown in Figure 51, was designed and fabricated. The components of the apparatus are shown in Fig. 52 prior to assembly, whereas Fig. 51 is a schematic of the assembled fixture. The purpose of the apparatus is threefold:

1) support the specimen and the "confining chamber" components, comprised of the confining sleeve and the loading anvils, during the autofrettaging procedure;

2) provide the necessary alignment and guidance of the components during the autofrettaging assembly process; and

3) act as a reaction frame for the application and maintenance of the axial component of the hydrostatic pressure.

Initially, the specimen and the upper loading anvil are held approximately 2.05 cm above the confining sleeve by attaching them to the load transmitter bar positioned internally to the hydraulic actuator. A water cooled brass shield, not shown in the figure, is inserted between the specimen/upper anvil assembly and the sleeve to prevent heating of the specimen.

The compact, ring type, high-pressure hydraulic actuator of the apparatus, shown in Fig. 52d, is mounted on the sliding and rotatable support/locking ring. To assure proper alignment during the auto-frettaging procedure, the support/locking ring is piloted by a guide ring assembly, not shown

in Fig. 51 but which is shown in Fig. 52d. The position of the guide ring assembly is adjustable on the reaction frame. Initial alignment of the guide assembly, relative to the confining sleeve, is accomplished with special alignment tools (see Fig. 52d), and without the presence of the specimen and the upper loading anvil. Precision alignment of the system is critical due to the close tolerancing of the specimen and the confining sleeve and the requirement for rapid insertion of the specimen into the confining sleeve once the target temperature of the confining sleeve is achieved.

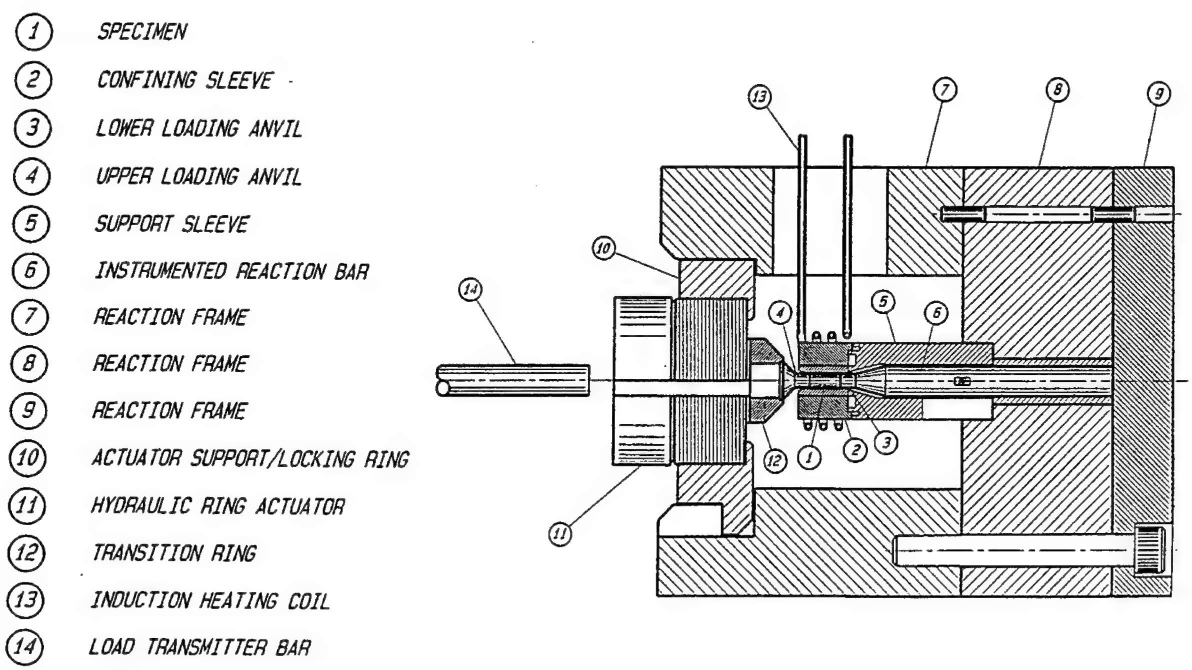

Figure 51. Experimental apparatus

During the autofrettaging procedure the confining sleeve is held in its proper position by a brass support sleeve, while the lower loading anvil is supported by the instrumented reaction bar. In addition to its supporting function, the support sleeve serves as a shield for the reaction bar, protecting the bar from direct heating by the induction coil. To provide further protection for the strain gages, the reaction bar is also equipped with two water cooled pads, not shown in the figure, to mitigate the effect of the heat conducted into the bar from the lower loading anvil during the autofrettaging procedure.

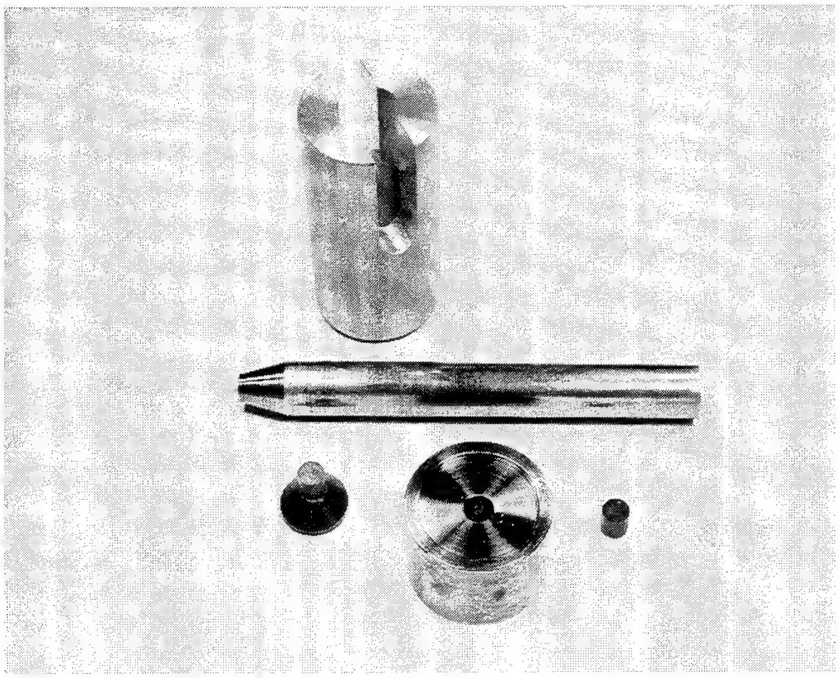

Figure 52a. Device Components: Items 4, 2, 3 5 and 6 (see Fig. 51)

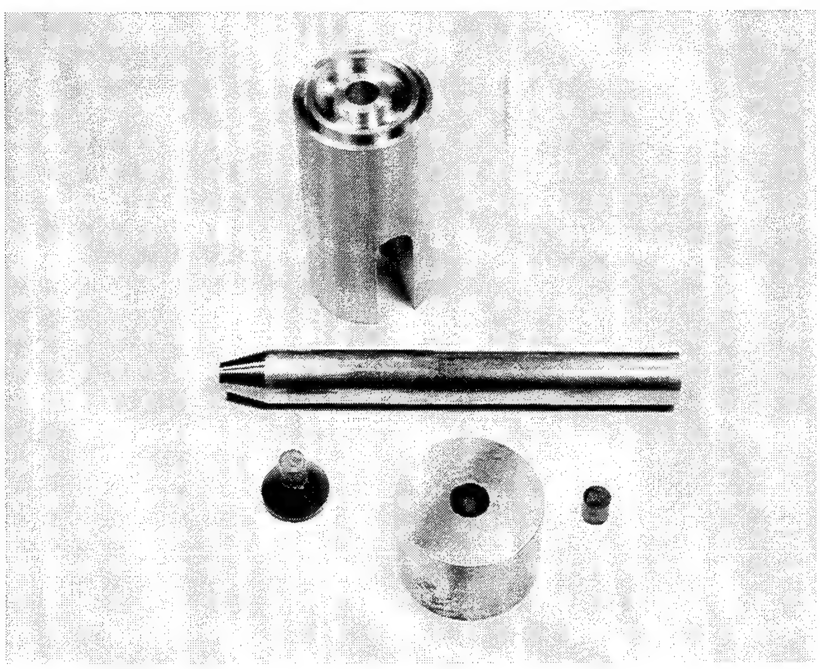

Figure 52b. Device Components: Same as Fig. 52a but items 2 and 5 turned over

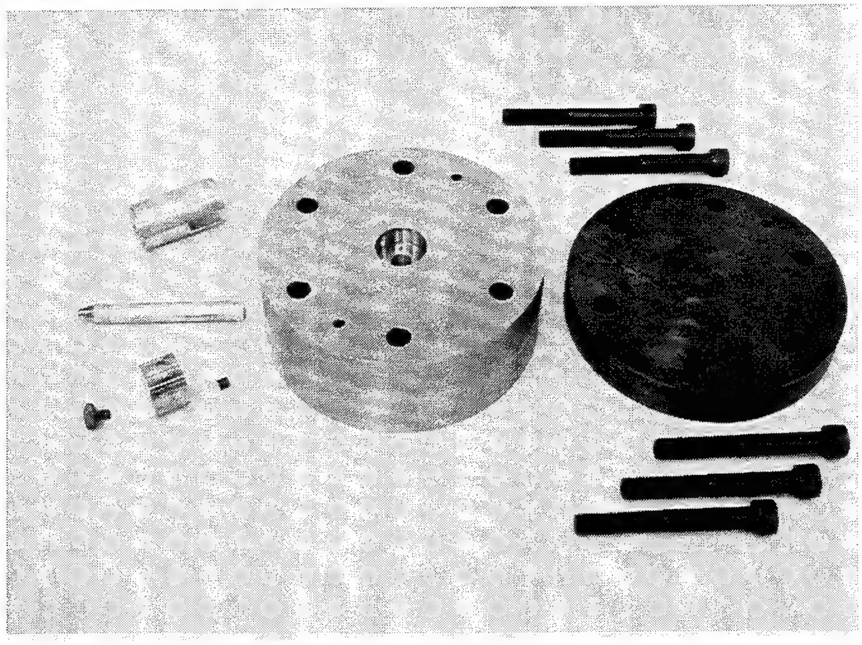

Figure 52c. Device Components: Items 8 and 9 (see Fig. 51) along with the components shown in Fig. 52a

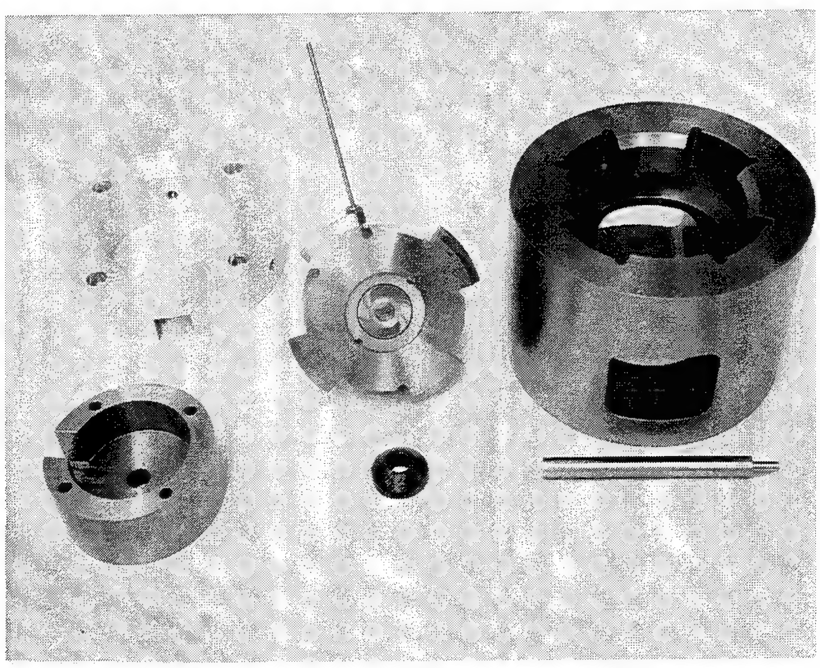

Figure 52d. Device Components: Items 8, 10, 11, and 12 (see Fig. 51). Items 10 and 11 (compact, ring type, high-pressure hydraulic actuator) are combined in the photograph. The two items in the left part of the photograph (not shown in Fig. 51) are alignment rings that go around the hydraulic actuator. The long cylindrical bar in front of piece 8 is an alignment tool for precise alignment of the hydraulic actuator.

Once proper alignment is established, the autofrettaging procedure is performed in a servo-controlled, hydraulic, MTS test system under closed-loop load control, where the output signal from the strain gage on the reaction bar is used as the feedback. The confining sleeve is inductively heated to 510-525°C as rapidly as possible. Upon reaching this temperature the shield, located between the specimen and the confining ring, is removed and an appropriate axial load, proportional to the predicted confining pressure, is applied to the transmitter bar with the MTS system. Application of the load results in the insertion of the specimen into the confining ring, and the specimen bottoms out on the lower loading anvil. The applied axial load is maintained throughout the cooling sequence. Pre-application of the axial pressure is permissible as long as the applied stress is less than the compressive yield strength of the specimen.

After the confining system reaches room temperature, the hydraulic actuator of the autofrettaged system is lowered into its final axial placement and rotated into its locking position. While maintaining axial load control with the MTS test system, the actuator of the autofrettaging apparatus is pressurized until it takes over the axial load from the MTS test system. At this point, the MTS system is switched to position control mode, and the output signal from the reaction bar is switched to controlling the axial stress with the actuator of the autofrettaged system. While maintaining the proper axial stress, the apparatus is transferred to a pre-aligned cradle on the SHPB system for high-strain-rate loading of the specimen.

5.4 Experimental Results

5.4.1 High-Strain-Rate Testing

A 0.6332-cm diameter by 1.27-cm long cylindrical specimen was prepared and inserted within the autofrettage device as outlined in the previous section. The specimen was 99.5% pure Al_2O_3 manufactured by Coors. The reported density was 3.90 g/cm^3 (the specimens were machined from a tile identical to those used in the ballistic experiments described in Section 2.0).

The transition platens (items 3 and 4 in Fig. 51) were machined from tungsten carbide (each of these loading anvils were single-piece fabrication although a line exists denoting the transition from a conical shape to a bar in Fig. 51). The confined high-strain-rate experiments were performed using the hybrid SHPB consisting of a strain-gaged, 0.154-m long incident bar and a similarly gaged

transmitter bar only 0.077 m in length. A short (0.05 m), high strength steel projectile was fired at 66 m/s to generate a 20-μs stress pulse within the bar system.

The apparatus was examined after the test. The tungsten carbide platens were shattered; no damage was visible to the confined Al_2O_3. It was decided to sacrifice the autofrettage assembly to further examine the ceramic. This is discussed below.

Previous work in our laboratory has shown [70] that stress rate signals derived from the transmitter bar are compromised by dispersion phenomena for specimen strain rates above about 2700 s^{-1}, an effect that was recently modeled and rationalized by Ravichandran and Subhash [71]. Accordingly, a series of experiments was performed involving the placement of strain gages at various locations along the transmitter bar to provide an empirical relationship that can be used to correct transmitter bar data and bring it into agreement with that obtained by specimen-mounted gages. Since the confinement process obviously precluded the latter, corrected transmitter bar data were utilized to derive the stress-time history of the sample.

Tests also were run with no confinement at strain rates of 10^{-4} s^{-1} and 5000 s^{-1}, the former using a servo-controlled hydraulic load machine and the latter the SHPB. In these cases, the samples were strain-gaged.

5.4.2 Damage Characterization

Following testing under confinment, the entire autofrettage device was sectioned using a diamond saw; half of the sample was polished and examined by SEM. From the other half, transmission electron microscope specimens were sectioned, cored, and ion-milled. Similar TEM specimens were obtained from untested alumina. Both groups of samples were examined in a 200 KeV transmission electron microscope.

5.4.3 Experimental Results

Shown in Fig. 53 is the time history of the stress pulse experienced by aluminum oxide confined within the autofrettage device and tested in the SHPB. The strain rate leading up to the peak stress (transmitter bar signal corrected for dispersion) was 5940 s^{-1}. Immediately upon reaching the maximum stress amplitude (beyond the hydrostat) of 4.85 GPa, the stress falls slightly and the

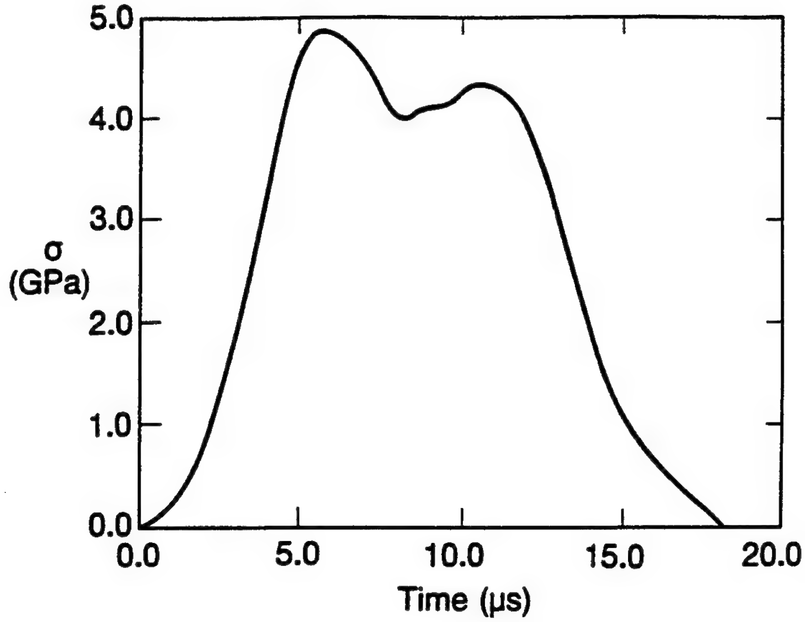

Figure 53. Stress-time history within confined Al_2O_3 sample

sample immediately begins to undergo apparent stable plastic flow with hardening. This lasts for a period of about 3.5 μs, so that the sample experienced high stresses (> 4 GPa) for approximately 8 μs. The incident pulse length of ~20 μs was not realized within the sample due to failure of the platens, although the specimen itself survived. When the autofrettage device was sectioned, the sample was revealed to be essentially intact, with the exception of a single large crack transverse to the applied axial load. This clearly was not a compressive failure, but rather an incidental fracture due to a dynamic post-test tensile release wave, or to relaxation induced by the sectioning itself. The static compressive strength, as reported by Coors, is only 0.38 GPa. By analogy with AD85, it is expected that the unconfined strength of the 99.5% Al_2O_3 is significantly enhanced to that of the static strength [65]. However, the strength level achieved in the autofrettage device (> 4 GPa) is considerably greater than that reported for unconfined specimens, which were reduced to dust and a few small fragments.

Under the SEM, no evidence of microfracture was visible on polished sections taken from the confined high-strain-rate specimen. Transmission electron microscopy (TEM), however, showed extensive evidence of plastic flow. Numerous grain boundary dislocation pileups (arrows, Figs. 54 thru 57) were observed, as well as deformation on multiple slip systems (Fig. 56). Some of the

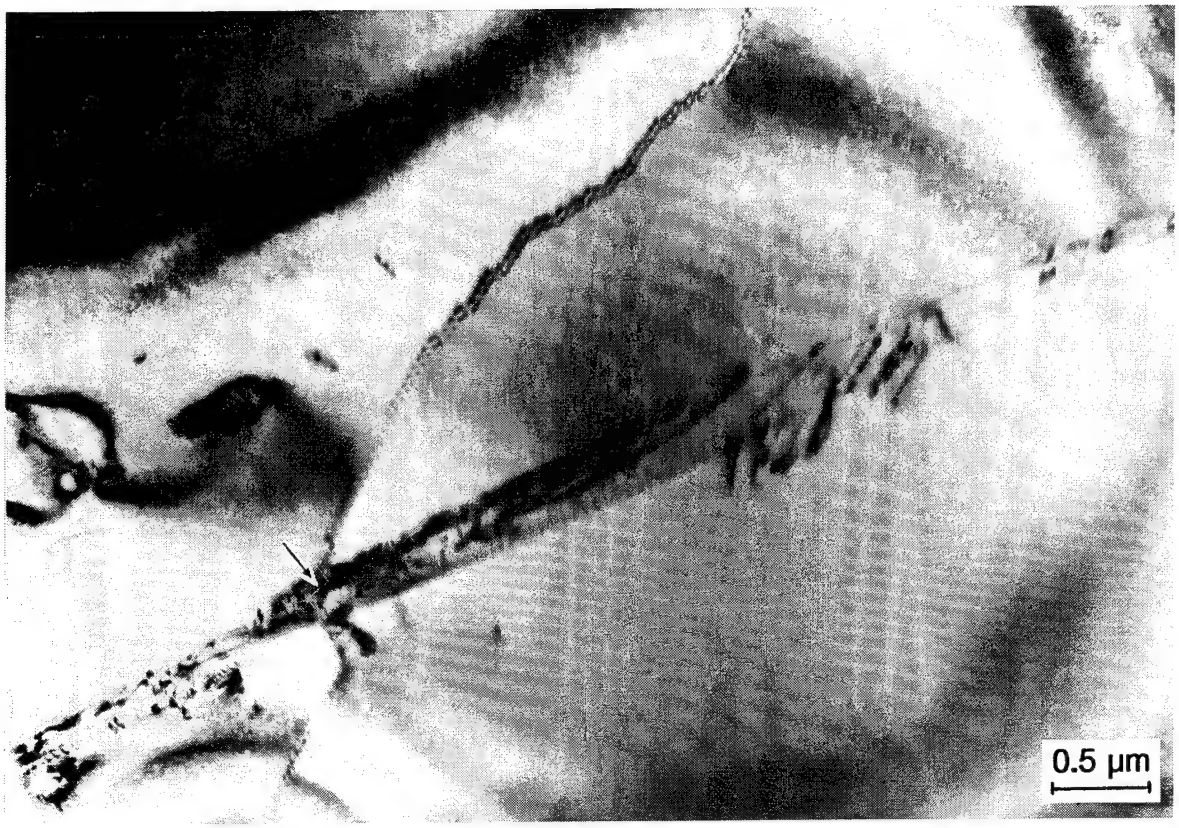

Figure 54. Slip band pileup at GB (arrow), nucleating slip band in adjacent (left) grain.

Figure 55. Slip band pileup at GB (arrow), nucleating transgranular microcrack in adjacent grains. Nearby are slip bands that have caused no microfracture.

Figure 56. Tilted view of image shown in Fig. 54, showing multiple slip system dislocation activity.

Figure 57. Dislocation slip band (arrow) nucleating transgranular microcrack in adjacent grain.

pileups induced dislocation activity in adjacent grains (Fig. 54), while others nucleated small transgranular microcracks (arrows, Figs. 55 thru 57). It should be noted that no microcracks were observed except in association with dislocation arrays, and no large (multi-grain) cracks were observed at all.

5.5 Discussion

It is well known [68, 72] that in the absence of confinement, alumina (like other brittle ceramics) fails in compression via the nucleation growth and coalescence of (roughly) axially-oriented microcracks. This is an apparently brittle fracture process, and usually occurs at stress levels below those characteristic of shock loading conditions, where compressive "failure" is represented by the Hugoniot elastic limit (HEL). The latter is the axial stress at which the material, loaded in compression under uniaxial strain constraint (perfect confinement), can no longer support purely elastic strain and begins to flow through either plastic flow or cataclastic (flow-like) fracture processes [73]. Contrasting with the (latter) high strain rate situation in which confinement is generated by inertial effects, is microhardness indentation under quasistatic conditions, with confinement provided by the indenter and elastic surround. In this case, the hardness (H) is a measure of compressive yielding, always at pressures much in excess of the unconfined compressive strength (σ_c).

Measured values of H and HEL thus include confinement terms superimposed on the uniaxial intrinsic static and dynamic yield strengths (Y_S and Y_D). Typically, the former is defined as [72]

$$Y_S \simeq H/3 \tag{24}$$

while [74]

$$Y_D = 2\frac{c_s^2}{c_l^2}\,\mathrm{HEL} \tag{25}$$

where c_s and c_l are the shear and longitudinal sound speeds, respectively. For 99.5% Al_2O_3, H = 14.5 GPa; HEL = 10.6 GPa; c_s = 6.24 km/s; and c_l = 10.56 km/s [74]. Based on these parameters and Eqns. (24) and (25), $Y_S \simeq 4.8$ GPa, and $Y_D = 4.3$ GPa. Grady has further shown [75] experimentally that over a limited dynamic strain rate range, Y_D is strain-rate independent.

The present experiments can be placed in perspective as shown in Figure 58. Here the compressive yield strength of Al_2O_3 is given for a strain rate range of 10^{-4} s^{-1} to 10^6 s^{-1}, with the current confined high-strain-rate experiment represented by the peak stress to which the sample was loaded beyond the hydrostate, i.e., 4.85 GPa. The results plotted in Fig. 58 lie within a tight range of stress levels, suggesting that the yield strength is virtually strain-rate insensitive.

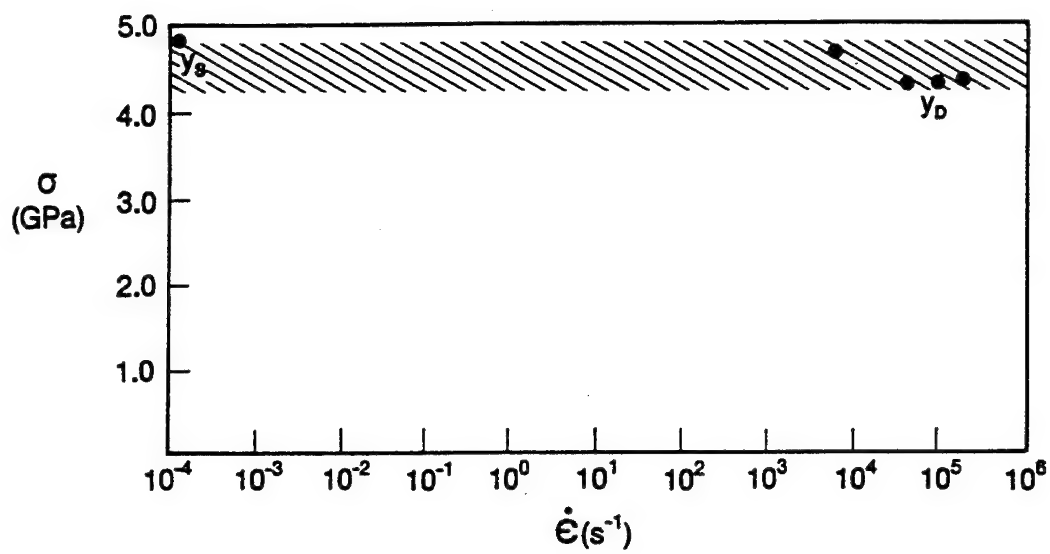

Figure 58. Compressive yield strength for 99.5% Al_2O_3 derived from indentation hardness (Y_S), plate impact (Y_D), and confined SHPB experiments.

Based on the TEM evidence and the shape of the stress-time history, it seems clear that the effect of the autofrettage confinement was to permit the sample to attain a stress level equal to the essentially strain-rate independent yield strength established by the microhardness and plate impact experiments. It is known that extensive plastic flow is associated with Al_2O_3 hardness impressions, [72], and Grady has recently hypothesized [76, 77] that it seems more reasonable to ascribe observed yielding within the shock front, i.e., the HEL, to plastic flow rather than to brittle microfracture. The present results appear virtually to assure that that is indeed the case. In particular, damage

associated with the autofrettage experiment consisted of extensive dislocation arrays and slip bands, plus occasional microcracks nucleated by slip band pileups.

This is consistent with earlier work by Cagnoux and Longy [78] involving SEM and X-ray analysis of plate impact fragments of 99.7% Al_2O_3, microstructurally similar to the present 99.5% Al_2O_3. Based on the absence of detectable microcracks, and the interpretation of X-ray line broadening, it was inferred that the shock ($\dot{\epsilon} \approx 10^5\ s^{-1}$) stress regime from 0.9 HEL to 2.0 HEL is dominated by plastic flow.

The present work also appears to have implications regarding the nature of "conventional" compressive strength in ceramics. It has been noted [72] that there exist striking correlations between compressive strength and indentation hardness, at least in terms of trends, i.e., $\sigma_c \propto H$. Moreover, Lankford has shown [72] that when optimal compressive test conditions are utilized in conjunction with strong, near-theoretically dense (minimum porosity) ceramic bodies, there is obtained an almost 1:1 correlation between Y_S and σ_c. This implies that under unconfined conditions, the highest compressive strength that can be attained is the intrinsic yield point, at which macroscopic plastic flow and associated microfracture will be inevitable, leading to rapid failure via microcrack coalescence. Under confinement, as demonstrated by Heard and Cline [68], this quasistatic limit can be exceeded, i.e., $\sigma_c > Y_S$, with monotonic hardening. The latter supports the interpretation of the present results (Fig. 53) that the confined sample under dynamic loading is experiencing stable post-yielding hardening.

6.0 ACKNOWLEDGEMENTS

The authors thank Ms. Suzanne Royal-Timmons for her assistance in the conduct of the ballistic experiments described in Section 2.0. We also thank Dr. Gordon Johnson and Mr. Tim Holmquist, of Alliant Techsystems, for performing the EPIC calculations discussed in Section 3.0. We gratefully acknowledge the contributions of Mr. Andrew Nagy and his expertise in taking the concept described in Section 5.0 and turning it into a working apparatus. And many thanks to Ms. Janet Banda for her time and dedication in assembling this report.

7.0 REFERENCES

1. C. E. Anderson, Jr., D. L. Littlefield, and J. D. Walker, "Long-rod penetration, target resistance, and hypervelocity Impact," *Int. J. Impact Engng,* **14** (1-4), 1-12 (1993).

2. D. L. Orphal, C. E. Anderson, Jr., R. R. Franzen, J. D. Walker, P. N. Schneidewind, and M. E. Majerus, "Impact and penetration by L/D $\leq$ 1 projectiles," *Int. J. Impact Engng.*, **14** (1-4), 551-560 (1993).

3. S. J. Bless and C. E. Anderson, Jr., "Penetration of hard layers by hypervelocity rod projectiles," *Int. J. Impact Engng.*, **14** (1-4), 85-93 (1993).

4. S. J. Bless, R. Subramanian, C. E. Anderson, Jr., and D. L. Littlefield, "Prediction of large scale high velocity penetration experiments on ceramic armor,"in **Proc. 13th Army Symp. on Solid Mechanics**, pp. 9-22 (Edited by S-C. Chu, D. D. Bartlett, Jr., T. W. Wright, and D. Iyer), Plymouth, MA, August 17-19 (1993).

5. C. E. Anderson, Jr., V. Hohler, J. D. Walker, and A. J. Stilp, "Penetration of long rods into steel and glass targets: experiments and computations," *14th Int. Symp. on Ballistics*, Vol. 1, pp. 145-154, Québec, Canada, September 26-29 (1993).

6. C. E. Anderson, Jr., S. J. Bless, D. L. Littlefield, and R. Subramanian, "Prediction of large scale impact experiments on steel targets," *14th Int. Symp. on Ballistics*, Vol. 2, pp. 459-468, Québec, Canada, September 26-29 (1993).

7. C. E. Anderson, Jr. and D. L. Littlefield, "Pretest predictions of long-rod interactions with armor technology targets," SwRI Report 07-5117, prepared for the U. S. Army Research Office, Southwest Research Institute, San Antonio, TX, April (1994).

8. C. E. Anderson, Jr., D. L. Littlefield, N. W. Blaylock, S. J. Bless, and R. Subramanian, "The penetration performance of short L/D projectiles," in **High Pressure Science and Technology 1993**, Vol. 2, pp. 1809-1812 (Edited by S. C. Schmidt, J. W. Shaner, G. A. Samara, and M. Ross), AIP Press, Woodbury, NY (1994).

9. D. L. Littlefield, C. E. Anderson, Jr., and S. R. Skaggs, "Analysis of penetration of steel and Al_2O_3 targets," in **High Pressure Science and Technology 1993**, Vol. 2, pp. 1793-1796 (Edited by S. C. Schmidt, J. W. Shaner, G. A. Samara, and M. Ross), AIP Press, Woodbury, NY (1994).

10. J. D. Walker and C. E. Anderson, Jr., "Multi-material velocities for mixed cells," in **High Pressure Science and Technology 1993**, Vol. 2, pp. 1773-1777 (Edited by S. C. Schmidt, J. W. Shaner, G. A. Samara, and M. Ross), AIP Press, Woodbury, NY (1994).

11. J. Lankford, C. E. Anderson, Jr., S. A. Royal, and J. P. Riegel, III, "Erosion mechanisms associated with tungsten alloy penetration of steel targets," *Dynamic Behavior of Materials, Materials Week '94*, TMS/AMS International, Rosemont, IL, Oct. 2-6 (1994).

12. C. E. Anderson, Jr., V. Hohler, J. D. Walker, and A. J. Stilp, "Time-resolved penetration of long rods into steel targets," *Int. J. Impact Engng.*, **16**(1), 1-18 (1995).

13. C. E. Anderson, Jr., S. A. Royal, and B. L. Morris, "Ballistic performance of confined 99.5% Al_2O_3 ceramic tiles," *Proc. 6th Annual TARDEC Combat Vehicle Survivability Symp.*, Vol. I, pp. 111-120, Monterey, CA, March 28-30 (1995).

14. C. E. Anderson, Jr., G. R. Johnson, and T. J. Holmquist, "Ballistic performance and computations of confined Al_2O_3 ceramic tiles," *15th Int. Symp. on Ballistics*, Vol. 2, pp. 65-72, Jerusalem, Israel, May 21-24 (1995).

15. C. E. Anderson, Jr., J. D. Walker, S. J. Bless, and T. R. Sharron, "On the velocity dependence of the L/D effect for long-rod penetrators," *Int. J. Impact Engng.,* **17**(1-4), (1995).

16. D. L. Orphal, C. E. Anderson, Jr., R. R. Franzen, and S. M. Babcock, "Variation of crater geometry with projectile L/D for $L/D \leq 1$," *Int. J. Impact Engng.,* **17**(1-4), (1995).

17. C. E. Anderson, Jr., J. D. Walker, S. J. Bless, and Y. Partom, "On the L/D effect for long-rod penetrators," *Int. J. Impact Engng.,* **18**(1) (1996).

18. J Lankford, C. E. Anderson, Jr., and S. A. Royal, "Penetration erosion phenomenology," *Int. J. Impact Engng.,* **18**, in publication (1996).

19. D. Yaziv, G. Rosenberg, and Y. Partom, "Differential ballistic efficiency of applique armor," *9th Int. Symp. on Ballistics*, Vol. 2, 315-319, Royal Military College of Science, Shrivenham, 29 April - 1 May (1986).

20. C. E. Anderson, Jr. and B. L. Morris, "The ballistic performance of confined Al_2O_3 ceramic tiles, *Int. J. Impact Engng.*, **12**(2), 167-187 (1992).

21. J. Lankford, C. E. Anderson, Jr., G. R. Johnson, and T. J. Holmquist, "Dynamic compressive failure of ceramics under confinement," *Proc. 1991 Combat Vehicle Survivability Conf.*, Vol. II, pp. 67-73, Gaithersburg, MD, April 15-17 (1991).

22. C. E. Anderson, Jr., P. E. O'Donoghue, J. Lankford, and J. D. Walker, "Numerical simulations of SHPB experiments for the dynamic compressive strength and failure of ceramics," *Int. J. Fract.,* **55**, 193-208 (1992).

23. Y. Partom and D. L. Littlefield, "Validation and calibration of a lateral confinement model for long-rod penetration at ordnance and high velocities," *Int. J. Impact Engng.*, **17**, in press (1995).

24. G. E. Hauver, P. H. Netherwood, R. F. Benck, W. A. Gooch, W. J. Perciballi, and M. S. Burkins, "Variation of target resistance during long-rod penetration into ceramics," *Proc. 13th Int. Symp. on Ballistics,* Vol. 3, pp. 257-264, Stockholm. Sweden, June 1-3 (1992).

25. A. M. Rajendran, "Modeling the impact behavior of AD85 ceramic under multiaxial loading," *Int. J. Impact Engng.*, **15**(6), 749-768 (1994).

26. D. A. Mandell and R. Henniger, "Evaluation of two ceramic models in the MESA code," LA-12267, Los Alamos National Laboratory, Los Alamos, NM, February (1992).

27. D. A. Mandell, "Prediction of alumina penetration," LA-12520, Los Alamos National Laboratory, Los Alamos, NM, February (1993).

28. T. J. Holmquist, G. R. Johnson, D. E. Grady, C. M. Lopatin, and E. S. Hertel, "High strain rate properties and constitutive modeling of glass," *15th Int. Symp. on Ballistics*, Jerusalem, Israel, May 21-24 (1995).

29. P. Woolsey, S. Mariano, and D. Kokidko, "Alternative test methodology for ballistic performance ranking of armor ceramics," *Fifth Annual TACOM Armor Coordinating Conf.*, Monterey, CA, March (1989).

30. P. Woolsey, "Ceramic materials screening by residual penetration ballistic testing," *Proc. 13th Int. Symp. on Ballistics,* Vol. 3, pp. 109-116, Stockholm. Sweden, June 1-3 (1992).

31. S. J. Bless and C. E. Anderson, Jr., "Penetration of hard layers by hypervelocity rod projectiles, *Int. J. Impact Engng.*, **14**, 85-93 (1993).

32. A. Tate, "A theory for the deceleration of long rods after impact," *J. Mech. Phys. Solids*, **15**, 387-399 (1967).

33. M. Wilkins, J. Gibbon, V. Hohler, A. J. Stilp, and M. Cozzi, "Ballistic performance of AlN, SiC, and Al_2O_3 ceramic tiles impacted by tungsten alloy long rod projectiles," *2nd Annual TACOM Combat Vehicle Survivability Symp.*, Vol. II, 75-95, Gaithersburg, MD, April (1991).

34. P. Woolsey, "Residual penetration ballistic testing of armor ceramics," *2nd Annual TACOM Combat Vehicle Survivability Symp.*, 75-95, Gaithersburg, MD, April (1991).

35. V. Hohler, A. J. Stilp, and K. Weber, "Hypervelocity penetration of tungsten sinter-alloy rods into alumina," *Int. J. Impact Engng.*, **17**, 409-418 (1995).

36. D. Yaziv and Y. Partom, "The ballistic efficiency of thick alumina targets against long rod penetrators," *Proc. 14th Int. Symp. on Ballistics*, Vol. 2, pp. 331-340, Québec, Canada, November (1993).

37. G. R. Johnson and T. J. Holmquist, "A computational constitutive model for brittle materials subjected to large strains, high strain rates, and high pressures," **Shock Waves and High-**

Strain Rate Phenomena in Materials, pp. 1075-1081 (Edited by M. A. Myers, L. E. Murr, and K. P. Staudhammer) Marcel Dekker, NY (1992).

38. G. R. Johnson and T. J. Holmquist, "An improved computational constitutive model for brittle materials," **High Pressure Science and Technology—1993**, Vol. 2, pp. 981-984, (Edited by S. C. Schmidt, J. W. Shaner, G. A. Samara, and M. Ross), AIP Press, Woodbury, NY (1994).

39. T. J. Holmquist, G. R. Johnson, D. E. Grady, C. M. Lopatin and E. S. Hertel, "High strain rate properties and constitutive modeling of glass," *Proc. 15th Int. Symp. on Ballistics*, Vol. 1, pp. 237-244, Jerusalem, Israel (1995).

40. D. E. Grady, "Dynamic properties of ceramic materials," Sandia National Laboratories Technical Report, SAND94-3266, February (1995).

41. G. R. Johnson, E. H. Petersen and R. A. Stryk, "Incorporation of an SPH option into the EPIC code for a wide range of high velocity impact computations," *Int. J. Impact Engng.*, **14**, 385-394 (1993).

42. G. R. Johnson and W. H. Cook, "A constitutive model and data for metals subjected to large strains, high strain rates and high temperatures," pp. 541-547, *Proc. 7th Int. Symp. on Ballistics*, The Hague, The Netherlands, (1983).

43. G. R. Johnson and W. H. Cook, "Fracture characteristics of three metals subjected to various strains, strain rates, temperatures and pressures," *Engng. Fract. Mech,* **21**(1), 31-48 (1985).

44. G. R. Johnson and T. J. Holmquist," Test data and computational strength and fracture model constants for 23 materials subjected to large strains, high strain rates, and high temperatures," LA-11463-MS, Los Alamos National Laboratory, NM, January (1989).

45. G. R. Johnson, "Artificial viscosity effects for SPH impact calculations," *Int. J. Impact Engng.*, accepted for publication (1995).

46. G. R. Johnson, "Linking of lagrangian particle methods to standard finite element methods for high velocity impact computations," *Nucl. Engng. Design*, **150** (1994).

47. J. Dehn, "Modeling dwell in ceramic armor," *Proc. 15th Int. Symp. on Ballistics*, Vol. 1, pp. 435-442, Jerusalem, Israel (1995).

48. G. E. Hauver, P. H. Netherwood, R. F. Benck, and L. J. Kecskes, "Ballistic performance of ceramic targets," *Proc. Army Symp. on Solid Mech.*, Plymouth, MA, August 17-19 (1993).

49. G. E. Hauver, P. H. Netherwood, R. F. Benck, and L. J. Kecskes, "Enhanced ballistic performance of ceramics," *Proc. 19th Army Science Conf.*, Orlando, FL, June 20-24 (1994).

50. J. Dehn, Army Research Laboratory, private communication (1995).

51. C. E. Anderson, Jr., J. D. Walker, and G. E. Hauver, "Target resistance for long-rod penetration into semi-infinite targets," *Nucl. Engng. and Design*, **138**, 93-104 (1992).

52. A. Tate, "Long rod penetration models—part II. Extensions to the hydrodynamic theory of penetration," *Int. J. Engng. Sci.*, **28**, 599-612 (1986).

53. C. E. Anderson, Jr. and J. D. Walker, "An examination of long-rod penetration," *Int. J. Impact Engng.*, **11**(4), 381-501 (1991).

54. J. M. McGlaun, S. L Thompson, and M. G. Elrick, "CTH: a three-dimensional shock wave physics code," *Int. J. Impact Engng.*, **10**(1-4), 351-360 (1990).

55. W. W. Predebon, C. E. Anderson, Jr., and J. D. Walker, "Inclusion of evolutionary damage measures in Eulerian wavecodes," *Comp. Mech.*, **7**(4), 221-236 (1991).

56. S. Silling, "Stability and accuracy of differencing methods for viscoplastic models in wavecodes," *J. Comp. Phys.*, **104**, 30-40 (1993).

57. J.D. Walker and C.E. Anderson, Jr., "A time-dependent model for long-rod penetration," *Int. J. Impact Engng.*, **16**(1), 19-48 (1995).

58. J. Reaugh, Lawrence Livermore National Laboratory, private communication.

59. L. A. Glenn, B. Moran, and A. S. Kusubov, "Modeling jet penetration in glass," *Proc. of the Conf. on the Application of 3-D Hydrocodes to Armor/Anti-Armor Problems*, U.S. Army Ballistic Research Laboratory, Aberdeen Proving Ground, MD, May 8-9 (1990).

60. B. Moran, L. A. Glenn, and A. Kusubov, "Experiments and calculations of jet penetration in glass," *Proc. Combat Vehicle Survivability Symp.*, Vol. II, pp. 177-186, Gaithersburg, MD, April 15-17 (1991).

61. U.S. Lindholm, L.M. Yeakley, and A. Nagy, *Int. J. Rock Mech. Min. Sci.,* **11**, 181-191 (1974).

62. R. Arrowood and J. Lankford, *Jour. Mat. Sci.*, **22**, 3737 (1987).

63. S. Serdengecti and G.D. Boozer, "The effects of strain rate and temperature on the behavior of rocks subjected to triaxial compression," *Proc. 4th Symp. Rock Mech.,* Pennsylvania State University, 83 (1961).

64. R. J. Christensen, S.R. Swanson, and W.S. Brown, *Experimental Mechanics,* **12**, 508-513 (1972).

65. J. Lankford, C.E. Anderson, Jr., G.R. Johnson, and T.J. Holmquist, "Dynamic compressive failure of ceramics under confinement," *Proc. 1991 Combat Vehicle Survivability Conf.*, Vol. II, pp. 67-73, Gaithersburg, MD, April 15-17 (1991).

66. U.S. Lindholm, in *Techniques of Metals Research,* **5**(1), 199-271 (Edited by R.F. Bunshah), John Wiley & Sons, NY (1971).

67. C.E. Anderson, Jr., P.E. O'Donoghue, J. Lankford, and J.D. Walker, "Numerical simulations of SHPB experiments for the dynamic compressive strength and faiure of ceramics," *Int. J. Fract.*, **55**, 193-208 (1992).

68. H.C. Heard and C.F. Cline, "Mechanical behavior of polycrystalline BeO, Al_2O_3, and AlN at high pressure," *J. Matl. Sci.*, **15**, 1889-1897 (1980).

69. W. Chen and G. Ravichandran, "Static and dynamic compressive behavior of aluminum nitride under moderate confinement," *J. Am. Ceram. Soc.* (submitted).

70. J. M. Staehler, W.W. Predebon, B.J. Pletka, and J. Lankford, "Testing of high-strength ceramics with the split-hopkinson pressure bar," *J. Am. Ceram. Soc.*, **76**, 536-538 (1993).

71. G. Ravichandran and G. Subhash, "Critical appraisal of limiting strain rates for compression testing of ceramics in a split-hopkinson pressure bar," *J. Am. Ceram. Soc.*, **77**, 263-267 (1994).

72. J. Lankford, "The compressive strength of strong ceramics: microplasticity versus microfracture," *J. Hard Materials*, **2**, 55-77 (1991).

73. D. E. Grady, "Dynamic material properties of armor ceramics," Sandia Report No. SAND91-0147, Sandia National Laboratories, Albuquerque, NM (March 1991).

74. D. E. Grady and J. L. Wise, "Dynamic properties of ceramic materials," Sandia Report No. SAND93-0610, Sandia National Laboratories, Albuquerque, NM (September 1993).

75. D. E. Grady, "Constitutive modeling: theory and applications," *CIMNE*, Barcelona, 1995 (to be published).

76. D. E. Grady, "Dynamic properties of ceramic materials," Sandia Report No. SAND94-3266, Sandia National Laboratories, Albuquerque, NM (February 1995).

77. D. E. Grady, "Shock-wave properties of brittle materials," *1995 APS Topical Conference on Shock Compression of Condensed Matter*, Seattle, WA, August 13-18 (1995).

78. J. Cagnoux and F. Longy, "Spallation and shock-wave behaviour of some ceramics," *Journal de Physique*, **49**, C3.3-C3.10, September 1988.